MICRO- AND MILLIFLUIDIC PLATFORMS FOR IMAGING AGENT SYNTHESIS

BY

JOSEPH JAMES WHITTENBERG

DISSERTATION

Submitted in partial fulfillment of the requirements
for the degree of Doctor of Philosophy in Chemical Engineering
in the Graduate College of the
University of Illinois at Urbana-Champaign, 2017

Urbana, Illinois

Doctoral Committee:

Professor Paul J.A. Kenis, Chair
Associate Professor David E. Reichert, Washington University in St. Louis
Professor Hong Yang
Associate Professor Ling-Jian Meng
Assistant Professor Damien S. Guironnet

Abstract

Molecular imaging, the non-invasive visualization of cellular and sub-cellular events, holds great promise to improve the basic understanding of biochemical processes and clinical diagnosis of diseases. One widely used molecular imaging technique is positron emission tomography (PET) that is especially useful for clinical oncology applications. PET has seen remarkable growth recently due to improvements in the regulation of PET radiotracers and the development of multimodal imaging set-ups that combine the sensitivity of PET with X-ray computed tomography (CT) or magnetic resonance imaging (MRI) that provide anatomical details. To date the most widely used PET radiotracer is [^{18}F]fluorodeoxyglucose ([^{18}F]FDG). Despite the widespread use of [^{18}F]FDG, ^{18}F has a short half-life and [^{18}F]FDG cannot detect certain cancers. There is a desire to develop radiometal-based radiotracers that have a wide selection of radioisotope half-lives from 10's of minutes to days. Additionally, these tracers have the potential for flexible synthesis of tumor-specific tracers by easily changing the biomolecule (BM) utilized. However, radiometal-based PET radiotracers still face key challenges including (1) site-specific attachment of bifunctional chelators (BFCs), responsible for chelating the radiometal, to tumor-targeting biomolecules and (2) improving synthesis equipment to reduce reagent use and radiation shielding costs.

My dissertation primarily focuses on addressing the challenges associated with radiometal-based PET radiotracer synthesis. "Click chemistry", or more specifically Cu(I)-catalyzed azide-alkyne cycloaddition (CuAAC), was utilized to address the concern regarding site-specific attachment of BFCs to BMs. CuAAC, like other "click reactions", yields products with few side reactions under mild reaction conditions which is key when working with biomolecules. However, PET radiotracers are typically made in small batches because radioisotopes are

utilized. Microfluidic platforms enable handling of small volumes, reducing reagent use and simultaneously minimizing radiation shielding costs due to their inherently small size. Here I describe how microfluidics was merged with the "click chemistry" concept to produce BM-BFC conjugates with the potential to be used as PET radiotracers. In Chapter 2 I describe the initial development and fabrication of a "click chip" with immobilized Cu(I) catalyst to facilitate CuAAC reactions that also minimizes purification requirements because the cytotoxic Cu(I) catalyst is immobilized to the microfluidic platform. Chapter 3 discusses how the "click chip" was improved to reduce solvent loss and enable longer reactions to conjugate BMs and BFCs.

Nanoparticles (NPs) are another class of imaging agents that have some advantages over small molecule-based imaging agents (e.g., facile incorporation of multiple imaging modalities). However, many NPs are synthesized using low-yield synthetic strategies not amenable for scale up (e.g., microfluidics). Microfluidic mixers have been well characterized over the past decades, but few efforts have focused on millifluidic mixers and millifluidic platforms in general. Millifluidic devices offer some of the same advantages as microfluidics, such as rapid heat and mass transfer, but also enable higher throughput and are typically easier to fabricate. In Chapter 4 I discuss the design and fabrication of a millifluidic mixer that was validated by synthesizing gold nanoparticles (AuNPs).

Ultimately, I was able to develop microfluidic and millifluidic platforms that have the potential to improve synthesis of imaging agents.

To my family

Acknowledgements

This dissertation would not have been possible without the help and support of my family, friends, and colleagues. First and foremost I would like to thank my advisor Dr. Paul J. A. Kenis for his advice and guidance during my graduate career at the University of Illinois. His tutelage improved my skills as an independent researcher, and he continuously supported my goals and various side projects.

Furthermore, I would like to thank the rest of the Kenis group for helping me with my graduate studies, especially Dr. Amit Desai for mentoring me my first few years in graduate school. Amit was always available to discuss challenges and research directions and I greatly appreciate his assistance. I would like to give a big shout out to Jeremy Schieferstein, Dr. Vivek Kumar, and Dr. Sichao Ma, who joined the Kenis group at the same time I did. They not only assisted me with my research, but also were great friends outside the lab. Many other graduate students and senior members of the Kenis group helped make UIUC a special place, especially, Sumit Verma, Byoungsu Kim, Dr. Ash Pawate, Dr. Liz Horstman, Dr. Matt Byrne, Dr. Sachit Goyal, Dr. Sudipto Guha, Dr. Ritika Mohan, Dr. Josh Tice, Dr. Matt Naughton, Dr. Daria Khvostichenko, Whitney Sinclair, Ajit Vikram, and Uzoma Nwabara. I also had the privilege of working with Jan Koziol, Chotitath Sanpitakseree, Heeral Patel, and Keegan Lane. These undergraduate students assisted me with my different research projects and helped make this dissertation possible.

I worked with many faculty and staff here at UIUC that aided me with my research and Unit Operations lab manager responsibilities. Whenever equipment needed to be modified or fixed Kyle Webb, Kyle Kroha, Hodge Harland, Tom Wilson, and multiple other staff members at UIUC were able to provide much needed assistance. The several user-based facilities here at

Illinois provided the equipment and expertise to complete many of my experiments, and I would like to thank Dr. Lucas Li, Dr. Alex Ulanov, Dr. Rick Haasch, and Dr. Glennys Mensing in particular for their assistance and troubleshooting.

Much of this work would not have been possible without help from Dr. David Reichert and members of his lab, including Dr. David Ranganathan, Dr. Hairong Li, Dr. Haiying Zhou, and Dr. Brian Wright. Dr. Reichert was a fantastic mentor and provided great insight into some of the challenges I encountered in the field of nuclear medicine. Dr. Reichert's lab also synthesized and provided some of the key reagents for the "click chip" projects, especially the Cu(I) ligand.

A wide variety of sources were critical for funding my work. These sources include the National Institutes of Health (R01 CA16134802 and R25 CA154015A), Dow Chemical Company (research agreement #226772AC), the Diffenbaugh Fellowship, the Ullyot Graduate Fellowship, the Hanratty Travel Award, and the Graduate College Travel Award.

I would also like to thank my family. My mom, dad, and brother in particular continuously encouraged me to pursue my dreams, and I would not be where I am today without them.

Table of Contents

Chapter 1

Introduction

Molecular imaging can broadly be defined as the noninvasive visualization of biochemical processes on the sub-cellular and cellular levels, but the specifics of what molecular imaging entails can differ depending on the field.[1] Molecular imaging continues to improve the understanding of basic biochemistry and cell biology as well as clinical diagnostics and disease treatment. A primary motivation of molecular imaging is to overcome the limitations of standard *in vitro* assays by moving to an *in vivo* setting.[1] Some advantages of molecular imaging compared to traditional *in vitro* assays include (1) noninvasively studying cells in their natural environment in real-time[2], (2) capable of performing repeated studies with the same animal, enabling collection of longitudinal data[3, 4], and (3) rapidly determining pharmacokinetics and pharmacodynamics of new drug candidates reducing time and cost for drug development[4]. Key molecular imaging agent modalities include X-ray computed tomography (CT), positron emission tomography (PET), single-photon emission computed tomography (SPECT), magnetic resonance imaging (MRI), and ultrasound (US). The choice of imaging modality/modalities depends on a number of criteria such as required spatial resolution, requisite sensitivity (minimum imaging agent concentration necessary for detection), and whether a whole body or only a small region needs to be imaged.[1, 5]

Two of the aforementioned imaging techniques, PET and SPECT, require administering radioisotope-based imaging probes into the subject/sample and detecting the decaying isotopes. These radioisotope indicators, typically with the radioisotope incorporated into a biologically active compound, are also known as radiotracers.[6] Radiotracers have proven particularly adept

for clinical oncology applications because (1) only minute concentrations (as low as picomolar) of imaging probes are required compared to concentrations of contrast agents for other molecular imaging modalities such as CT (~millimolar) or MRI (~micromolar)[7] and (2) radiotracers are able to specifically target tumors. Radiotracer specificity for particular tumors is accomplished by incorporating biomolecules (BMs) such as peptides[8, 9], antibodies[10, 11], sugars[12], and nucleosides[13, 14] into the radiotracers to either target overexpressed surface receptors on cells, or abnormal tumor metabolism[13] (*e.g.*, excess glucose uptake). PET is particularly useful for oncology because PET has a higher sensitivity, higher resolution, and superior quantitative capability compared to SPECT.[15]

1.1 History of PET radiotracers

In the next few paragraphs I will present a brief history of PET and nuclear medicine in general to provide context on the future of PET radiotracers. A timeline (**Figure 1.1**) displays key dates for radiopharmaceuticals (including radiotracers) as well as "click chemistry" and microfluidics, which will be discussed in more detail in later sections in Chapter 1. There are several other sources available that discuss the history of nuclear medicine in more detail.[16-21]

The birth of oncology imaging occurred in 1895 with the discovery of X-rays, and the first diagnostic radiotracer procedure performed on a human was in 1925, to measure circulation time.[16, 22] A facile method to produce certain radionuclides was developed in 1931 by Ernest Lawrence when he invented the cyclotron. This was a key event for radiotracer production and nuclear medicine in general[23], and the first cyclotron devoted to biomedical radionuclide production was built roughly a decade later at Washington University in St. Louis.[17] Another important step in the development of PET and radiotracers occurred in 1951, when the first use of positrons for a medical application was reported.[21, 24]

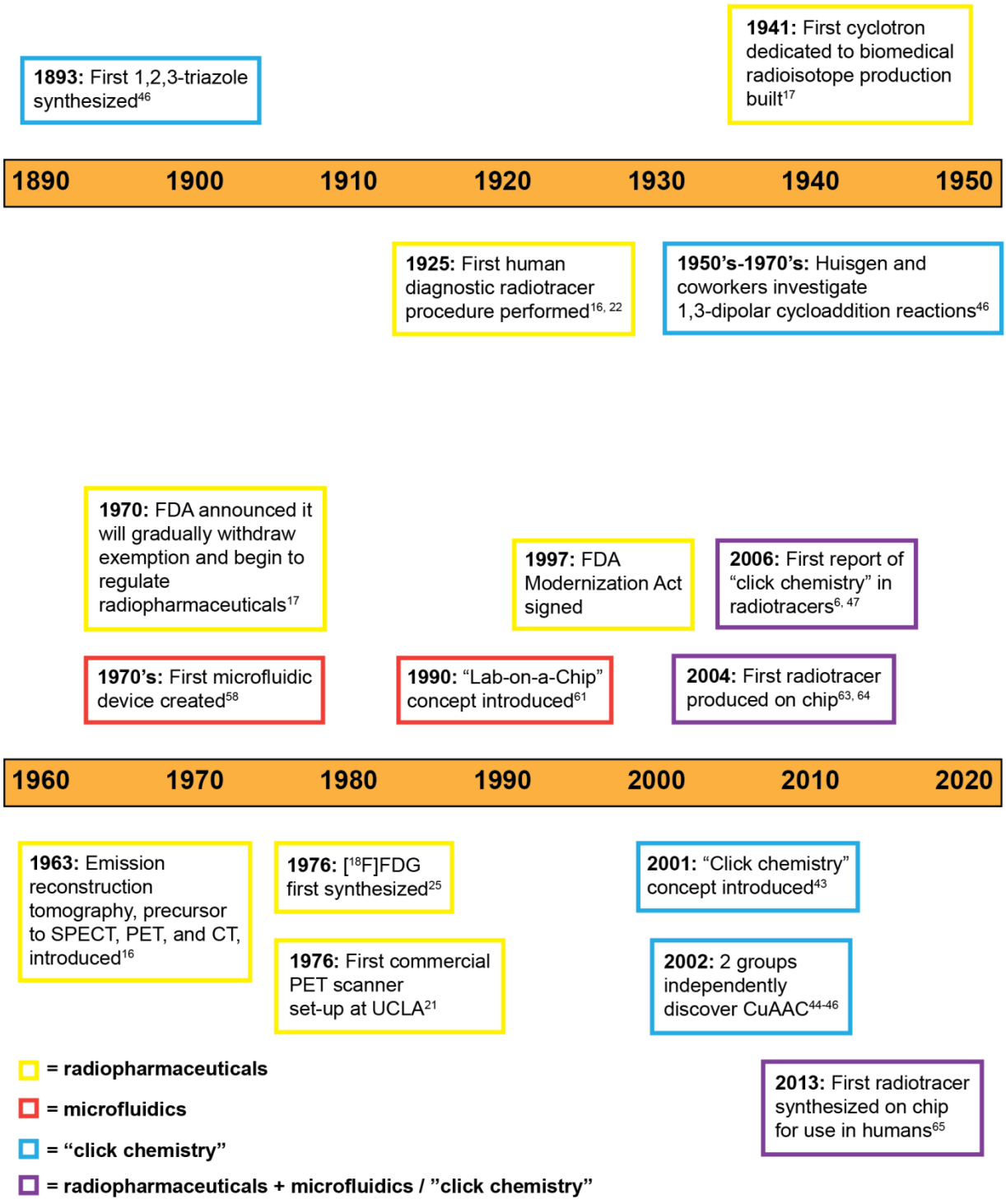

Figure 1.1. A timeline that summarizes significant events for (1) radiopharmaceuticals (including radiotracers), (2) microfluidics, and (3) "click chemistry" with an emphasis on the Cu(I)-catalyzed azide-alkyne cycloaddition (CuAAC) reaction. The events in purple are for events that created radiotracers with either microfluidics or "click chemistry".

However, producing and using radioisotopes is only part of the equation. Methods to acquire images of radiotracers significantly advanced in 1963, when David Kuhl and Roy Edwards introduced emission reconstruction tomography, the precursor to PET, SPECT, and CT[16], and the first commercial PET scanner was set-up in 1976 at the University of California, Los Angeles[21]. [^{18}F]fluorodeoxyglucose (^{18}[F]FDG) was produced for the first time in 1976 as well[25], and not only did ^{18}[F]FDG help pave the way for PET use and research as discussed later in the regulation of PET radiotracers, ^{18}[F]FDG is currently the most commonly used PET probe[26].

Initial clinical PET applications in the 1970s and 1980s focused on the field of neurology (e.g., evaluating brain function)[16], and PET wasn't extensively used clinically for oncology until the 1990s.[27] Over the last few decades, improvements in PET have come from multimodality imaging by combining PET and CT or PET and MRI. While PET is a highly sensitive molecular imaging technique, PET images lack the desired anatomical detail. Hence, PET/CT and PET/MRI equipment enables collection of complementary anatomic and biologic information that enhances localization of lesions.[28, 29]

Another key aspect of the history and future of PET radiotracers is regulation, and for the purposes of this dissertation I will solely discuss regulation in the United States. PET radiotracers and production methods are unique compared to other pharmaceuticals for a number of reasons. First and foremost, because PET radiotracers have incorporated radioisotope(s) these probes require regulation as a drug and a radioactive compound. This distinction requires cooperation from multiple regulatory bodies and organizations in the United States including the Food and Drug Administration (FDA), the Nuclear Regulatory Commission (NRC), and the United States Pharmacopeia (USP). Additionally, many PET radiotracers have short half-lives requiring unique guidance on production and quality control.[18] Similarly, because radiotracers

have high specificity, they are often administered in millimolar or micromolar concentrations to patients. At these concentrations PET radiotracers are well below toxic doses, and therefore require a different perspective regarding toxicology studies.[30] Finally, from a cost standpoint two important factors to consider are (1) the importance of reimbursing PET procedures and (2) the expense of regulations on radiopharmacies producing PET radiotracers that are typically smaller than large pharmaceutical manufacturers.[19, 31]

From a regulation standpoint, two of the major regulatory agencies involved are the FDA and NRC, formerly the Atomic Energy Commission (AEC) prior to splitting into the NRC and the current Department of Energy (DOE). Additionally, the USP is a nonprofit organization that fills an important role by developing and improving drug standards that the FDA enforces. The FDA and AEC/NRC regulate different aspects of radiopharmaceutical production and use, but since 1975 the clinical use of all radiopharmaceuticals, including PET radiotracers, has been regulated by the FDA.[18] As PET continued to develop, early PET centers (~1985-1998) were funded mostly by the National Institutes of Health (NIH) and DOE, but funding eventually became difficult to attain.[19] In addition to funding challenges, expensive FDA regulations and lack of reimbursements for PET radiopharmaceuticals prevented further growth of PET.[31] The FDA Modernization Act (FDAMA) was signed in 1997 to revamp the FDA and the agencies' regulations, including PET radiotracer regulations. Separately, ^{18}[F]FDG was approved by the FDA and the first reimbursements for ^{18}[F]FDG occurred in 1998. These two events were vital for reducing cost of PET scans and led to a sudden growth in PET.[19, 30] The FDAMA ultimately led to improved regulation of PET radiopharmaceuticals, including the creation of title 21 of the Code of Federal Regulations part 212 (21 CFR 212) that became effective in 2011[32], and outlines current good manufacturing practice (CGMP) for PET radiopharmaceuticals. The regulatory

landscape for PET radiotracers played a critical role in the growth of PET radiotracers from the late 1990s to present, and also indicates the need of PET radiotracer production to meet the relatively new CGMP regulations.

1.2 Conventional PET radiotracer synthesis

Nuclear medicine has progressed significantly in the last ~90 years since the first diagnostic radiotracer procedure performed on a human in 1925. However, there are still many challenges with the production and use of radiopharmaceuticals, including PET radiotracers. As mentioned previously in this chapter, the most widely used PET radiotracer is ^{18}[F]FDG.[26] However, ^{18}[F]FDG lacks the specificity to detect some types of tumors including liver, prostate, pancreas, and brain tumors.[33] Additionally, traditional PET radioisotopes used for tumor imaging such as ^{18}F, ^{13}N, and ^{11}C have short half-lives (< 2 h), limiting their use to smaller BMs that rapidly accumulate in tumors.[34] Additionally, non-metal radioisotopes typically require complex synthesis steps with harsh reaction conditions.[35]

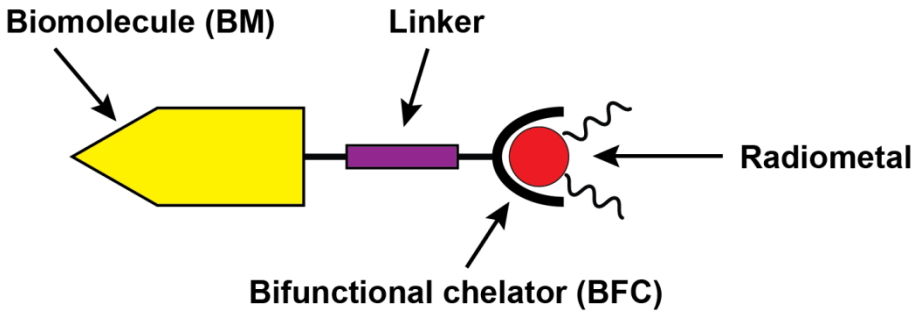

Figure 1.2. A schematic showing the four main components, (1) biomolecule, (2) radiometal, (3) bifunctional chelator, and (4) linker, of a typical radiometal-based radiotracer.

However, radiometals such as ^{64}Cu, ^{89}Zr, and ^{68}Ga have a wide range of half-lives on the order of 10's of minutes to days and can easily be incorporated into tracers via a simple chelation event. Typical radiometal-based PET tracers consist of four main components: (1) a biomolecule to specifically target tumors, (2) a radiometal that emits positrons to enable imaging, (3) a

bifunctional chelator to bind the radiometal, and (4) a linker to covalently attach the BFC to the BM (**Figure 1.2**). Radiometal-based tracers are advantageous compared to radiotracers with non-metal radioisotopes because radiometal-based radiotracers offer flexibility, modularity, and simplicity.[35] Radiometal radiotracers are modular in the sense that BMs and BFCs can be conjugated in different combinations to provide the required tumor specificity by tuning the BM, while also enabling attachment of different radiometals by altering the BFC. The ability to change the BFC and associated radiometal provides flexibility to match the half-life of the probe to the half-life of the BM (i.e., adjust based on time for radiotracer to reach the target).[34] Also, for smaller BMs (e.g., peptides) BFCs can affect the pharmacokinetics and biodistribution. The actual chelation of the radiometal to the BFC can be achieved under mild conditions and is typically simple to purify, unlike ^{18}F-based probes which require harsh reaction conditions and complicated purifications.[35] One key challenge with radiometal-based radiotracers is the site specific attachment of BFCs to BMs which is typically accomplished via amide, thiourea, and thioether bonds.[36] However, biomolecules tend to have multiple free primary amines and thiols making site-specific BFC attachment a challenge.[37]

While radiometal-based tracers offer unique advantages over ^{18}F and other non-metal radiotracers, the production of radiometal PET tracers still faces challenges. Conventional radiotracer synthesis methods typically involve many tedious steps and impose constraints on conjugation reactions (i.e., conjugating BMs and BFCs), such as the requirement of protection/de-protection steps to prevent unwanted side reactions during conjugation reactions.[38] Additionally, commonly used radiopharmaceuticals are conventionally produced in automated synthesis modules (ASMs) that utilize high-dilution conditions and consume large quantities of

reagents.[8, 39, 40] ASMs are expensive, require highly trained staff to operate, and due to their bulky size (~80 cm x 60 cm x 40 cm) require large amounts of space and radiation shielding.[41, 42]

1.3 Addressing challenges in PET radiotracer synthesis

Cu(I) "click chemistry"

As mentioned previously, attachment of BFCs to BMs is typically accomplished via amide, thiourea, and thioether bonds.[36] Yet these conjugation methods are challenging because the many functional groups present on BMs require protection/de-protection steps to prevent side reactions. In 2001 Kolb, Finn, and Sharpless outlined the concepts of "click chemistry" to describe reactions that chemoselectively form non-natural heteroatom links in high yields under simple reaction conditions.[43] The most widely utilized "click" reaction, Cu(I)-catalyzed azide-alkyne cycloaddition (CuAAC), was discovered in 2002 by two independent groups, Meldal in Denmark[44], and Fokin and Sharpless[45] in the United States.[46] However, the origins of CuAAC date back to 1893 when the first 1,2,3-triazole was synthesized, and the reaction between azides and alkynes was examined further in the 1950s-1970s by Huisgen and coworkers when they studied the larger family of 1,3-dipolar cycloaddition reactions.[46] However, thermal reactions of alkynes and azides have exceedingly low reaction rates due to high activation barriers, and also result in a mixture of regioisomers (**Scheme 1.1A**). The discovery of CuAAC in 2002 demonstrated that Cu(I) catalyst rapidly increased the reaction rate of alkynes and azides even at room temperature (**Scheme 1.1B**).[46] Following the breakthrough discovery of CuAAC, the first example of "click" chemistry in radiopharmaceutical science was reported by Marik and Sutcliffe in 2006.[6, 47]

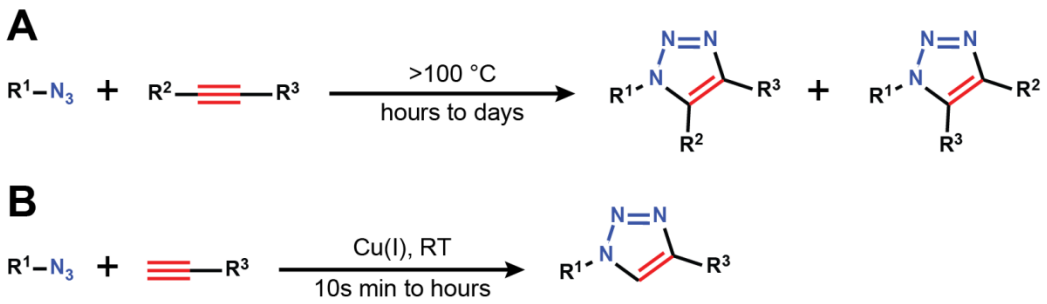

Scheme 1.1. General precursors, products, and reaction conditions for thermal cycloaddition of azides and alkynes (A) and CuAAC (B). Thermal cycloaddition reactions result in a mixture of regioisomers while CuAAC yields only 1,4-disubstituted regioisomers. Adapted from Hein et al.[46] with permission of The Royal Society of Chemistry.

Ultimately, "click chemistry", CuAAC in particular, provided a bioorthogonal method to conjugate BMs and BFCs, and reduced the number of protection/de-protection steps required for radiotracer synthesis.[48] Also, "click" reactions are commonly performed in mild, non-toxic, aqueous conditions that are amenable for the conjugation of biomolecules.[49] More specifically for radiotracers, the resulting triazole ring from CuAAC conjugation reactions is highly resilient to degradation *in vivo* and displays tumor uptake comparable to analogous tracers using traditional prosthetic groups.[48, 50] Despite the advantages of CuAAC for bioconjugation, challenges exist regarding the Cu(I) catalyst. Two key limitations of the CuAAC "click" reaction are (1) the thermodynamic instability of the Cu(I) oxidation state and (2) the need to remove the cytotoxic Cu(I) catalyst.[51]

A convenient method to potentially avoid the aforementioned complications is to immobilize the Cu(I) catalyst on a solid support. Ligands have been used to not only stabilize the Cu(I) state, but also to immobilize the Cu(I) catalyst to a solid support such as resins[52, 53], polysaccharides[54], silica particles[55], and a number of other supports[56] for CuAAC "click" reactions. Immobilized Cu(I) catalyst systems have the potential to minimize purification times[56] and obviate the need for sodium ascorbate, commonly added to maintain Cu in the +1 oxidation state, which can

produce reactive oxygen species in the presence of Cu to react with or cleave BMs (e.g., peptides, antibodies).[57]

Microfluidics

CuAAC addresses challenges related to the conjugation of BFCs and BMs, but progress in synthesis equipment is required to improve handling of precursors and products during synthesis of PET radiotracers. A few of the key challenges of current PET radiotracer synthesis are (1) the bulky size of current equipment that requires a commensurately large amount of radiation shielding, (2) excessive consumption of reagents, and (3) radiolysis, which is the cleavage of chemical bonds by ionizing radiation from free or incorporated radioisotopes that can reduce radiotracer yield. Regardless of what new technology is developed for PET radiotracer synthesis, the equipment must be able to synthesize radiotracers in a quick, robust, and repeatable manner with the potential for automation to improve worker safety.[40]

Microfluidic devices, comprised of enclosed channels and features ~10s to 100s of micrometers tall/wide have the potential to address these challenges. The first microfluidic device, a miniaturized gas chromatography system, was created in the 1970s[58], and many of the first microfluidic systems were microanalytical methods including capillary electrophoresis.[59, 60] The micro-total analysis system (μ-TAS) or "lab-on-a-chip" concept was introduced in 1990 by Manz et al.[61]; the concepts of which are now used in applications such as analysis and synthesis in fields ranging from chemistry to biology[62]. Eventually microfluidic platforms were used for radiotracer production with the first example occurring in 2004[63] to produce esters labeled with ^{11}C or ^{18}F.[64] The use of microfluidics for PET radiotracer synthesis continued to grow after the initial example in 2004 and eventually a set-up was built in 2013 to produce radiotracers for use in humans for the first time[65].

Microfluidics has the potential to address many challenges in radiotracer production including reducing reagent consumption and footprint to minimize costs.[66] The small dimensions also enable precise control of reaction conditions including temperature and mass transfer, and microfluidic systems have the potential for automation. Furthermore, microfluidic designs can be adjusted to minimize radiolytic effects to improve radiotracer yields.[67] Numerous radiotracers have been produced using microfluidic set-ups as outlined by Pascali et al.[40] However, most microfluidic systems focus on the production of ^{18}F-based radiotracers with little previous work on radiometal-based tracers. As discussed previously, radiometal-based PET tracers have advantages over traditional non-metal radiotracers including facile radioisotope incorporation and purification. These radiometal tracers could also benefit from the advantages provided by microfluidic systems.

Combining CuAAC and microfluidics

As depicted in **Figure 1.1** the development of radiopharmaceuticals, "click chemistry", and microfluidics have all just recently started to mature to a point enabling combination of these fields. The initial "lab-on-a-chip" concept wasn't introduced until 1990[61] and chip fabrication techniques were still in their infancy. CuAAC wasn't discovered until 2002[44, 45] and the term "click chemistry"[43] was coined just one year before. Also, despite the long history of nuclear medicine, PET radiotracers for clinical oncology didn't take off until the 1990s and even then PET didn't truly grow until after [^{18}F]FDG procedures began being reimbursed in 1998 and the FDA began to significantly change regulation for PET radiopharmaceuticals in 1997. Therefore, the combination of these three technologies didn't begin until the mid-2000s. The work described in this dissertation describes how all three technologies ("click chemistry",

microfluidics, and radiotracers) were combined by utilizing microfluidics and CuAAC to synthesize BM-BFC conjugates useful as PET radiotracers.

1.4 Improving platforms for nanoparticle synthesis

In addition to my work developing microfluidic platforms to improve PET radiotracer synthesis I also worked on developing a millifluidic mixer for use in nanoparticle (NP) synthesis in collaboration with Dr. Vivek Kumar, formerly a member of the Kenis lab. Nanoparticles possess unique optical, magnetic, and chemical properties that provide distinctive advantages over small molecule based imaging agents including (1) facile incorporation of multiple imaging modalities, (2) potential for higher signal-to-background ratios, and (3) localization at tumor sites via the enhanced permeability and retention effect due to "leaky" tumor blood vessels.[68, 69] A multitude of nanoparticles have been created for medical imaging purposes including gold NPs[70, 71], quantum dots[72], and Fe_3O_4 magnetic NPs[73]. However, most functionalized NPs are synthesized using low-yield synthetic strategies not amenable for scale up. Lohse et al. addressed this issue by creating a simple millifluidic reactor to produce AuNPs in a high throughput fashion, but specifically mentioned the current design was a "version 1.0" model and one potential improvement would be to incorporate new mixer designs.[74]

Rapid mixing is critical for NP synthesis because poor mixing contributes to high polydispersity and poor batch-to-batch reproducibility.[75] However, fast mixing at the micro- and millifluidic level can be challenging because flows are typically laminar due to the small channel dimensions and low velocities. Both active and static mixers have been developed to quickly mix solutions on the microfluidic scale. Active mixers require an external energy source while passive mixers only require pressure head and structures in the mixer to improve mixing.[76] Passive mixers are typically more desirable because they are simpler to fabricate and easier to

interface with other fluidic components.[77] Many different types of passive mixers have been developed including triangle baffles[77], double-heart chambers[78], and 3-D serpentine channels[79]. One of the most prevalent microfluidic mixers is the staggered herringbone mixer (SHM), originally developed by Stroock et al.[80], because of the simple design and proven capability as an efficient mixer.[81, 82]

Microfluidic passive mixers have been studied extensively over the past decades.[83, 84], but few efforts have focused on millifluidic mixers.[85] Millifluidic platforms, like microfluidic platforms, enable rapid mass and heat transfer[86], but millifluidics enables higher throughput and simpler fabrication.[74, 86, 87] Many micromixers utilize traditional soft lithography techniques that typically use polydimethylsiloxane (PDMS) replica molding.[77, 80, 81] Not only is PDMS replica molding more difficult for devices with larger features due to fabrication challenges (*e.g.*, photoresist delamination, loss of PDMS features), but PDMS soft lithography techniques are not amenable for mass production. Poly(methyl methacrylate) (PMMA) has many desirable traits including optical transparency, low cost, and multiple methods for patterning features and bonding.[88] Additionally, previous work fabricated a groove based micromixer in PMMA (300 μm wide, 100 μm deep including grooves) supporting the feasibility of using PMMA as an alternative material to create mixers.[89] PMMA and other thermoplastics also have the potential for mass fabrication through injection molding or hot embossing unlike PDMS.

Developing an improved millifluidic mixer for NP synthesis has the potential to improve throughput and reduce cost of fabrication while maintaining low polydispersity and high batch-to-batch reproducibility. Additionally, micro- and millifluidic platforms are commercially available and reduce required expertise to fabricate and utilize these systems and improve the transition from academic research to industrial production.[90] Continued development and

improvement of micro- and millifluidic platforms will enable both academic and industrial settings to take advantage of small-scale systems while reducing the expertise necessary for fabrication.

1.5 Objectives

The overall objective of my research is to improve micro- and millifluidic platforms for utilization in the medical imaging community, especially PET radiotracers. In my dissertation I will discuss two different small-scale platforms. The first platform is a "click chip" with an immobilized ligand with chelated Cu(I) to catalyze CuAAC reactions, and the second is a millifluidic static mixer that enables rapid mixing of reagents for applications including AuNP synthesis. Both platforms are useful to the medical imaging community but many fields utilize CuAAC or require rapid mixing including pharmaceutical synthesis, biological assays, and nanoparticle production.

This dissertation is separated into five chapters, including this chapter. In Chapter 2 I discuss the design, fabrication, and initial testing of the "click chip". Chapter 3 provides details on how the "click chip" design was improved to accommodate BM and BFC conjugation reactions. Furthermore, Chapter 3 discusses the validation of the improved "click chip" by testing three different BM and BFC conjugation reactions on the "click chip". Chapter 4 switches gears from BM and BFC conjugation reactions to talk about the design, fabrication, and validation of a millifluidic SHM for AuNP synthesis. Finally, Chapter 5 summarizes the main conclusions of the dissertation and outlines future directions.

1.6 References

(1) James, M. L., and Gambhir, S. S. (2012) A Molecular Imaging Primer: Modalities, Imaging Agents, and Applications. *Physiol. Rev. 92*, 897-965.
(2) Pysz, M. A., Gambhir, S. S., and Willmann, J. K. (2010) Molecular imaging: current status and emerging strategies. *Clin. Radiol. 65*, 500-516.

(3) Chen, Z. Y., Wang, Y. X., Lin, Y., Zhang, J. S., Yang, F., Zhou, Q. L., and Liao, Y. Y. (2014) Advance of Molecular Imaging Technology and Targeted Imaging Agent in Imaging and Therapy. *Biomed. Res. Int. 2014*.
(4) Willmann, J. K., van Bruggen, N., Dinkelborg, L. M., and Gambhir, S. S. (2008) Molecular imaging in drug development. *Nat. Rev. Drug. Discov. 7*, 591-607.
(5) Ametamey, S. M., Honer, M., and Schubiger, P. A. (2008) Molecular imaging with PET. *Chem. Rev. 108*, 1501-1516.
(6) Mamat, C., Ramenda, T., and Wuest, F. R. (2009) Recent Applications of Click Chemistry for the Synthesis of Radiotracers for Molecular Imaging. *Mini-Rev. Org. Chem. 6*, 21-34.
(7) Hussain, T., and Nguyen, Q. T. (2014) Molecular imaging for cancer diagnosis and surgery. *Adv. Drug Deliv. Rev. 66*, 90-100.
(8) Liu, Y., Tian, M., and Zhang, H. (2013) Microfluidics for Synthesis of Peptide-Based PET Tracers. *Biomed. Res. Int. 2013*.
(9) Dijkgraaf, I., Rijnders, A. Y., Soede, A., Dechesne, A. C., van Esse, G. W., Brouwer, A. J., Corstens, F. H. M., Boerman, O. C., Rijkers, D. T. S., and Liskamp, R. M. J. (2007) Synthesis of DOTA-conjugated multivalent cyclic-RGD peptide dendrimers via 1,3-dipolar cycloaddition and their biological evaluation: implications for tumor targeting and tumor imaging purposes. *Org. Biomol. Chem. 5*, 935-944.
(10) Vosjan, M. J. W. D., Perk, L. R., Visser, G. W. M., Budde, M., Jurek, P., Kiefer, G. E., and van Dongen, G. A. M. S. (2010) Conjugation and radiolabeling of monoclonal antibodies with zirconium-89 for PET imaging using the bifunctional chelate p-isothiocyanatobenzyl-desferrioxamine. *Nat. Protoc. 5*, 739-743.
(11) Zhang, Y., Hong, H., and Cai, W. (2011) PET tracers based on Zirconium-89. *Curr. Radiopharm. 4*, 131-9.
(12) Abouzied, M. M., Crawford, E. S., and Nabi, H. A. (2005) 18F-FDG imaging: pitfalls and artifacts. *J. Nucl. Med. Technol. 33*, 145-55; quiz 162-3.
(13) Graham, M. M. (2012) Clinical Molecular Imaging with Radiotracers: Current Status. *Med. Prin. Pract. 21*, 197-208.
(14) Meyer, J.-P., Probst, K. C., and Westwell, A. D. (2014) Radiochemical synthesis of 2′-[18F]-labelled and 3′-[18F]-labelled nucleosides for positron emission tomography imaging. *J. Labelled Compd. Rad. 57*, 333-337.
(15) Hicks, R. J., and Hofman, M. S. (2012) Is there still a role for SPECT-CT in oncology in the PET-CT era? *Nat. Rev. Clin. Oncol. 9*, 712-720.
(16) Sharma, B., Martin, A., Stanway, S., Johnston, S. R. D., and Constantinidou, A. (2012) Imaging in oncology-over a century of advances. *Nat. Rev. Clin. Oncol. 9*, 728-737.
(17) Knapp, F. F., and Dash, A. (2016) *Radiopharmaceuticals for Therapy*, Springer India.
(18) Saha, G. B. (2016) *Basics of PET Imaging: Physics, Chemistry, and Regulations*, Third ed., Springer International Publishing.
(19) Muehllehner, G., and Karp, J. S. (2006) Positron emission tomography. *Phys. Med. Biol. 51*, R117-R137.
(20) Agdeppa, E. D., and Spilker, M. E. (2009) A Review of Imaging Agent Development. *AAPS J. 11*, 286-299.
(21) Nutt, R. (2002) The History of Positron Emission Tomography. *Mol. Imaging Biol. 4*, 11-26.

(22) Patton, D. D. (2003) The birth of nuclear medicine instrumentation: Blumgart and Yens, 1925. *J. Nucl. Med. 44*, 1362-1365.
(23) Wagner, H. N. (2007) *A Personal History of Nuclear Medicine*, Springer London.
(24) Sweet, W. H. (1951) The Uses of Nuclear Disintegration in the Diagnosis and Treatment of Brain Tumor. *N. Engl. J. Med. 245*, 875-878.
(25) Yu, S. (2006) Review of F-FDG Synthesis and Quality Control. *Biomed. Imag. Interv. J. 2*, e57.
(26) Uz Zaman, M., Fatima, N., Sajjad, Z., Zaman, U., Tahseen, R., and Zaman, A. (2014) 18FDG Synthesis and Supply: a Journey from Existing Centralized to Future Decentralized Models. *Asian Pac. J. Cancer Prev. 15*, 10057-10059.
(27) Buck, A. K., Herrmann, K., Stargardt, T., Dechow, T., Krause, B. J., and Schreyögg, J. (2010) Economic Evaluation of PET and PET/CT in Oncology: Evidence and Methodologic Approaches. *J. Nucl. Med. Technol. 38*, 6-17.
(28) Rischpler, C., Nekolla, S. G., Dregely, I., and Schwaiger, M. (2013) Hybrid PET/MR Imaging of the Heart: Potential, Initial Experiences, and Future Prospects. *J. Nucl. Med. 54*, 402-15.
(29) Pichler, B. J., Kolb, A., Nägele, T., and Schlemmer, H.-P. (2010) PET/MRI: Paving the Way for the Next Generation of Clinical Multimodality Imaging Applications. *J. Nucl. Med. 51*, 333-336.
(30) Wagner, H. N. (2007) PET is alive and well. *J. Nucl. Med. 48*, 495-495.
(31) Hung, J. C. (2013) Bringing New PET Drugs to Clinical Practice - A Regulatory Perspective. *Theranostics 3*, 885-893.
(32) Schwarz, S. W., Dick, D., VanBrocklin, H. F., and Hoffman, J. M. (2014) Regulatory Requirements for PET Drug Production. *J. Nucl. Med. 55*, 1132-1137.
(33) Schelbert, H. R. (2011) Nuclear Medicine at a Crossroads. *J. Nucl. Med. 52*, 10s-15s.
(34) Wadas, T. J., Wong, E. H., Weisman, G. R., and Anderson, C. J. (2010) Coordinating Radiometals of Copper, Gallium, Indium, Yttrium, and Zirconium for PET and SPECT Imaging of Disease. *Chem. Rev. 110*, 2858-2902.
(35) Zeglis, B. M., Houghton, J. L., Evans, M. J., Viola-Villegas, N., and Lewis, J. S. (2014) Underscoring the Influence of Inorganic Chemistry on Nuclear Imaging with Radiometals. *Inorg. Chem. 53*, 1880-1899.
(36) Zeglis, B. M., and Lewis, J. S. (2011) A practical guide to the construction of radiometallated bioconjugates for positron emission tomography. *Dalton Trans. 40*, 6168-6195.
(37) Knör, S., Modlinger, A., Poethko, T., Schottelius, M., Wester, H.-J., and Kessler, H. (2007) Synthesis of Novel 1,4,7,10-Tetraazacyclodecane-1,4,7,10-Tetraacetic Acid (DOTA) Derivatives for Chemoselective Attachment to Unprotected Polyfunctionalized Compounds. *Chem. – Eur. J. 13*, 6082-6090.
(38) Hein, C., Liu, X.-M., and Wang, D. (2008) Click Chemistry, A Powerful Tool for Pharmaceutical Sciences. *Pharm. Res. 25*, 2216-2230.
(39) Elizarov, A. M. (2009) Microreactors for radiopharmaceutical synthesis. *Lab Chip 9*, 1326-1333.
(40) Pascali, G., Watts, P., and Salvadori, P. A. (2013) Microfluidics in radiopharmaceutical chemistry. *Nucl. Med. Biol. 40*, 776-787.

(41) Gillies, J. M., Prenant, C., Chimon, G. N., Smethurst, G. J., Perrie, W., Hambletta, I., Dekker, B., and Zweit, J. (2006) Microfluidic reactor for the radiosynthesis of PET radiotracers. *Appl. Radiat. Isot. 64*, 325-332.
(42) Lin, W. Y., Wang, Y. J., Wang, S. T., and Tseng, H. R. (2009) Integrated microfluidic reactors. *Nano Today 4*, 470-481.
(43) Kolb, H. C., Finn, M. G., and Sharpless, K. B. (2001) Click Chemistry: Diverse Chemical Function from a Few Good Reactions. *Angew. Chem., Int. Ed. 40*, 2004-2021.
(44) Tornoe, C. W., Christensen, C., and Meldal, M. (2002) Peptidotriazoles on solid phase: 1,2,3 -triazoles by regiospecific copper(I)-catalyzed 1,3-dipolar cycloadditions of terminal alkynes to azides. *J. Org. Chem. 67*, 3057-3064.
(45) Rostovtsev, V. V., Green, L. G., Fokin, V. V., and Sharpless, K. B. (2002) A stepwise huisgen cycloaddition process: copper(I)-catalyzed regioselective "ligation" of azides and terminal alkynes. *Angew. Chem., Int. Ed. Engl. 41*, 2596-9.
(46) Hein, J. E., and Fokin, V. V. (2010) Copper-catalyzed azide-alkyne cycloaddition (CuAAC) and beyond: new reactivity of copper(I) acetylides. *Chem. Soc. Rev. 39*, 1302-1315.
(47) Marik, J., and Sutcliffe, J. L. (2006) Click for PET: rapid preparation of [F-18]fluoropeptides using Cu-I catalyzed 1,3-dipolar cycloaddition. *Tetrahedron Lett. 47*, 6681-6684.
(48) Wangler, C., Schirrmacher, R., Bartenstein, P., and Wangler, B. (2010) Click-chemistry reactions in radiopharmaceutical chemistry: fast & easy introduction of radiolabels into biomolecules for in vivo imaging. *Curr. Med. Chem. 17*, 1092-116.
(49) Nwe, K., and Brechbiel, M. W. (2009) Growing applications of "click chemistry" for bioconjugation in contemporary biomedical research. *Cancer Biother. Radiopharm. 24*, 289-302.
(50) Zeng, D. X., Zeglis, B. M., Lewis, J. S., and Anderson, C. J. (2013) The Growing Impact of Bioorthogonal Click Chemistry on the Development of Radiopharmaceuticals. *J. Nucl. Med. 54*, 829-832.
(51) Thundimadathil, J. (2013) Click chemistry in peptide science: a mini-review Synthesis of clickable peptides and applications. *Chim. Oggi 31*, 34-37.
(52) Chan, T. R., and Fokin, V. V. (2007) Polymer-supported copper(I) catalysts for the experimentally simplified azide-alkyne cycloaddition. *QSAR Comb. Sci. 26*, 1274-1279.
(53) Baxendale, I. R., Ley, S. V., Mansfield, A. C., and Smith, C. D. (2009) Multistep Synthesis Using Modular Flow Reactors: Bestmann-Ohira Reagent for the Formation of Alkynes and Triazoles. *Angew. Chem., Int. Ed. 48*, 4017-4021.
(54) Reddy, K. R., Rajgopal, K., and Kantam, M. L. (2007) Copper-alginates: a blopolymer supported Cu(II) catalyst for 1,3-dipolar cycloaddition of alkynes with azides and oxidative coupling of 2-naphthols and phenols in water. *Catal. Lett. 114*, 36-40.
(55) Li, P., Wang, L., and Zhang, Y. (2008) SiO2-NHC-Cu(I): an efficient and reusable catalyst for 3+2 cycloaddition of organic azides and terminal alkynes under solvent-free reaction conditions at room temperature. *Tetrahedron 64*, 10825-10830.
(56) Dervaux, B., and Du Prez, F. E. (2012) Heterogeneous azide-alkyne click chemistry: towards metal-free end products. *Chem. Sci. 3*, 959-966.
(57) Hong, V., Presolski, S. I., Ma, C., and Finn, M. G. (2009) Analysis and optimization of copper-catalyzed azide-alkyne cycloaddition for bioconjugation. *Angew. Chem., Int. Ed. Engl. 48*, 9879-9883.

(58) Terry, S. C., Jerman, J. H., and Angell, J. B. (1979) Gas-Chromatographic Air Analyzer Fabricated on a Silicon-Wafer. *IEEE T. Electron Dev. 26*, 1880-1886.
(59) McDonald, J. C., Duffy, D. C., Anderson, J. R., Chiu, D. T., Wu, H. K., Schueller, O. J. A., and Whitesides, G. M. (2000) Fabrication of microfluidic systems in poly(dimethylsiloxane). *Electrophoresis 21*, 27-40.
(60) Whitesides, G. M. (2006) The origins and the future of microfluidics. *Nature 442*, 368-373.
(61) Manz, A., Graber, N., and Widmer, H. M. (1990) Miniaturized Total Chemical-Analysis Systems - a Novel Concept for Chemical Sensing. *Sensor Actuat B-Chem 1*, 244-248.
(62) Harrison, D. J. (2013) A personal stroll through the historical development of Canadian microfluidics. *Lab Chip 13*, 2500-2503.
(63) Lu, S. Y., Watts, P., Chin, F. T., Hong, J., Musachio, J. L., Briard, E., and Pike, V. W. (2004) Syntheses of C-11- and F-18-labeled carboxylic esters within a hydrodynamically-driven micro-reactor. *Lab Chip 4*, 523-525.
(64) Liu, K., Wang, M. W., Lin, W. Y., Phung, D. L., Girgis, M. D., Wu, A. M., Tomlinson, J. S., and Shen, C. K. F. (2011) Molecular Imaging Probe Development Using Microfluidics. *Curr. Org. Synth. 8*, 473-487.
(65) Lebedev, A., Miraghaie, R., Kotta, K., Ball, C. E., Zhang, J. Z., Buchsbaum, M. S., Kolb, H. C., and Elizarov, A. (2013) Batch-reactor microfluidic device: first human use of a microfluidically produced PET radiotracer. *Lab Chip 13*, 136-145.
(66) Keng, P. Y., Sergeev, M., and van Dam, R. M. (2016) Advantages of Radiochemistry in Microliter Volumes, in *Perspectives on Nuclear Medicine for Molecular Diagnosis and Integrated Therapy* (Kuge, Y., Shiga, T., and Tamaki, N., Eds.) pp 93-111, Springer Japan, Tokyo.
(67) Rensch, C., Waengler, B., Yaroshenko, A., Samper, V., Baller, M., Heumesser, N., Ulin, J., Riese, S., and Reischl, G. (2012) Microfluidic reactor geometries for radiolysis reduction in radiopharmaceuticals. *Appl. Radiat. Isot. 70*, 1691-1697.
(68) Choi, H. S., and Frangioni, J. V. (2010) Nanoparticles for Biomedical Imaging: Fundamentals of Clinical Translation. *Mol. Imaging 9*, 291-310.
(69) Chapman, S., Dobrovolskaia, M., Farahani, K., Goodwin, A., Joshi, A., Lee, H., Meade, T., Pomper, M., Ptak, K., Rao, J., Singh, R., Sridhar, S., Stern, S., Wang, A., Weaver, J. B., Woloschak, G., and Yang, L. (2013) Nanoparticles for cancer imaging: The good, the bad, and the promise. *Nano Today 8*, 454-460.
(70) Zhao, Y., Sultan, D., Detering, L., Cho, S., Sun, G., Pierce, R., Wooley, K. L., and Liu, Y. (2014) Copper-64-Alloyed Gold Nanoparticles for Cancer Imaging: Improved Radiolabel Stability and Diagnostic Accuracy. *Angew. Chem., Int. Ed. 53*, 156-159.
(71) Coughlin, A. J., Ananta, J. S., Deng, N., Larina, I. V., Decuzzi, P., and West, J. L. (2014) Gadolinium-Conjugated Gold Nanoshells for Multimodal Diagnostic Imaging and Photothermal Cancer Therapy. *Small 10*, 556-565.
(72) Gao, X. H., Cui, Y. Y., Levenson, R. M., Chung, L. W. K., and Nie, S. M. (2004) In vivo cancer targeting and imaging with semiconductor quantum dots. *Nat. Biotechnol. 22*, 969-976.
(73) Yoo, H., Moon, S. K., Hwang, T., Kim, Y. S., Kim, J. H., Choi, S. W., and Kim, J. H. (2013) Multifunctional Magnetic Nanoparticles Modified with Polyethylenimine and Folic Acid for Biomedical Theranostics. *Langmuir 29*, 5962-5967.

(74) Lohse, S. E., Eller, J. R., Sivapalan, S. T., Plews, M. R., and Murphy, C. J. (2013) A Simple Millifluidic Benchtop Reactor System for the High-Throughput Synthesis and Functionalization of Gold Nanoparticles with Different Sizes and Shapes. *ACS Nano 7*, 4135-4150.
(75) Rahman, M., and Rebrov, E. (2014) Microreactors for Gold Nanoparticles Synthesis: From Faraday to Flow. *Processes 2*, 466.
(76) Lee, C. Y., Chang, C. L., Wang, Y. N., and Fu, L. M. (2011) Microfluidic Mixing: A Review. *Int. J. Mol. Sci. 12*, 3263-3287.
(77) Wang, L., Ma, S., Wang, X., Bi, H., and Han, X. (2014) Mixing enhancement of a passive microfluidic mixer containing triangle baffles. *Asia Pac. J. Chem. Eng. 9*, 877-885.
(78) Fu, L.-M., Fang, W.-C., Hou, H.-H., Wang, Y.-N., and Hong, T.-F. (2014) Rapid vortex microfluidic mixer utilizing double-heart chamber. *Chem. Eng. J. 249*, 246-251.
(79) Kang, T. G., Singh, M. K., Anderson, P. D., and Meijer, H. E. H. (2009) A chaotic serpentine mixer efficient in the creeping flow regime: from design concept to optimization. *Microfluid. Nanofluid. 7*, 783-794.
(80) Stroock, A. D., Dertinger, S. K. W., Ajdari, A., Mezic, I., Stone, H. A., and Whitesides, G. M. (2002) Chaotic Mixer for Microchannels. *Science 295*, 647-651.
(81) Williams, M. S., Longmuir, K. J., and Yager, P. (2008) A practical guide to the staggered herringbone mixer. *Lab Chip 8*, 1121-1129.
(82) Land, K. J., Mbanjwa, M., and Korvink, J. G. (2014) Microfluidic channel structures speed up mixing of multiple emulsions by a factor of ten. *Biomicrofluidics 8*, 054101.
(83) Lee, C.-Y., Chang, C.-L., Wang, Y.-N., and Fu, L.-M. (2011) Microfluidic Mixing: A Review. *Int. J. Mol. Sci. 12*, 3263-3287.
(84) Lee, C.-Y., Wang, W.-T., Liu, C.-C., and Fu, L.-M. (2016) Passive mixers in microfluidic systems: A review. *Chem. Eng. J. 288*, 146-160.
(85) Woldemariam, M., Filimonov, R., Purtonen, T., Sorvari, J., Koiranen, T., and Eskelinen, H. (2016) Mixing performance evaluation of additive manufactured milli-scale reactors. *Chem. Eng. Sci. 152*, 26-34.
(86) Shahbazali, E., Hessel, Volker, Noël, Timothy, Wang, Qi. (2016) Metallic nanoparticles made in flow and their catalytic applications in micro-flow reactors for organic synthesis. *Physical Sciences Reviews 1*.
(87) Tran, T.-T., Nguyen, M.-H., Tan, Y. Z., Chew, J. W., Khan, S. A., and Hadinoto, K. (2017) Millifluidic synthesis of amorphous drug-polysaccharide nanoparticle complex with tunable size intended for supersaturating drug delivery applications. *Eur. J. Pharm. Biopharm. 112*, 196-203.
(88) Rahbar, M., Chhina, S., Sameoto, D., and Parameswaran, M. (2010) Microwave-induced, thermally assisted solvent bonding for low-cost PMMA microfluidic devices. *J. Micromech. Microeng. 20*.
(89) Tofteberg, T., Skolimowski, M., Andreassen, E., and Geschke, O. (2010) A novel passive micromixer: lamination in a planar channel system. *Microfluid. Nanofluid. 8*, 209-215.
(90) Elvira, K. S., i Solvas, X. C., Wootton, R. C. R., and deMello, A. J. (2013) The past, present and potential for microfluidic reactor technology in chemical synthesis. *Nat. Chem. 5*, 905-915.

Chapter 2

Development of a "click chip" with immobilized Cu(I) catalyst*

2.1 Introduction

The use of biomolecules such as peptides or antibodies as the targeting moiety for imaging agents has benefited from the development of "click chemistry" based reactions. A major benefit of "click" reactions is the reduction in the number of protection/de-protection steps due to the bioorthogonal nature of these reactions, the functional groups of neither the reactants nor the product interact with the functionalized biomolecule[1], and only complementary functional groups form bonds. An additional advantage is that most "click" reactions are compatible with mild, non-toxic, aqueous conditions, a necessary feature for reactions involving many biomolecules. A review on the application of "click chemistry" and bioorthogonal reactions for labeling biological molecules was published by Best in 2009.[2]

One of the most common "click" reactions is the Cu(I) catalyzed Huisgen 1,3-dipolar cycloaddition of an azide and alkyne.[3] The Cu(I) state is thermodynamically unstable under normal oxidative conditions, but can be protected by complexation with the tetradentate ligand tris-(benzyltriazolylmethyl)amine (TBTA) from oxidation and disproportion.[4, 5] For *in vivo* use, imaging agents prepared through "click chemistry" utilizing Cu(I) catalysis requires purification in order to remove the toxic copper salts and any associated ligands from the desired product. An additional consideration is the reducing agents required to maintain the Cu(I) oxidation state may also react with the other reagents (e.g., peptides or antibodies) leading to adverse effects.[6]

*This chapter was adapted from Li, H. R., Whittenberg, J. J., Zhou, H. Y., Ranganathan, D., Desai, A. V., Koziol, J., Zeng, D. X., Kenis, P. J. A., and Reichert, D. E. (2015) Development of a microfluidic "click chip" incorporating an immobilized Cu(I) catalyst. *RSC Adv. 5*, 6142-6150 with permission from The Royal Society of Chemistry. This work was performed in collaboration with Dr. David Reichert's group at Washington University in St. Louis. Dr. Hairong Li (Reichert group) contributed to the writing and figures, specifically Figures 2.6 – 2.10 and Schemes 2.1 – 2.3.

Microfluidic devices, comprising enclosed micro-channels (normally 10-500 μm wide or tall), mixing units, heaters, pumping systems, are able to control and process chemical or biological reactions in a continuous flow manner or batch mode.[7-11] Microreactor synthesis offers: (1) manipulation of small volumes, which mitigates issues associated with diluting reagents, (2) efficient mixing to prevent mass transfer limitations, and (3) exceptional control of reaction conditions, such as reagent concentrations and temperature, that enable reliable and reproducible reaction yields. These characteristics of microreactors for chemical processing and synthesis are attractive for *in situ* "click chemistry", and have been successfully demonstrated in integrated microfluidics platforms for parallel or large-scale screening by Tseng et al.[10, 12]

The previously mentioned undesirable requirements of the Cu(I) catalyzed "click" reaction (need for purification and side reactions of reductants) could be eliminated by the immobilization of an oxidatively robust Cu(I) complex. The catalytic copper center can be reduced to the active Cu(I) in the absence of sensitive biological molecules, and the catalyst can then be easily separated from the products. Many previous Cu(I) immobilization schemes utilize nitrogen or carboxylate containing molecules to chelate the copper catalyst onto resins[13, 14], polysaccharides[15], silica particles[16], and other solid supports[17]. One of the more promising immobilized catalyst systems, now commercially available through Sigma-Aldrich, was developed by Chan et al., and consisted of TBTA bound to TentaGel resin.[14] Cu(I) bound to the TBTA functionalized TentaGel displayed high activity with minimal leaching. Solid supports, including TentaGel, can be adapted for use in microreactors by fabricating packed-bed microreactors and directly injecting the suitable resin into the microreactor. These reactors, however, suffer from issues inherent with packed bed systems, e.g., high pressure drops, channeling, and changes in resin swelling with different solvents.

An alternative approach is to immobilize the Cu(I) catalyst onto the microfluidic device itself. Sui et al. developed a facile method to functionalize intact polydimethylsiloxane (PDMS) devices using an acidic hydrogen peroxide solution and silanes.[18] This method, or similar procedures, have been used to immobilize anti-fouling agents[19], proteins[20], DNA[21], and galactose[22] onto PDMS surfaces. However, these functionalized PDMS features are primarily used for biological assays or to prevent analyte loss/microchannel fouling. A similar immobilization procedure was adopted here to immobilize a TBTA derivative to PDMS-glass microreactors to enable chelation and stabilization of Cu(I) in the +1 oxidation. These PDMS-glass microreactors with immobilized Cu(I) are also called "click chips". From an application perspective, the research reported here is unique because intact microreactors were functionalized with a chelated metal catalyst for synthetic applications. To the best of my knowledge there is only one report of immobilizing a metal catalyst to the surfaces of a PDMS-based microreactor, this involved nanoparticles rather than a metal-chelate complex.[23]

A key component of this research was to develop and evaluate a novel TBTA derivative with improved water solubility, capable of attachment to a silane functionalized microreactor. The immobilization process was characterized by both X-ray photoelectron spectroscopy (XPS) and radiotracer studies. The microreactor was validated by testing "click" reactions involving azides and alkynes, and the "click chip" demonstrated improved reaction yields compared to conventional techniques. To the best of my knowledge, this represents the first report of a microreactor incorporating an immobilized Cu(I) catalyst useful for bioconjugation, and where the fabrication procedure is amenable for development of high-density, integrated microfluidic platforms.

2.2 Results and discussion

Microreactor design

The microreactor was fabricated out of PDMS and glass for the following two reasons: (1) availability of simple, well-established methods for fabrication based on soft lithography, and (2) accessibility of multiple strategies for surface functionalization via creation of reactive silanol groups followed by silane attachment. Sui, et al.'s previous work in particular provided a facile method to form reactive silanol groups in intact PDMS devices for subsequent silanization.[18] Deep reactive ion etching (DRIE) was found to produce more robust silicon masters than traditional SU-8 based masters since the DRIE fabricated masters contained a fluorocarbon layer that provided easier liftoff of the PDMS imprints. Scanning electron microscope (SEM) was used to analyze masters and PDMS imprints. The resulting PDMS imprints from DRIE fabricated masters displayed no loss of posts after multiple uses of the masters (**Figure 2.1A**) while PDMS imprints made from traditional SU-8 based masters exhibited missing posts with continued use of the masters (**Figure 2.1B**). When fabricating microreactors with dense features, it may be more efficient to etch silicon using DRIE and then apply a fluorocarbon layer rather than attempt to optimize a process based on traditional SU-8 soft lithography techniques.

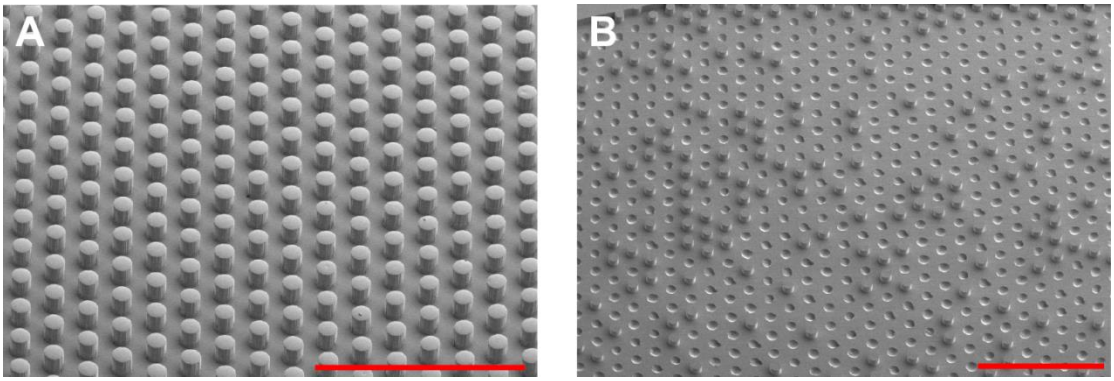

Figure 2.1. SEM images of a tank with PDMS posts from PDMS imprints using masters created by DRIE (A) and standard SU-8 photolithography techniques (B), illustrating the loss of posts and the hexagonal packing scheme. Both scale bars are 1 mm.

The microreactor design (**Figure 2.2**) included two key features: (1) posts and (2) reservoirs. The posts were placed in a hexagonal packing scheme (**Figure 2.1**) with a 200 μm center-to-center distance from one post to any adjacent post. The posts served primarily to reduce reagent diffusion distances to a catalytic site while also slightly increasing the available surface area for immobilization of the catalyst (~30% increase compared to a device without posts). The diffusion time of reagents can be approximated by:

$$t_D \approx \frac{l^2}{D} \tag{2.1}$$

where t_D is the approximate diffusion time of reagents, l is the characteristic length, and D is the diffusion coefficient. With 100 μm diameter PDMS posts spaced 100 μm apart (edge of one post to edge of adjacent post) the approximate diffusion time of reagents to an active catalytic site is therefore approximately 25 s (**Equation 2.1**, $t_D \approx (50\ \mu m)^2\ (10^{-10}\ m^2\ s^{-1})^{-1}$), significantly shorter than the typical overall incubation time (>10 min). Using **Equation 2.1**, diffusion times for a device without posts would be roughly 40 seconds with respect to the microreactor bottom and top, but it would take hours to diffuse to the sides of a reservoir. The microreactor contained five reservoirs with an average height of 125.99 ± 1.61 μm (n = 13) to provide an adequate sample volume (~46 μL) for analysis. The height and/or number of tanks can be easily adjusted to provide the desired sample volume with minimal pressure drop compared to scaling up channel-based microreactors. Additionally, if the number of reservoirs changed, the surface area-to-volume ratio is maintained, providing the possibility of adjusting sample volume with minimal changes in relative amount of immobilized catalyst.

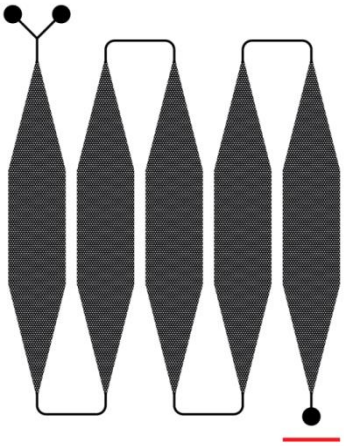

Figure 2.2. CAD image of the "click chip" design used for all experiments in Chapter 2. The chip has five reservoirs to provide adequate sample volume for analysis, and each reservoir is filled with 100 μm diameter posts to reduce diffusion time of reagents to an active catalyst site. The scale bar is 5 mm.

Ligand immobilization and characterization

The TBTA-Cu(I) complex has been shown to be an efficient catalyst for "click" reactions.[5, 14] The Cu(I) state is unstable under normal oxidative conditions, but can be stabilized by complexation with the tetradentate TBTA ligand.[4, 5] The TBTA ligand has been immobilized on different polymeric materials, e.g., TentaGel[14] and polystyrene[24], to afford an active Cu(I) catalyst source for "click" reactions. One major challenge of the original TBTA developed by Chan et al. from the standpoint of biomolecule compatibility is the limited water solubility of TBTA. To address this issue a series of TBTA derivatives (data not shown) were developed and a water-soluble TBTA derivative (ligand **2**) was determined to be the optimal choice for Cu(I) immobilization. The synthesis of ligand **2** started from a "mono-click" reaction of tripropargylamine and 11-azido-3,6,9-trioxaundecan-1-amine in the presence of the Cu(I) catalyst tetrakis(acetonitrile)copper(I) hexafluorophosphate to afford mono-PEG linker substituted intermediate **1** in 29.7% yield. A second "click" reaction between intermediate **1** and 8-azido-3,6-dioxaoctanol afforded the water-soluble TBTA derivative, ligand **2**, in 31.6% yield (**Scheme 2.1**).

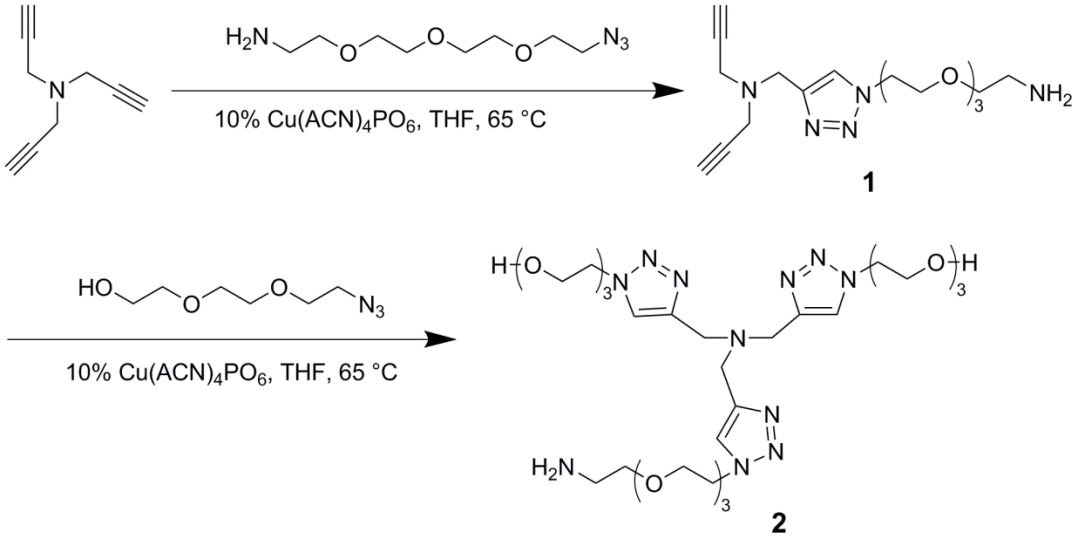

Scheme 2.1. Synthesis of a water-soluble TBTA derivative, ligand **2**.

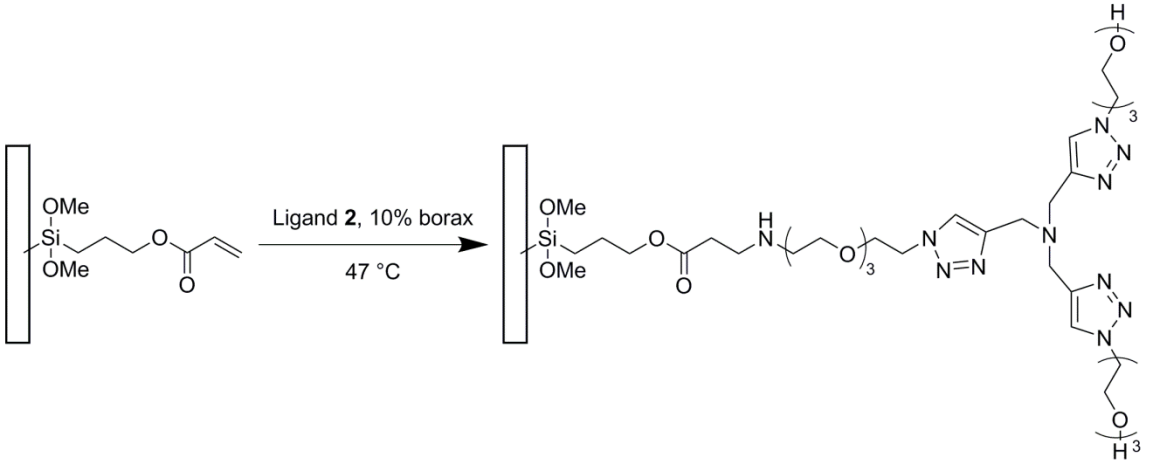

Scheme 2.2. Immobilization of ligand **2** on chip surfaces.

Ligand **2** was successfully immobilized onto the surface of microreactors (**Scheme 2.2**) by first activating the surface with an acidified hydrogen peroxide solution, then covalently bonding the silane 3-(trimethoxylsilyl)propyl acrylate (TMSPA) to the activated surface groups, followed by attaching ligand **2** to the TMSPA. Finally, an aqueous Cu(I) solution was injected to form the Cu(I)-ligand **2** complex (see materials and methods section for more details). XPS was utilized to validate each step of the immobilization process on glass and PDMS substrates. The four

individual steps tested using XPS were: (1) non-functionalized substrate (control), (2) substrate + TMSPA, (3) substrate + TMSPA + ligand **2**, and (4) substrate + TMSPA + ligand **2** + Cu(I).

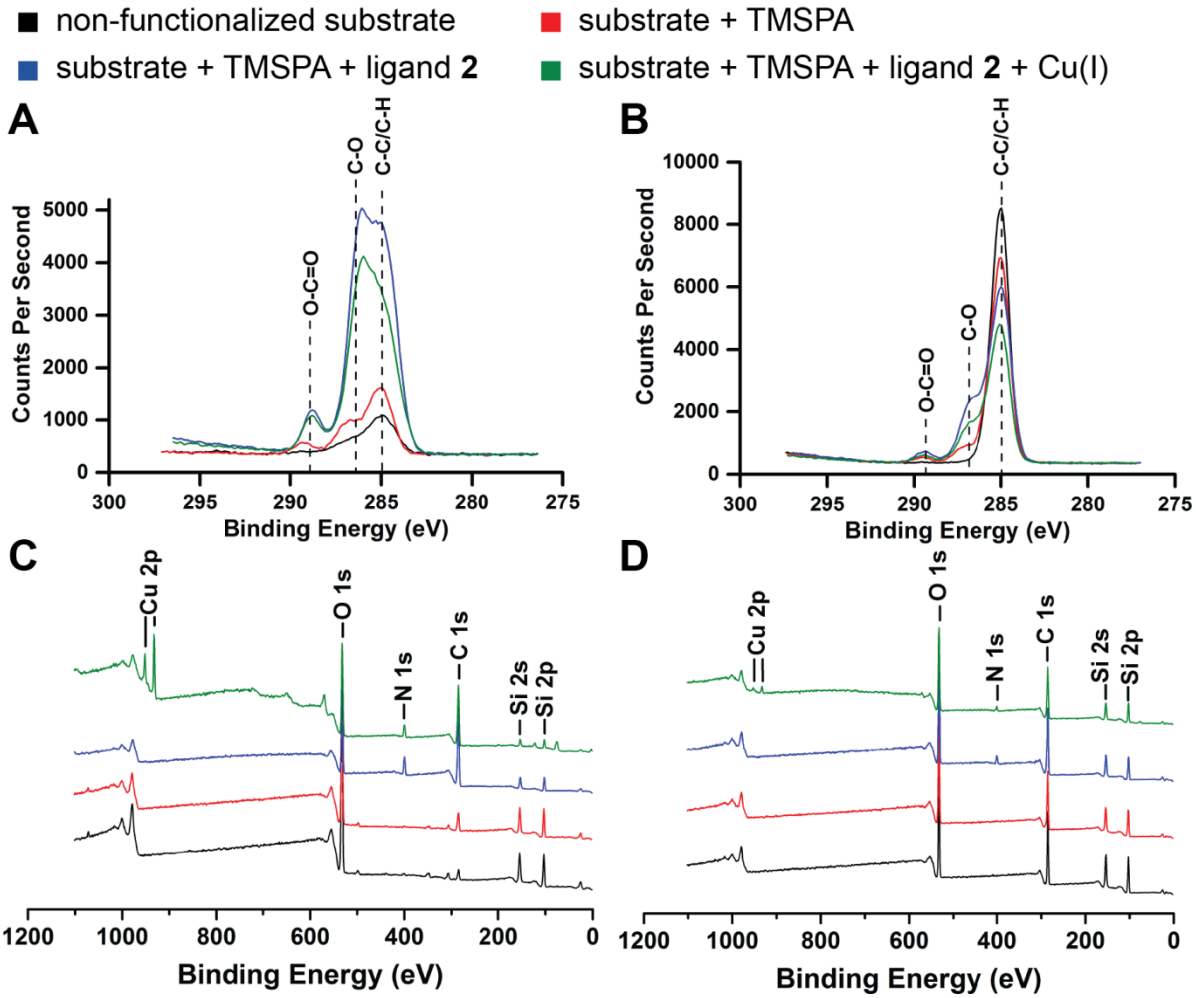

Figure 2.3. C1s narrow scan spectra of glass (A) and PDMS (B) and survey spectra of glass (C) and PDMS (D) at each stage of functionalization: non-functionalized substrate (black); substrate + TMSPA (red); substrate + TMSPA + ligand **2** (blue); substrate + TMSPA + ligand **2** + Cu(I) (green).

Two types of XPS spectra, survey spectra covering a wide range of binding energies to determine what elements were present and narrow scan spectra to analyze the various states of specific elements, were performed and analyzed. C1s narrow scan spectra of glass (**Figure 2.3A**) and PDMS (**Figure 2.3B**) substrates after covalent bonding of TMSPA to activated surface groups indicated TMSPA was successfully bonded based on (1) a new characteristic peak (red lines vs. black lines) at ~289 eV that corresponds well to the O-C=O carbon found in acrylate

groups and (2) a new or relatively larger peak (red lines vs. black lines) at ~286 eV indicative of C-O bonds. The C1s narrow scan spectra also demonstrated successful bonding of ligand **2** to TMSPA for both glass and PDMS substrates (**Figure 2.3A** and **B**) because of the increase in size of the ~286 eV peak (C-O bond) relative to other peaks in the C1s spectra (blue or green lines vs. red or black lines) that indicates the presence of ethylene glycol moieties of polyethylene glycol (PEG) chains in ligand **2**. Survey scan spectra of glass (**Figure 2.3C**) and PDMS (**Figure 2.3D**) substrates after attaching ligand **2** (blue and green lines) also supported the conclusion that ligand **2** was successfully immobilized based on a substantial N1s peak at ~400 eV that is best explained by the triazole moieties in ligand **2**.

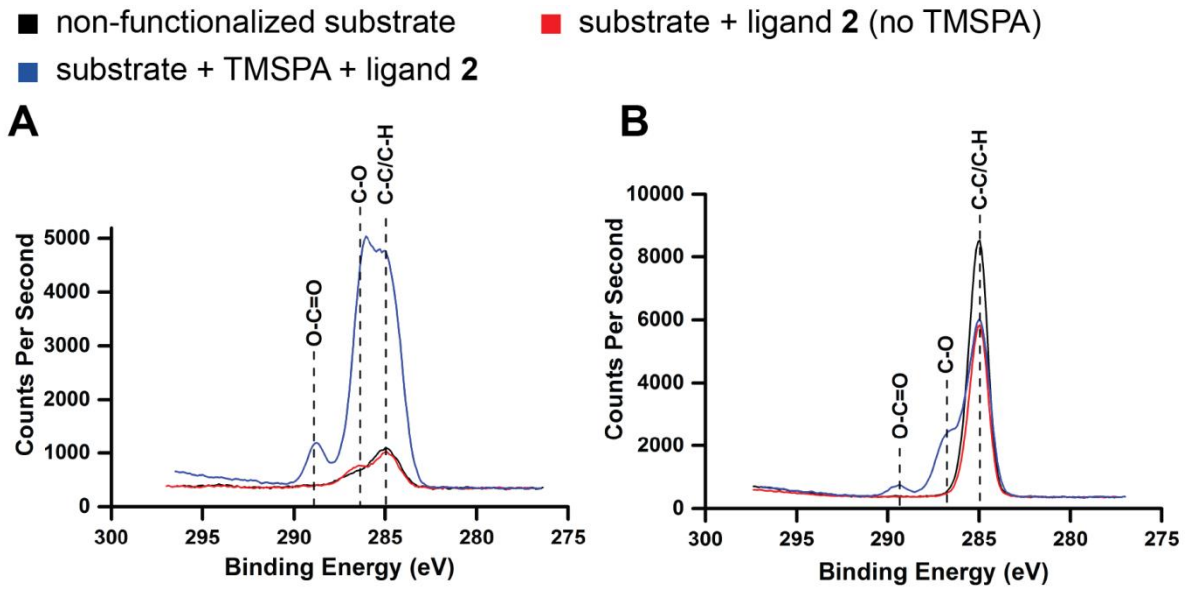

Figure 2.4. C1s narrow scan spectra of glass (A) and PDMS (B) after ligand **2** was incubated on both substrates without activating the surfaces with an acidified hydrogen peroxide solution and covalently bonding TMSPA to the surfaces. The black lines (non-functionalized substrate) and blue lines (substrate + TMSPA + ligand **2**) are the same used in **Figure 2.3** and are present for comparison purposes.

A negative control study was also performed to demonstrate the silanization process was essential for ligand **2** immobilization onto glass (**Figure 2.4A**) and PDMS (**Figure 2.4B**) surfaces. For this experiment the first two steps of the immobilization process (surface activation and TMSPA attachment) were skipped, and ligand **2** was directly incubated on both glass and

PDMS. The near identical profiles of the black lines (non-functionalized substrate) relative to the red lines (substrate + ligand **2** (no TMSPA)) in **Figure 2.4** indicate ligand **2** was not successfully bonded to either the glass or PDMS surface and was washed away during the rinse step. Therefore, the TMSPA is critical for permanent attachment of ligand **2** to both glass and PDMS surfaces.

Finally, XPS also confirmed the presence of copper and provided information on the oxidative state of the copper chelated to ligand **2**. The presence of Cu2p peaks in the survey spectra (green lines) of glass (**Figure 2.3C**) and PDMS (**Figure 2.3D**) demonstrate the presence of Cu on both samples. Furthermore, the presence of a symmetrical $Cu2p_{3/2}$ peak and the lack of shake-up peaks in the Cu2p narrow scan spectra of both glass (**Figure 2.5A**) and PDMS (**Figure 2.5B**) samples, indicate the copper oxidation state is either Cu(0) or Cu(I) but not Cu(II).[25]

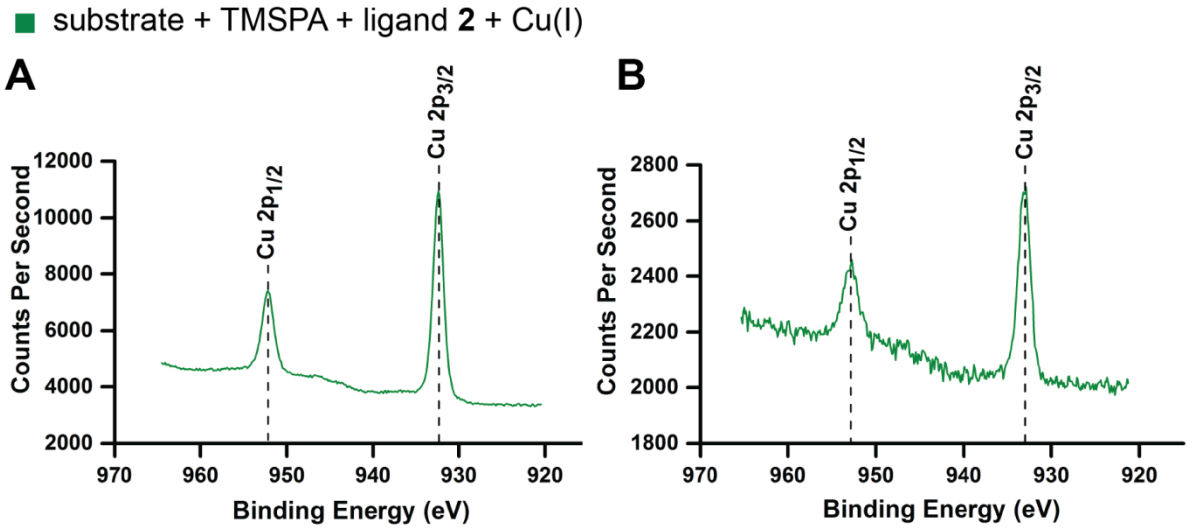

Figure 2.5. Cu2p narrow scan spectra of glass (A) and PDMS (B) after Cu(I) chelation to immobilized ligand **2**.

Microreactors with ligand **2** attached had a colorless appearance. However, after immobilization of Cu(I), the “click chips" displayed a visibly yellow appearance. The amount of ligand **2** immobilized on the chip was quantified via radiotracer methods. Using a carrier-added

Cu(I) solution that consists of a known concentration of cold copper with a trace amount of radioactive Cu-64, the amount of bound copper was determined by measuring the radioactivity of the chips. This value also roughly estimates the amount of ligand **2** immobilized onto the chip surface assuming the active catalyst was a 1 : 1 complex of Cu(I) and ligand **2** and little non-specific binding. Microreactors with five tanks filled with posts and functionalized with ligand **2** had 1136 ± 272 nmol of immobilized Cu(I) (n = 3). After accounting for the internal microreactor surface area, the immobilized Cu(I) density was 81 ± 20 nmol cm^{-2}.

Because a previous study demonstrated that copper could adsorb onto the surface of PDMS-based chips[26], a control study was performed to measure the non-specific binding of Cu(I) onto PDMS-glass microreactor surfaces. The various chemical modifications involved with the immobilization of ligand **2** makes it difficult to choose an ideal control model for the surface adsorption of copper. A plain chip without any functionalization was chosen as the control model, but results may have greater amounts of non-specifically bound Cu(I) than the actual "click chip" with immobilized ligand **2** because the TMSPA occupies potential Cu(I) binding sites on the glass and PDMS surfaces. Control chips with no surface treatment were treated with a radioactive Cu(I) buffer solution using the same process used for "click chips". Low amounts of Cu-64 (36-48 μCi, decay corrected) were observed on the chip indicating low amounts of non-specific binding of copper onto the PDMS and glass surfaces (380 ± 55 nmol). After treatment with an ethylenediaminetetraacetic acid (EDTA) solution (0.05 M, pH 6), only minimal amounts of copper (7-10 μCi, decay corrected) remained on the chip, which corresponded to a copper density of 6 ± 1 nmol cm^{-2}.

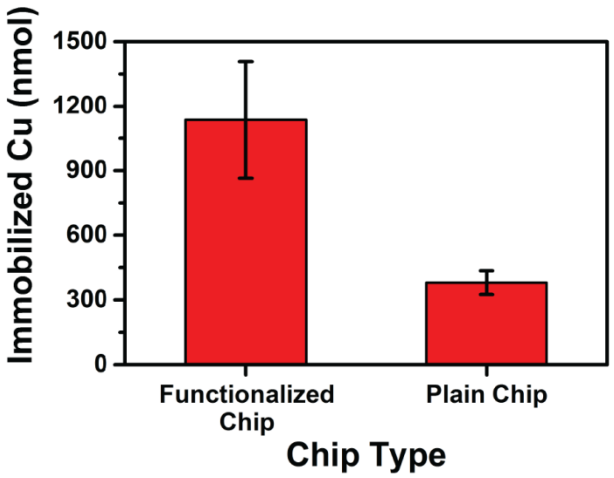

Figure 2.6. Carrier-added Cu(I) solution was injected into chips with immobilized ligand **2** (functionalized chip) and chips with no surface modifications (plain chip). After rinsing the devices the activity was quantified and used to calculate the amount of copper present. Data is presented as the mean ± standard deviation (n = 3).

"Click" reactions on chip

To validate the "click chip", reactions between Flu568-azide and propargylamine or Flu568-acetylene and an azide derivative of the small peptide, *cyclo*[Arg-Gly-Asp-D-Phe-Lys] (cRGDfK-azide), were tested on chip (**Scheme 2.3**). Flu568-azide/acetylene are derivatives of a common dye, chosen because the compounds are easily detected by the UV-Vis detectors on high-performance liquid chromatography (HPLC) set-ups. Propargylamine is a widely used alkyne to test "click" reactions and cRGDfK-azide is a small peptide, easily synthesized, that is useful for characterizing "click" reactions with biomolecules.

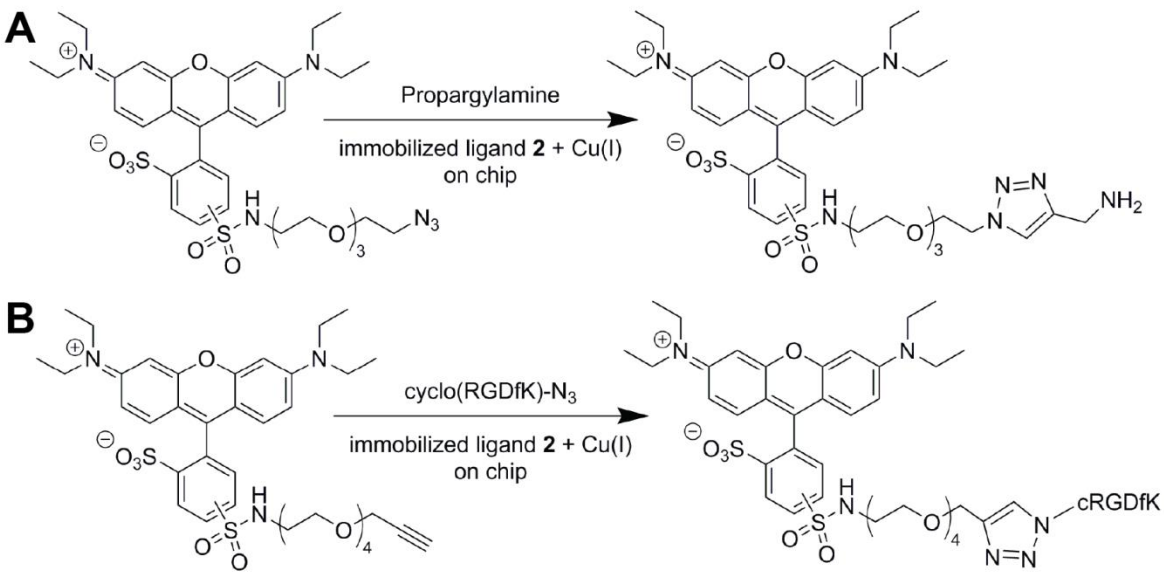

Scheme 2.3. Reactions between Flu568-azide and propargylamine (A) and Flu568-acetylene and cRGDfK-azide (B) were used to validate the "click chip".

Initial tests were performed with Flu568-azide and propargylamine. Reaction yield increased with prolonged incubation period on a "click chip". The yield after a 15 min incubation time (55 ± 9%) increased to 76 ± 8% after incubating for 30 min, and increased to 83 ± 4% after 50 min in a "click chip" (**Figure 2.7A**). The same reaction (Flu568-azide and propargylamine) was tested on a different "click chip" and similar yields (e.g., 52 ± 7% for 15 min reaction) were achieved, indicating the functionalization process is reproducible.

The same Flu568-azide and propargylamine reaction was also testing using a conventional set-up (reaction vials on a ThermoMixer) using the same reaction conditions (i.e., reactant concentration, volume, time, and temperature). The yield was only 12 ± 2% with 60 mol% of Cu(I)-TBTA catalyst after incubating for 15 min (**Figure 2.7B**). The yield did increase to 81 ± 3% in the presence of a large excess of catalyst (~2000 mol%) (**Figure 2.7B**). However, using this conventional approach with an excess of catalyst would require a purification step to remove the catalyst that is not required after reactions on the "click chip" because Cu(I) is chelated to the

immobilized ligand **2**. Additionally, the results from the "click" reaction using the conventional set-up clearly indicate the "click chip" surface is immobilized with sufficient active catalyst to promote the tested "click" reaction in a short period of time (~10s min).

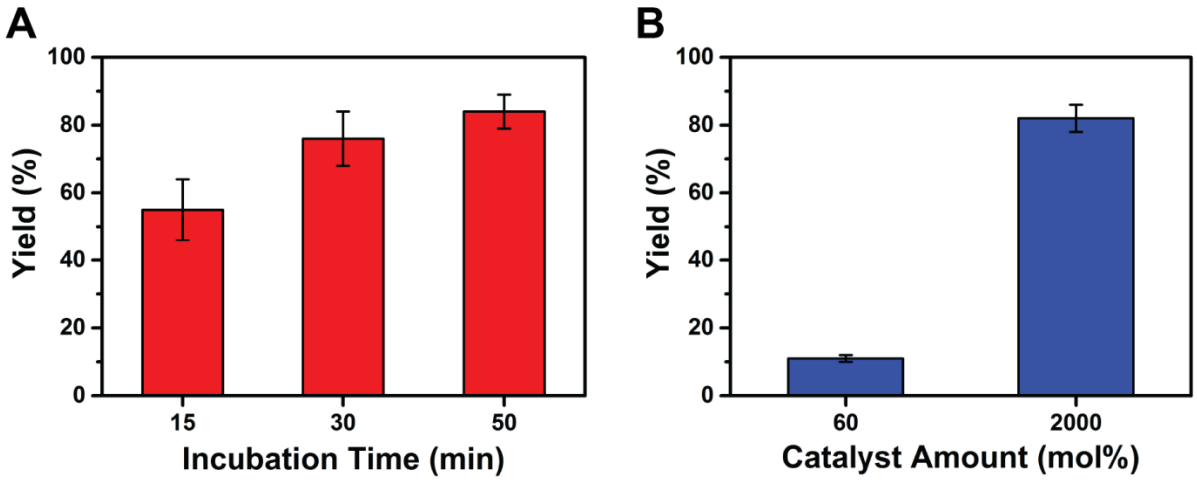

Figure 2.7. "Click" reaction of Flu568-azide and propargylamine at 37 °C using a "click chip" after an incubation time of 15, 30, or 50 min (A) and using a conventional set-up after an incubation time of 15 min with different concentrations of catalyst (B). Data is presented as the mean ± standard deviation (n = 3-4).

To confirm the Cu(I)-ligand **2** complex was the active catalyst, the "click" reaction between Flu568-azide and propargylamine was performed on a plain chip without immobilized ligand **2**. A Cu(I)-ascorbate solution was pumped through the chip, then the chip was washed with DI water. When reagents were incubated on the plain chip for 15 min the nonspecifically bound Cu(I) catalyzed the reaction, but with a lower yield (16 ± 5%) compared to the "click chip" (55 ± 9%). Even when the reaction was repeated on the same control chip with a 30 min incubation time, the reaction yield (7 ± 2%) was still much lower than reactions on the "click chip" (76 ± 8%) (**Figure 2.8**). These results strongly indicate the immobilized Cu(I)-ligand **2** complex is the active catalyst while adsorbed Cu(I) only plays a minor role in catalyzing "click" reactions.

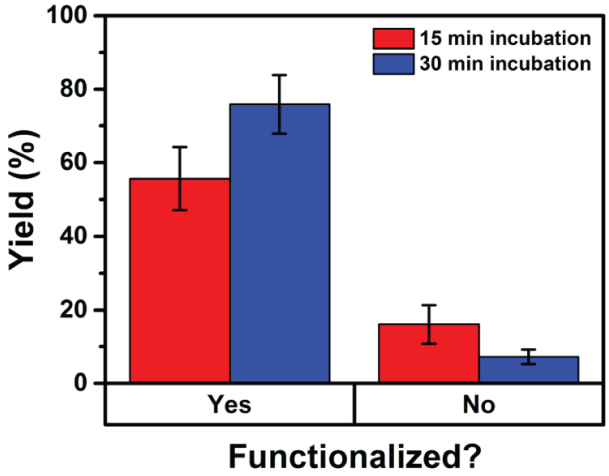

Figure 2.8. "Click" reaction between Flu568-azide and propargylamine in a functionalized chip ("click chip") or a chip without immobilized ligand **2** incubated for 15 min (red bars) or 30 min (blue bars). Data is presented as the mean ± standard deviation (n = 4).

The functionalization of "click chips" remained effective for at least one month as long as the Cu(I) catalyst was regenerated periodically. Flu568-azide and propargylamine "click" reactions were performed on the same "click chip" on different days to study the shelf-life of the ligand **2** immobilized chip. Reaction yields 0, 1, 3, 7, and 10 days after the initial addition of Cu(I) solution into the chip were similar. Additionally, the reaction yield 10 days after the initial addition of Cu(I) solution (48 ± 5%) was similar to yield for the initial reaction on day 0 (55 ± 9%), even after three additional injections of Cu(I) into the "click chip". Furthermore, the yield of Flu568-azide and propargylamine "click" reactions after 30 min of incubation time on a "click chip" (76 ± 8%) could be repeated ~20 days later with near identical yields (77 ± 6%) on the same chip. The reaction yield remained above 80% (50 min incubation time) after one month of using the same "click chip". After five regenerations of the Cu(I)-ligand **2** catalyst, however, the reaction yield decreased, and the tank surface became discolored in some spots which indicated ligand **2** may have detached from the surface.

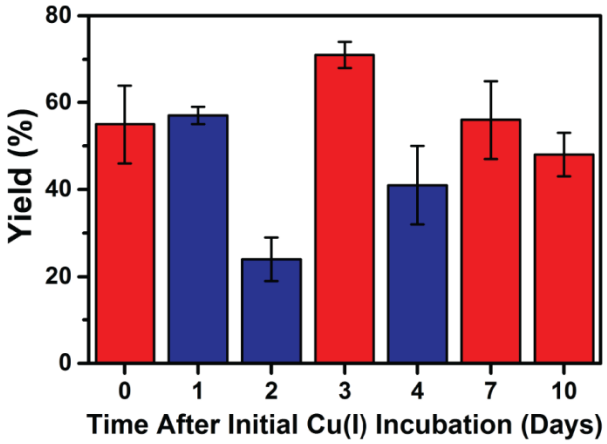

Figure 2.9. Reaction between Flu568-azide and propargylamine on the same "click chip" for 15 min at 37 °C over several days. Cu(I) was regenerated periodically prior to the first reaction on some days (red bars) by injecting more Cu(I) solution into the "click chip". Blue bars represent days where Cu(I) was not re-injected into "click chip" and the chip was used as is. Data is presented as the mean ± standard deviation (n = 3-4).

To validate the application of the reactor for use with biomolecules, the "click" reaction between an azide containing peptide, cRGDfK-azide[27] and Flu568-acetylene was studied. This reaction was performed five times on a "click chip" (30 min incubation time) with only small deviations in product yield (75 ± 3%) (**Figure 2.10**). The reported reaction yield was based on the conjugated peptide and not on the loss of Flu568-acetylene because some Flu568-acetylene was converted into an uncharacterized byproduct (HPLC elution time of 13.4 min). The byproduct likely arose from a reaction between the Flu568-acetylene and the Cu(I) catalyst. The same byproduct was also observed in the conventional reaction, when Flu568-acetylene and cRGDfK-azide were mixed with Cu(I)-TBTA at 37 °C. The conventional reaction of cRGDfK-azide and Flu568-acetylene with 60 mol% catalyst afforded a product yield of 54 ± 5%, which was lower than the same reaction on a "click chip" (75 ± 3%) (**Figure 2.10**). These results confirm a biomolecule (RGD peptide) was compatible with the catalyst-immobilized chip, and a higher yield could be achieved using the "click chip" compared to conventional techniques.

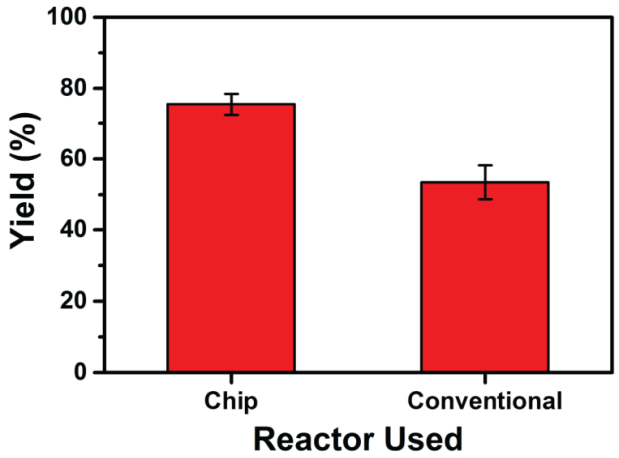

Figure 2.10. "Click" reaction between Flu568-acetylene and cRGDfK-azide in a "click chip" with immobilized ligand **2** and a conventional reactor. Reactions were incubated for 30 min at 37 °C. Data is presented as the mean ± standard deviation (n = 3-5).

2.3 Materials and methods

All solvents and chemical reagents were purchased from Sigma-Aldrich or Fisher Scientific unless specified. All chemicals were used without further purification. Flu568-azide and Flu568-acetylene were purchased from Click Chemistry Tools. Deionized (DI) water was produced in-house using either the water purification system maintained at the Micro-Nano-Mechanical Systems Cleanroom at the University of Illinois (all wafer fabrication steps), or a Barnstead e-Pure filtration system (UIUC) or a Millipore Milli-Q water purification system (Wash U) for all other methods. $^{64}CuCl_2$ was produced at Washington University in St. Louis School of Medicine, and obtained in a 0.1 M HCl solution. Silicon wafers were purchased from University Wafer. AP-8000 adhesion promoter and SPR220-7.0 were purchased from MicroChem, and used for fabricating silicon master templates. Sylgard 184 PDMS was purchased from Dow Corning. Glass microscope slides were purchased from Fisher Scientific, and used to manufacture PDMS reactors. Microbore polytetrafluoroethylene (PTFE) tubing (0.012" ID, 0.030" OD) was purchased from Cole-Parmer. Silica TLC plates and C18 TLC silica plates were purchased from Sorbent Technologies. ^{1}H NMR and ^{13}C NMR spectrometry were performed on an I400 Varian

Inova NMR instrument (400 MHz for ^{1}H NMR and 100.5 MHz for ^{13}C NMR). MALDI-TOF mass spectrometry was performed on a Voyager-DE STR BioSpectrometry Workstation. High resolution electrospray ionization mass spectrometry was conducted on a Thermo Scientific LTQ Orbitrap Velos mass spectrometer with Xcalibur operating system. Three microliter flow modular pump components (syringe pump, a pump driver circuit, and a power supply) were obtained from Harvard Apparatus. A Kapton-insulated thin film heater (2" x 2"), Omega CN740 temperature controller and an Omega SA 1-RTD probe were obtained from Omega Engineering. The ThermoMixer C was purchased from Eppendorf North America. Microliter syringes were obtained from Hamilton Co. The Capintec CRC-712M radioisotope dose calibrator was purchased from Capintec Inc., and used for the measurement of radioactivity. X-ray photoelectron spectroscopy was performed on a Kratos Axis Ultra. Scanning electron microscope imaging was performed on a Hitachi S-4700 SEM with an acceleration voltage of 2 kV. Surface profilometer measurements were taken on an Alpha Step IQ profilometer. Analytical reverse phase HPLC was performed on a Hewlett Packard 1050 series (Model 35900E), and analyzed with Chem Station IC software. The HPLC analytical column was an Econosil C18 reverse phase column (10 µm, 250 mm) from Alltech Associates, Inc. The flow rate was 1 mL min^{-1} for analytical HPLC and 2.5 mL min^{-1} for semi-preparative HPLC, with the mobile phase of solvent A (0.1% TFA in water) and solvent B (0.1% TFA in acetonitrile). The UV detector was set at 576 nm. The gradient analytical HPLC method started at 25% B (0-5 min) and rose to 60% B (10-16 min), and returned to 25% B (16.5-20 min).

PDMS-glass chip fabrication

Lithography. Silicon wafers were rinsed, dried with filtered nitrogen, heated on a hot plate, and then cooled with filtered nitrogen. An adhesion promoter (AP-8000) was dispensed onto the

wafers and spin-coated in three consecutive steps: 500 rpm for 2 s, 1500 rpm for 2 s, and 3000 rpm for 30 s. Then SPR220-7.0 (5 mL) was dispensed onto the wafers and spin-coated in two consecutive steps: 500 rpm for 10 s and 2000 rpm for 30 s. The photoresist was soft baked on a hotplate for 30 s at 65 °C, 110 °C for 3 min, then 65 °C for 30 s, and finally cooled to room temperature for 3 min. The photoresist was exposed to UV light with an intensity of ~14 mW cm^{-2} through a transparency mask (FineLine Imaging, Colorado Springs, Colorado) and a quartz block for 15 s followed by a 1 min waiting period. The exposure process was repeated twice for a total exposure time of 45 s. Exposed photoresist was removed by vigorously swirling wafers in a solution of DI water/AZ400K developer for 1 to 3 min. Wafers were rinsed with DI water and dried with filtered nitrogen. The photoresist was then hard baked on a hot plate for either (1) 30 s at 65 °C, 3 min at 110 °C, and 30 s at 65 °C or (2) 3 min at 80 °C, to make the photoresist more resilient to etching.

Etching. Wafers were briefly cleaned with oxygen plasma, and etched using a Bosch process with a PlasmaTherm ICP-DRIE. After etching, the wafers were swirled for 10 min in 1165 PR stripper, then rinsed with acetone and isopropanol, and finally dried with filtered nitrogen. A flurocarbon passivation layer was deposited to prevent PDMS from adhering to the silicon.

Profilometer height measurement. After etching the silicon wafers and depositing a fluorocarbon passivation layer the etch heights were measured with a profilometer on the top of a vibration free table. Measurements were made over 13 different sections of the masters. Heights are expressed as the average ± standard deviation.

PDMS attachment to glass. Sylgard 184 reagent was combined in a 10 : 1 mass ratio (base/curing agent), mixed thoroughly, and degassed in a vacuum desiccator for ~20 min. The PDMS was poured into a petri dish containing the etched master, and cured in an oven at 65 °C

for ~2 h. The PDMS was peeled from the master, and the holes for inlets and outlets were punched using a 19 gauge hypodermic tubing with beveled edges. Glass slides were scrubbed with a Texwipe soaked in an aqueous Alconox solution, and rinsed with DI water, then dried with filtered nitrogen. The PDMS and glass were then exposed to oxygen plasma generated by an Atomflo atmospheric plasma system (Surfx Technologies) with power set at 100 W, helium flow at 15.0 L min^{-1} and oxygen flow at 0.30 L min^{-1}. PDMS and glass were slowly passed ~4 times under the plasma, while the oxygen plasma exited a nozzle which was held ~2 cm above the surfaces. The PDMS was immediately sealed to the glass and incubated in an oven at 65 °C overnight. **Figure 2.11** provides an illustration of the fabrication steps used to make PDMS-glass microreactors.

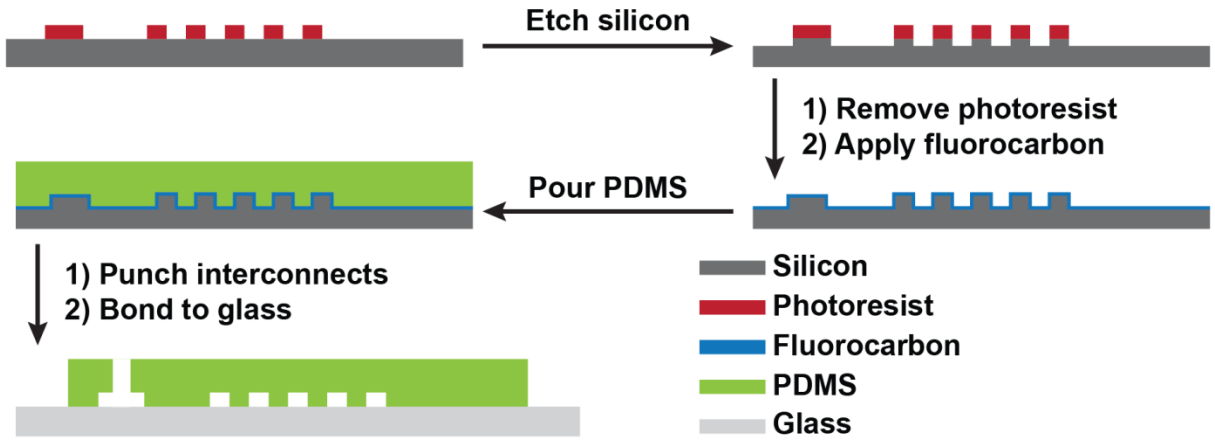

Figure 2.11. Schematic of the fabrication steps for making the PDMS-glass microreactors.

Synthesis of water-soluble TBTA ligand (ligand 2)

8-Azido-3,6-dioxaoctanol. 8-chloro-3,6-dioxaoctanol (5 g, 28.5 mmol) was dissolved in DI water (25 mL). Sodium azide (2.4 g, 36.9 mmol) was added to the reaction solution in three portions with caution. The reaction solution was refluxed at 105 °C for 48 h. After the reaction

solution cooled to room temperature, the solvent was removed under vacuum. The residue was washed with acetone (150 mL) to remove any solid salt. The liquid layer was dried over anhydrous sodium sulfate, and then concentrated. The product was further dried under vacuum overnight to afford a viscous yellow liquid (5 g, 96%). ^{1}H NMR (400 MHz, $CDCl_3$): δ 3.67-3.62 (m, 8H), 3.55 (t, J = 4.4 Hz, 2H), 3.34 (t, J = 4.4 Hz, 2H), 2.77 (br, 1H). ^{13}C NMR (100.5 MHz, $CDCl_3$): δ 72.36, 70.41, 70.14, 69.82, 61.46, 50.41.

*Intermediate **1***. Tripropargylamine (0.96 g, 7.34 mmol) and tetrakis(acetonitrile)copper(I) hexafluorophosphate (136.8 mg, 0.37 mmol) were dissolved in tetrahydrofuran (10 mL) in a 200 mL round-bottom flask under a nitrogen atmosphere. 11-azido-3,6,9-trioxaundecan-1-amine (0.4 g, 1.83 mmol) was dissolved in tetrahydrofuran (20 mL) and the solution was added to the reaction solution dropwise over 30 min at 40 °C. Then the reaction solution was refluxed at 66 °C for 18 h. After the reaction, the solution was cooled to room temperature. The product was purified by chromatography on a silica column eluting with methanol/dichloromethane (5 : 95), and then triethylamine/methanol/dichloromethane (2 : 10 : 88). The product was obtained as a yellow viscous liquid (0.19 g, 29.7%). ^{1}H NMR (400 MHz, $CDCl_3$): δ 7.74 (s, 1H), 4.85 (br, 2H), 4.54 (t, J = 5.0 Hz, 2H), 3.85 (t, J = 5.0 Hz, 2H), 3.79 (s, 2H), 3.67 (t, J = 4.8 Hz, 2H), 3.60-3.54 (m, 8H), 3.41 (d, J = 2.4 Hz, 4H), 3.09-3.00 (m, 4H), 2.29 (t, J = 2.2 Hz, 2H). ^{13}C NMR (100.5 MHz, $CDCl_3$): δ 143.64, 124.25, 78.21, 73.67, 70.06, 70.01, 69.91, 69.79, 69.26, 66.38, 50.00, 47.61, 45.70, 41.63. MALDI-TOF: calcd for $C_{17}H_{27}N_5O_3$ $[M]^+$: 349.21; found: 349.26. HRMS (ESI): calcd for $C_{17}H_{28}N_5O_3$ $[M + H]^+$: 350.2187; found: 350.2186.

*Water-soluble TBTA ligand **2***. Intermediate **1** (0.19 g, 0.54 mmol), 8-azido-3,6-dioxaoctanol (0.23 g, 1.31 mmol) and tetrakis(acetonitrile)copper(I) hexafluorophosphate (81 mg, 0.22 mmol) were dissolved in tetrahydrofuran (5 mL) and refluxed at 66 °C under nitrogen flow. After 18 h,

the reaction solution was cooled to room temperature. The solution was mixed with QuadraPure^{TM} TU resin (0.3 g) in a 50 mL round-bottom flask for 3 h. The solution was filtered, and the crude product was concentrated and purified by chromatography on a silica column using a gradient elution solvent system (methanol/dichloromethane 5 : 95 to triethylamine/methanol/dichloromethane 2 : 20 : 78). The product was afforded as a yellow viscous liquid (0.12 g, 31.6%). ^{1}H NMR (400 MHz, $CDCl_3$): δ 8.06 (s, 2H), 8.04 (s, 1H), 4.60-4.58 (m, 6H), 3.92-3.90 (m, 6H), 3.75 (s, 6H), 3.63-3.56 (m, 20H), 3.51-3.49 (m, 6H), 3.20-3.12 (m, 2H). ^{13}C NMR (100.5 MHz, $CDCl_3$): δ 143.52, 124.86, 72.10, 69.87, 69.84, 69.67, 68.84, 66.37, 60.63, 49.84, 47.50, 46.86, 46.22. MALDI-TOF: calcd for $C_{29}H_{53}N_{11}O_9$ $[M]^+$: 699.40; found: 699.26. HRMS (ESI): calcd for $C_{29}H_{54}N_{11}O_9$ $[M + H]^+$: 700.4100; found: 700.4099; calcd for $C_{29}H_{55}N_{11}O_9$ $[M + 2H]^{2+}$: 350.7087; found: 350.7086.

Procedures and evaluation for ligand 2 immobilization on chip

Ligand immobilization. The PDMS-glass chip was activated with an acidified hydrogen peroxide solution (H_2O_2/HCl/H_2O 1 : 1 : 5, 4 mL) with a flow rate of 50 μL min^{-1}. Then the chip was washed with DI water (1 mL), and dried with air for 4 min. A neat solution of TMSPA was pumped into the activated microreactor at 50 μL min^{-1} for 20 min, then dried by injecting air. The silanized chip was annealed at 70 °C under vacuum for 2 h to cure the surface. Ligand **2** (19.5 mg, 29.8 μmol) was dissolved in a 10 mmol% borax solution (1.5 mL),[28] and the solution was sonicated for 20 min. The solution was pumped into the chip at a rate of 10 μL min^{-1} at 47 °C for 150 min. The immobilized chip was washed with water and methanol (2 mL for each solvent), the chip was then dried with air flow for 10 min.

XPS analysis. XPS experiments were performed using a monochromatic aluminum X-ray source (1486.6 eV). Pass energy was 160 eV for survey spectra and 40 eV for narrow scan

spectra. All spectra were collected at a photoelectron take-off angle of 90°. To account for sample charging a flood gun was utilized and the hydrocarbon C1s peak was referenced to 285.0 eV. Analysis was performed utilizing CasaXPS version 2.3.16 software. Shirley background subtraction was used for all analyses.

Substrates for XPS analysis were prepared in a similar fashion to "click chips". Activated chips could not be used for XPS analysis primarily because (1) chips consisted of permanently bound PDMS to glass slides and this bond is difficult to break without ripping the PDMS, (2) because thick PDMS outgasses under vacuum and requires extensive time for the XPS set-up to achieve the appropriate vacuum for use, and (3) samples must be able to fit on the XPS stage. Due to the second issue, 10:1 PDMS for XPS analysis was prepared by spin-coating on clean silicon wafers, then cured in a 65 °C oven for 2 h. After cooling to room temperature the PDMS was covered with Scotch tape and the silicon wafer with PDMS was snapped in half after scoring with a diamond tipped scribe. Glass pieces for XPS analysis were cut to ~37 x 37 mm in size.

The following process describes the general method used for the complete Cu(I) immobilization process of glass and PDMS substrates for XPS analysis. The process was stopped at different points for some substrates to analyze the surface after (1) attaching TMSPA, (2) bonding ligand **2** to the TMSPA, and (3) chelating Cu(I) to ligand **2**. Individual pieces were first cleaned by soaking in a crystallizing dish with methanol while swirling the dish by hand to mimic injecting the solution into a "click chip", all soaking steps where swirled in a similar fashion. Pieces were rinsed and soaked in DI water for 10 min, then dried with N_2. PDMS and glass substrates were soaked in an acidic hydrogen peroxide solution (same concentration used for "click chip" functionalization). Pieces were rinsed with water, methanol, and then water again and dried with N_2. The acidified hydrogen peroxide soak and rinsing process were repeated

two more times. Silicon isolators were attached to pieces (Grace Bio-Labs, 25 x 25 mm outside perimeter, 13 mm internal diameter cut out) to enable functionalization of a specific location to reduce the amount of ligand **2** used. Samples were then placed in a glove bag with TMSPA. The bag was filled with N_2 to prevent cross-linking of the TMSPA due to water in the air. 200 μL of TMSPA was added inside the silicon isolator and incubated for 1 h at room temperature. Substrates were then rinsed and soaked in methanol for 4 min, then dried with N_2 and placed in a 65 °C oven for 2 h. Substrates were allowed to cool to room temperature, rinsed with methanol, rinsed with water and then soaked in water.

To attach ligand **2** to the surface, a second silicon isolator was added on top of the first to prevent the ligand **2** and borax solution to come in contact with a glass cover during the incubation period. To that end a second silicon isolator was added on top of the first and 190 μL of ligand **2** (20 mM) and borax (100 mM) solution were added inside the silicon isolator, and a piece of glass slightly larger than the isolator was placed on top to seal the chamber. Glass microscope slides were placed on either side of the substrate and glass cover and clamped together using a binder clip. After incubating for 20 h at room temperature, the ligand **2** and borax solution was aspirated off then substrates were rinsed with water then methanol, soaked in methanol for 6 min then soaked in water for 6 min and dried with N_2. A Cu(I) solution (5 mM $CuSO_4$ and 100 mM sodium ascorbate) was prepared and 250 μL of Cu(I) solution was added to the silicon isolator and incubated for 30 min. The Cu(I) solution was aspirated off and the Cu(I) incubation step was repeated once more. Finally the substrates were rinsed with water, soaked in water for 5 min, and dried with N_2. All substrates were trimmed to slightly larger than the 13 mm diameter hole from the silicon isolator using a diamond tipped scribe and breaking along the scored lines. This ensures all pieces will fit on the XPS stage.

Quantifying immobilization efficiency. Plastic syringes and Eppendorf tubes were washed with nitric acid (1 N) three times to remove any non-specifically bound metals. They were then washed with DI water followed by acetone, and dried with air. A Cu-64 stock solution was prepared in sodium acetate buffer (pH 5.5, 0.1 M). Carrier-added Cu(I) solution was prepared by adding a 100 mM sodium ascorbate solution to a 10 mM radioactive copper sulfate solution with specific activity of ~130 Ci mol^{-1}. The radiolabeling process was performed at room temperature. The carrier-added radioactive Cu(I) solution (~500 µCi) was pumped into the chip at a rate of 20 µL min^{-1} for 30 min, then the chip was cleaned with DI water thoroughly (4 mL), and dried under air flow. All PTFE tubing was removed, and the radioactivity of the chip was quantified (120-190 µCi, decay corrected). The calculated amount of immobilized Cu(I) was 1136 ± 272 nmol, and the density of Cu(I) was 81 ± 20 nmol cm^{-2}.

Control study with nonspecific binding of Cu-64. A non-functionalized chip of the same design was cleaned with methanol and water separately at 50 µL min^{-1} for 10 min. Carrier-added Cu(I) solution was prepared by adding 100 mM sodium ascorbate solution to a 10 mM radioactive copper sulfate solution with a specific activity of ~110 Ci mol^{-1}. The carrier-added radioactive Cu(I) solution (~500 µCi) was pumped into the chip at a rate of 20 µL min^{-1} for 30 min, then the chip was cleaned with DI water thoroughly (4 mL), and dried under air flow. All PTFE tubing was removed, and the radioactivity of the chip was quantified. The original tubing was then re-inserted into the chip. To determine the amount of removable copper bound to the surface, an EDTA solution (pH 6, 0.05 M, 1 mL) was pumped into the chip at 30 µL min^{-1}. Then all tubing was removed and the radioactivity of the chip was quantified (7-10 µCi, decay corrected). The remaining amount of copper adsorbed on the surface was 6 ± 1 nmol cm-^{2}.

General procedures for conventional and on chip "click" reactions

On chip "click" reactions. 100 µM stock solutions of Flu568-azide and Flu568-acetylene were prepared in an ammonium acetate buffer (pH 6.8, 0.1 M) with 1% sodium dodecyl sulfate to increase the solubility. The solution was sonicated for 10 min. Propargylamine stock solution was prepared as 400 µM in an ammonium acetate buffer. The synthesis of cRGDfK-azide peptide was reported previously,[27] and prepared as a 600 µM solution in an ammonium acetate buffer. The reaction solution consisted of equal volumes of two reagent stock solutions, and was pumped into chips from one inlet. The second inlet was connected to a syringe filled with ammonium acetate buffer. Prior to the first reaction and some subsequent reactions, chips with immobilized ligand **2** were activated by injecting a 5mM Cu(I) solution into the chips prepared from 10 mM copper sulfate and 200 mM sodium ascorbate solutions. After injecting Cu(I) into "click chips", they were washed thoroughly with DI water (5 mL). Then the reagent solution was pumped into the chip at a flow rate of 25 µL min^{-1}. The reactant flow was controlled by a microliter flow modular pump system. Reagent solutions were incubated on chip at 37 °C for 15, 30, or 50 min. After the reaction, the product was eluted from the chip by flowing ammonium acetate buffer into the chip. The chip was further washed with buffer (500 µL) to remove any reaction residue. The reaction was repeated for 4-6 times under the same conditions. The active catalyst immobilized on the chip could be repeatedly regenerated with 5 mM Cu(I) solution as described previously. The products were analyzed by reverse-phase HPLC, and characterized by MALDI-TOF mass spectrometry. The "click" products of the reaction between Flu568-azide and propargylamine were determined by HPLC with yields of 54 ± 9% (15 min incubation time), 76 ± 8% (30 min), and 82 ± 4% (50 min). MALDI-TOF: calcd for $C_{38}H_{51}N_7O_9S_2$ $[M]^+$: 813.32, found: 813.02; $C_{38}H_{50}N_7NaO_9S_2$ $[M + Na - H]^+$: 835.30, found: 834.90. The "click" product of

the reaction between Flu568-acetylene and cRGDfK-azide was quantified by HPLC (yield 75 ± 3%, 30 min incubation time). MALDI-TOF: calcd for $C_{65}H_{88}N_{14}O_{17}S_2$ $[M]^+$: 1400.02, found: 1400.79; $C_{65}H_{87}N_{14}NaO_{17}S_2$ $[M + Na - H]^+$: 1422.57, found: 1422.79.

Conventional "click" reactions. A Cu(I)-TBTA stock solution was prepared by mixing copper sulfate (10 mM, 12.5 µL), sodium ascorbate solution (50 mM, 12.5 µL) and tris[(1-benzyl-1H-1,2,3-triazol-4-yl)methyl]amine (20 mM, 16 µL). Flu568-azide or Flu568-acetylene (100 µM, 250 µL) and propargylamine (400 µM, 250 µL) or cRGDfK-azide (600 µM, 250 µL) were mixed well, and 60 mol% Cu(I)-TBTA catalyst was added to the reaction solution. The solution was shaken and incubated at 37 °C for 15 min (**Figure 2.7B**) or 30 min (**Figure 2.10**). The product was analyzed by reverse-phase high-performance liquid chromatography. The "click" product of the reaction of Flu568-azide and propargylamine was examined by HPLC with yield 12 ± 2%. MALDI-TOF: calcd for $C_{38}H_{51}N_7O_9S_2$ $[M]^+$: 813.32, found: 813.94; $C_{38}H_{50}N_7NaO_9S_2$ $[M + Na - H]^+$: 835.30, found: 835.78. The "click" product of the reaction of Flu568-acetylene and cRGDfK-azide was examined by HPLC with a yield of 54 ± 5%. MALDI-TOF: calcd for $C_{65}H_{88}N_{14}O_{17}S_2$ $[M]^+$: 1400.59, found: 1400.79; $C_{65}H_{86}N_{14}NaO_{17}S_2$ $[M + Na - 2H]^+$: 1421.56, found: 1421.76.

2.4 Conclusions

In this work, a new water-soluble TBTA derivative (ligand **2**) was synthesized to not only chelate and stabilize Cu(I) in the +1 oxidation state for "click" reactions, but also to enable immobilization onto a PDMS-glass microreactor. The fabricated "click chip" with immobilized Cu(I)-ligand **2** complexes, obviates the need to separate copper species from products, and eliminates side reactions of the copper reductant, typically ascorbate, with sensitive biomolecules. The Cu(I) catalyst was regenerated on chip five times without losing catalytic

efficiency. The model “click” reaction of Flu568-azide and propargylamine was studied on chip as a proof-of-principle reaction. The on chip reaction yield reached ~82% with a 50 min incubation time at 37 °C. A “click” compatible peptide, cRGDfK-azide, was then reacted with the dye Flu568-acetylene, and a yield of ~75% was achieved. These results highlight the potential of the “click chip” for the biomolecule-based “click” reactions.

2.5 References

(1) Nwe, K., and Brechbiel, M. W. (2009) Growing applications of "click chemistry" for bioconjugation in contemporary biomedical research. *Cancer Biother. Radiopharm. 24*, 289-302.

(2) Best, M. D. (2009) Click chemistry and bioorthogonal reactions: unprecedented selectivity in the labeling of biological molecules. *Biochemistry 48*, 6571-84.

(3) Rostovtsev, V. V., Green, L. G., Fokin, V. V., and Sharpless, K. B. (2002) A stepwise huisgen cycloaddition process: copper(I)-catalyzed regioselective "ligation" of azides and terminal alkynes. *Angew. Chem., Int. Ed. Engl. 41*, 2596-9.

(4) Wang, Q., Chan, T. R., Hilgraf, R., Fokin, V. V., Sharpless, K. B., and Finn, M. G. (2003) Bioconjugation by copper(I)-catalyzed azide-alkyne [3 + 2] cycloaddition. *J. Am. Chem. Soc. 125*, 3192-3.

(5) Chan, T. R., Hilgraf, R., Sharpless, K. B., and Fokin, V. V. (2004) Polytriazoles as copper(I)-stabilizing ligands in catalysis. *Org. Lett. 6*, 2853-2855.

(6) Hong, V., Presolski, S. I., Ma, C., and Finn, M. G. (2009) Analysis and optimization of copper-catalyzed azide-alkyne cycloaddition for bioconjugation. *Angew. Chem., Int. Ed. Engl. 48*, 9879-9883.

(7) Jahnisch, K., Hessel, V., Lowe, H., and Baerns, M. (2004) Chemistry in microstructured reactors. *Angew. Chem., Int. Ed. 43*, 406-446.

(8) Watts, P., and Haswell, S. J. (2005) The application of micro reactors for organic synthesis. *Chem. Soc. Rev. 34*, 235-246.

(9) deMello, A. J. (2006) Control and detection of chemical reactions in microfluidic systems. *Nature 442*, 394-402.

(10) Lin, W. Y., Wang, Y. J., Wang, S. T., and Tseng, H. R. (2009) Integrated microfluidic reactors. *Nano Today 4*, 470-481.

(11) Longstreet, A. R., and McQuade, D. T. (2013) Organic Reaction Systems: Using Microcapsules and Microreactors to Perform Chemical Synthesis. *Acc. Chem. Res. 46*, 327-338.

(12) Wang, Y. J., Lin, W. Y., Liu, K., Lin, R. J., Selke, M., Kolb, H. C., Zhang, N. G., Zhao, X. Z., Phelps, M. E., Shen, C. K. F., Faull, K. F., and Tseng, H. R. (2009) An integrated microfluidic device for large-scale in situ click chemistry screening. *Lab Chip 9*, 2281-2285.

(13) Girard, C., Onen, E., Aufort, M., Beauviere, S., Samson, E., and Herscovici, J. (2006) Reusable polymer-supported catalyst for the [3+2] Huisgen cycloaddition in automation protocols. *Org. Lett. 8*, 1689-92.

(14) Chan, T. R., and Fokin, V. V. (2007) Polymer-supported copper(I) catalysts for the experimentally simplified azide-alkyne cycloaddition. *QSAR Comb. Sci. 26*, 1274-1279.
(15) Reddy, K. R., Rajgopal, K., and Kantam, M. L. (2007) Copper-alginates: a blopolymer supported Cu(II) catalyst for 1,3-dipolar cycloaddition of alkynes with azides and oxidative coupling of 2-naphthols and phenols in water. *Catal. Lett. 114*, 36-40.
(16) Li, P. H., Wang, L., and Zhang, Y. C. (2008) SiO2-NHC-Cu(I): an efficient and reusable catalyst for [3+2] cycloaddition of organic azides and terminal alkynes under solvent-free reaction conditions at room temperature. *Tetrahedron 64*, 10825-10830.
(17) Dervaux, B., and Du Prez, F. E. (2012) Heterogeneous azide-alkyne click chemistry: towards metal-free end products. *Chem. Sci. 3*, 959-966.
(18) Sui, G., Wang, J., Lee, C.-C., Lu, W., Lee, S. P., Leyton, J. V., Wu, A. M., and Tseng, H.-R. (2006) Solution-Phase Surface Modification in Intact Poly(dimethylsiloxane) Microfluidic Channels. *Anal. Chem. 78*, 5543-5551.
(19) Croushore, C. A., Supharoek, S. A., Lee, C. Y., Jakmunee, J., and Sweedler, J. V. (2012) Microfluidic Device for the Selective Chemical Stimulation of Neurons and Characterization of Peptide Release with Mass Spectrometry. *Anal. Chem. 84*, 9446-9452.
(20) Deshpande, K. S., Kuddannaya, S., Staginus, J., Thune, P. C., de Smet, L. C. P. M., ter Horst, J. H., van der Wielen, L. A. M., and Ottens, M. (2012) Biofunctionalization and self-interaction chromatography in PDMS microchannels. *Biochem. Eng. J. 67*, 111-119.
(21) Liu, D., Perdue, R. K., Sun, L., and Crooks, R. M. (2004) Immobilization of DNA onto Poly(dimethylsiloxane) Surfaces and Application to a Microelectrochemical Enzyme-Amplified DNA Hybridization Assay. *Langmuir 20*, 5905-5910.
(22) Hsu, F.-Y., Kuo, K.-L., and Liou, H.-M. (2012) The surface immobilization of galactose ligands on a PDMS substrate for use in primary rat hepatocyte culture. *J. Taiwan Inst. Chem. E. 43*, 165-171.
(23) Lin, R., Freemantle, R. G., Kelly, N. M., Fielitz, T. R., Obare, S. O., and Ofoli, R. Y. (2010) In situ immobilization of palladium nanoparticles in microfluidic reactors and assessment of their catalytic activity. *Nanotechnology 21*.
(24) Lammens, M., Skey, J., Wallyn, S., O'Reilly, R. K., and Du Prez, F. (2010) Polymeric ligands as homogeneous, reusable catalyst systems for copper assisted click chemistry. *Chem. Commun. 46*, 8719-8721.
(25) Biesinger, M. C., Lau, L. W. M., Gerson, A. R., and Smart, R. S. C. (2010) Resolving surface chemical states in XPS analysis of first row transition metals, oxides and hydroxides: Sc, Ti, V, Cu and Zn. *Appl. Surf. Sci. 257*, 887-898.
(26) Wheeler, T. D., Zeng, D., Desai, A. V., Onal, B., Reichert, D. E., and Kenis, P. J. A. (2010) Microfluidic labeling of biomolecules with radiometals for use in nuclear medicine. *Lab Chip 10*, 3387-3396.
(27) Li, H., Zhou, H., Krieger, S., Parry, J. J., Whittenberg, J. J., Desai, A. V., Rogers, B. E., Kenis, P. J. A., and Reichert, D. E. (2014) Triazine-Based Tool Box for Developing Peptidic PET Imaging Probes: Syntheses, Microfluidic Radiolabeling, and Structure–Activity Evaluation. *Bioconjug. Chem. 25*, 761-772.
(28) Hussain, S., Bharadwaj, S. K., Chaudhuri, M. K., and Kalita, H. (2007) Borax as an efficient metal-free catalyst for hetero-Michael reactions in an aqueous medium. *Eur. J. Org. Chem.*, 374-378.

Chapter 3

"Click chip" for conjugation of bifunctional chelators to biomolecules*

3.1 Introduction

Molecular imaging, the noninvasive visualization of biochemical processes on the sub-cellular and cellular levels, is a powerful technique for early detection of diseases and drug discovery.[1] Positron emission tomography (PET) and single-photon emission computed tomography (SPECT) are currently two widely used clinical molecular imaging modalities. PET and SPECT are based on detection of radioisotopes, typically attached to tumor-targeting molecules, which are known as "radiotracers".[2] Currently, for clinical oncology, cardiology, and neurology one of the most widely utilized radiotracers is the PET tracer [^{18}F]fluorodeoxyglucose ([^{18}F]FDG).[3] Yet, [^{18}F]FDG and other ^{18}F-based radiotracers have multiple shortcomings including a short half-life and lengthy and harsh reaction conditions.[4]

Clinically relevant radiometals, including ^{68}Ga, ^{64}Cu, and ^{89}Zr, have half-lives ranging from roughly one hour to a few days. A wide range of available half-lives enables production of radiotracers where the half-life of the radioisotope matches the *in vivo* pharmacokinetics of the radiotracer. For example, antibody-based radiotracers may require days to achieve appropriate signal-to-noise ratios for imaging, and therefore require a radioisotope with a long half-life. Radiometal incorporation into radiotracers is usually accomplished by covalently bonding a bifunctional chelator (BFC) to the targeting biomolecule (BM) and chelating a radiometal to the BFC. This radiometalation event is typically rapid and accomplished under mild conditions.[5]

*This chapter has been adapted with permission from Whittenberg, J. J., Li, H., Zhou, H., Koziol, J., Desai, A. V., Reichert, D. E., and Kenis, P. J. A. (2017) "Click Chip" Conjugation of Bifunctional Chelators to Biomolecules. *Bioconjugate Chem.* 28, 986-994. Copyright 2017 American Chemical Society. This work was performed in collaboration with Dr. David Reichert's group at Washington University in St. Louis.

Covalent attachment of BFCs is usually accomplished via amide, thiourea, and thioether bonds.[6] However, biomolecules tend to have multiple free primary amines and thiols making site-specific BFC attachment a challenge.[7]

The advent of "click chemistry", defined as selective and rapid reactions that require mild conditions[8], has provided a new biorthogonal approach to site-specific BFC attachment to BMs.[9] A wide variety of "click" reactions, including Cu(I)-catalyzed azide-alkyne cycloaddition (CuAAC)[10], strain-induced azide-alkyne cycloaddition[11], and Michael addition of thiols to maleimides[12], have been utilized to link BFCs to BMs. CuAAC is particularly advantageous because the reaction is compatible with many functional groups[13] and the formed triazole heterocycle mimics amide bonds[9] that can also assist with metal chelation[13, 14]. However, key challenges for CuAAC chelator conjugation reactions are: (i) the Cu(I) catalyst is cytotoxic[9], (ii) Cu(I) may chelate with BFCs, and (iii) copper ions combined with sodium ascorbate, typically used to maintain the copper catalyst in the Cu(I) oxidation state, forms reactive oxygen species and byproducts that can damage biomolecules, particularly proteins[15-17]. One convenient method to potentially avoid these complications is to immobilize the Cu(I) catalyst on a solid support.

In this chapter, a microfluidic approach for using immobilized Cu(I) catalyst for CuAAC bifunctional chelator conjugation reactions with biomolecules is described. Only a minute amount (often nanogram levels[18]) of radiotracer is required for imaging *in vivo*, but traditionally radiotracers are synthesized on relatively large-scale automated synthesis modules that require at least 400 μL of solution for easy handling.[19] Microreactors are promising platforms for radiotracer synthesis because they (i) enable handling of small volumes, (ii) provide precise control over reaction conditions, (iii) reduce consumption of expensive precursors, and (iv) minimize radiation shielding size and radiation exposure to personnel.[20, 21] To date though, most

microfluidic radiotracer research has focused on ^{18}F-based probes, in particular the optimization of fluorine incorporation.[22] In prior work the advantages of microfluidics for radiolabeling peptides[23-25] and antibodies[26] with radiometals have been demonstrated, and a recent report indicated the benefits of using microfluidics for radiotracer quality control analysis[20].

The microfluidic approach for conjugating a biomolecule to a bifunctional chelator discussed here utilizes a thinner version of the "click chip" discussed in Chapter 2 that features an immobilized Cu(I)-ligand complex.[27] This unique approach integrates the advantages of microfluidics (*e.g.*, reduced reagent consumption) and "click" chemistry (*e.g.*, site-specific attachment) to yield BM-BFC conjugates. Additionally, an immobilized Cu(I)-ligand complex reduces complications associated with Cu(I) catalyst dissolved in solution. The platform was validated by synthesizing three different BM-BFC conjugates. Two of the conjugates consisted of the azide modified peptide *cyclo*[Arg-Gly-Asp-D-Phe-Lys] (cRGDfK-azide) conjugated to an alkyne derivative of 1,4,7,10-tetraazacyclododecane-1,4,7,10-tetraacetic acid (DOTA) (**Figure 3.1A**) or 1,4,7-triazacyclononane-1,4-diacetic acid (NO2A) (**Figure 3.1B**). The third conjugate was comprised of the nucleoside 5-ethynyl-2'-deoxyuridine (EdU) conjugated to an azide derivative of DOTA (**Figure 3.1C**).

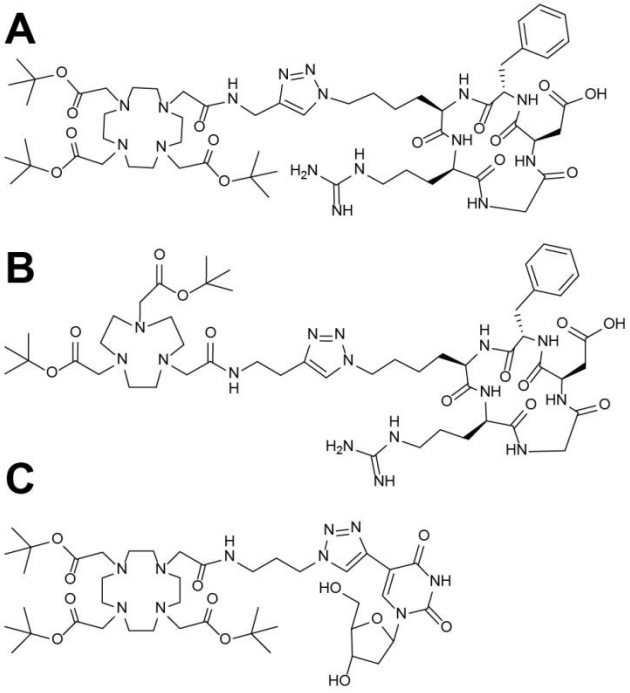

Figure 3.1. Schematic illustration of the BM-BFC conjugates DOTA-cRGDfK (A), NO2A-cRGDfK (B), and DOTA-EdU (C). All conjugates include a fully *tert*-butyl protected BFC without chelated copper ions, but reaction results discussed in detail later indicate BFCs in products displayed partial or complete *tert*-butyl group loss resulting in copper ion chelation.

3.2 Results and discussion

In this chapter I discuss how a thin "click chip" was utilized for conjugating BFCs and BMs as an elegant approach to eventually enable the multi-step synthesis of radiotracers on chip starting from initial reagents. To clarify terminology used in this chapter, both Cu(I) and Cu(II) ions were utilized in experiments. Cu(I) is the active catalyst for CuAAC bioconjugation reactions. In this case, the Cu(I) catalyst was bound to a water soluble Cu(I) ligand to form a Cu(I)-ligand complex. The Cu(I) ligand not only immobilizes Cu(I) catalyst, but maintains copper in the +1 oxidation state critical for CuAAC reactions. However, Cu(II) ions in this work were used to chelate copper to BFCs in an effort to reduce loss of immobilized Cu(I) catalyst discussed in greater detail in subsequent sections.

Multiple LC-MS UV chromatograms (200 nm) will be displayed throughout this chapter. The same LC-MS elution method (more details in materials and methods section) was used for all samples. Compounds of interest eluted between roughly 12 and 40 min so only this window is displayed. There were peaks prior to 12 min elution time, but these were from dimethyl sulfoxide (DMSO) and salts and were present because samples were not purified prior to injection into the LC-MS system. An example chromatogram of a blank injection with no sample (**Figure 3.2A**) and a sample injection of NO2A-alkyne (**Figure 3.2B**) is provided to show peak locations of salts and DMSO present in most samples.

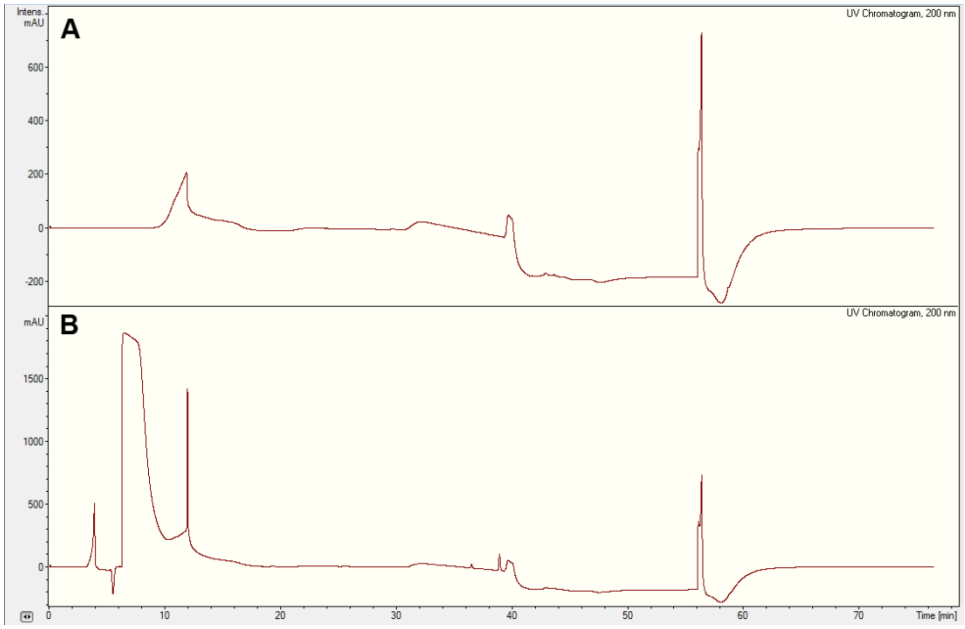

Figure 3.2. LC-MS UV chromatograms of a blank without any sample (A) and a BFC (NO2A-alkyne) sample (B). The same LC-MS method was used for all samples, and all samples had similar peaks from 0-12 min. The large peaks from ~6-12 min are due to a small amount of DMSO in samples.

Design and fabrication of thin "click chips"

The "click chip" for dye conjugation discussed in Chapter 2 was comprised of reservoirs containing posts to reduce reagent diffusion times to catalyst sites located on the inner chip walls.[27] Chip features were patterned in polydimethylsiloxane (PDMS) using traditional soft

lithography techniques and subsequently bonded to glass. PDMS and glass were used for the "click chip" fabrication because of the availability of well-established fabrication procedures and facile methods to immobilize compounds onto inner channel surfaces. The same design discussed in Chapter 2, five reservoirs with posts, was used for the work described in this chapter to provide ample solution volume for analysis. However, most non-therapeutic radiotracers are given at nanogram levels.[18] Here, BFC-BM conjugates were synthesized at roughly microgram levels (~100s μM concentrations) for accurate analysis utilizing a LC-MS set-up with a UV detector. In addition to reducing reagent concentrations, the number of reservoirs can easily be adjusted to tune reactor volume without changing the immobilization process to produce the desired nanogram levels of radiotracer with little loss of expensive reagents.

However, to use the "click chip" approach with immobilized Cu(I) catalyst for the synthesis of radiotracers I needed to address the challenge of solvent loss resulting from long incubation times in traditional, thick (~3-5 mm) PDMS chips. The previous "click chip" discussed in Chapter 2 was well suited for short reactions (~30-50 min), but "click" conjugation of BFCs to BMs at or near room temperature require longer incubation times (~12-18 h).[28, 29] The approach taken to alleviate this solvent loss was to create a thinner chip (**Figure 3.3A**) comprised of three layers, glass, PDMS, and cyclic olefin copolymer (COC) (**Figure 3.3B**). PDMS thickness was reduced from approximately 4 mm to 400 μm to minimize solvent loss into the bulk PDMS and through the sides of the microreactor. A 100 μm thick layer of water impermeable COC was bonded onto the PDMS to minimize water loss through the top of the reactor. Thick PDMS was only present at inlets and outlets to support tubing used to inject fluids into the thin "click chip".

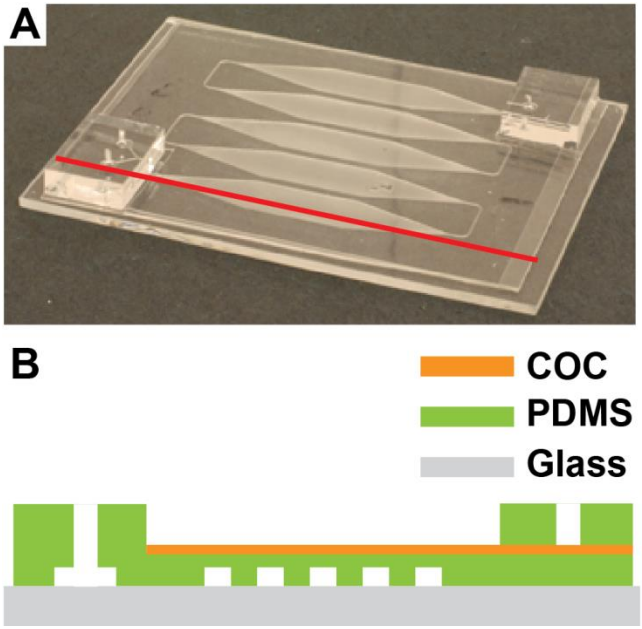

Figure 3.3. Photograph (A) and side-view schematic (B) of a thin "click chip" with five reservoirs filled with posts, the red line in (A) is the location of the side-view in (B). PDMS thickness was reduced and a gas impermeable COC layer was added to minimize solvent loss. A thicker layer of PDMS was used at inlets and outlets to support tubing.

Control experiments were performed to confirm solvent loss in thin COC/PDMS/glass chips was lower compared to traditional thick PDMS/glass chips. Both thin and thick microreactors were filled with water and incubated in humidity chambers at room temperature, 37 °C, or 47 °C for 12 h. Very little solvent loss occurred in either reactor when incubated at room temperature. However, thin chips lost less solvent (6.58% ± 1.12%) compared to thick chips (19.7% ± 3.55%) when incubated at 47 °C for 12 h (**Figure 3.4**). These results confirmed that thin chips reduced solvent loss at elevated temperatures.

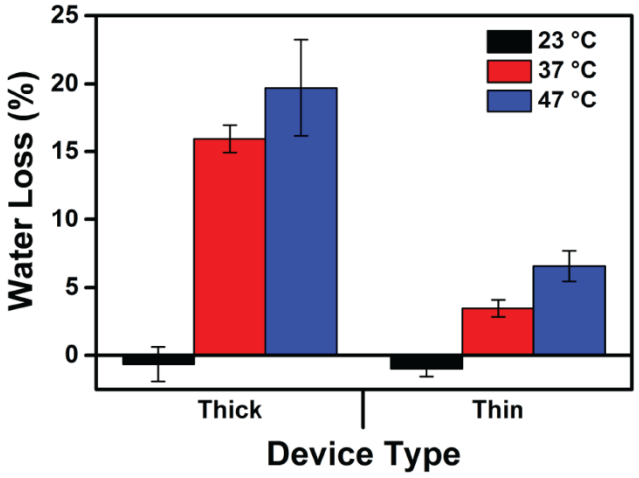

Figure 3.4. Water loss data for thick PDMS/glass and thin COC/PDMS/glass chips after incubating chips filled with water in a humidity chamber for 12 h at the specified temperature.

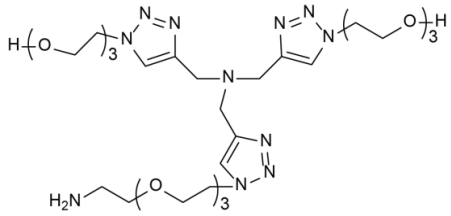

Figure 3.5. Schematic illustration of the water soluble analog of the commonly used Cu(I) chelator tris-(benzyltriazolylmethyl)amine (TBTA) used here to immobilize Cu(I) catalyst.

The final step for fabrication of thin "click chips" was to immobilize a Cu(I) ligand onto the inner microreactor surfaces to enable chelation of Cu(I) catalyst that facilitates the BFC and BM "click" conjugation reaction. The Cu(I) ligand utilized here is the same water soluble analog of tris-(benzyltriazolylmethyl)amine (TBTA) discussed in Chapter 2 (**Figure 3.5**), and the immobilization process was similar to the method described in Chapter 2.[27] Briefly, the channel surfaces were activated with an acidic hydrogen peroxide solution followed by injection of a neat 'silane' solution. The water soluble Cu(I) ligand was connected to the silane functionalized surface using an aza-Michael reaction catalyzed by a borax catalyst. To this end a ligand solution consisting of the Cu(I) ligand and borax was then injected into the chip. Finally, a Cu(I) solution comprised of an aqueous mixture of $CuSO_4$ and sodium ascorbate was injected into the

microreactor to form an immobilized Cu(I)-ligand complex. Excess non-chelated Cu(I) and other ions were removed via rinsing. The amount of chelated Cu(I) catalyst present in microreactors (1136 ± 272 nmol) was determined as described in Chapter 2, using ^{64}Cu.[27] The fabricated thin "click chip" will hereafter be referred to as simply "click chip" for the remainder of Chapter 3.

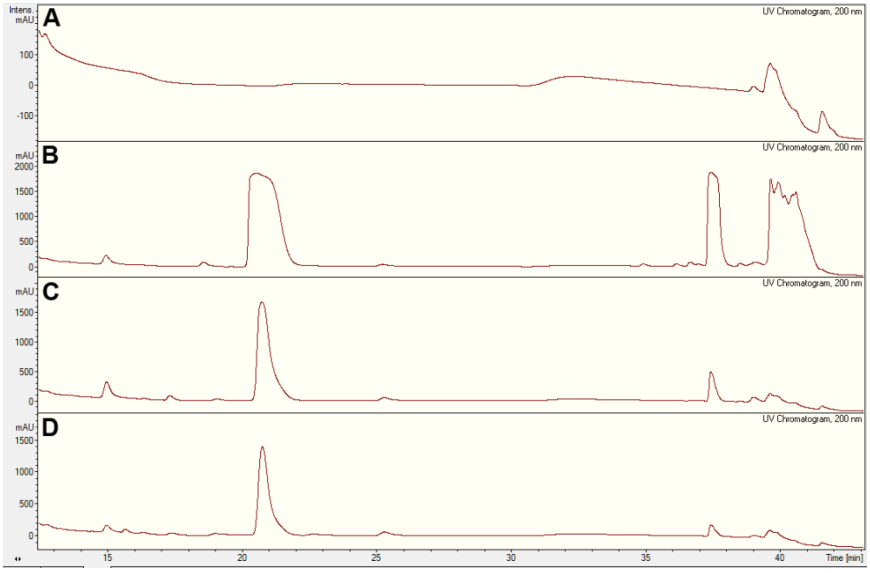

Figure 3.6. LC-MS UV chromatograms of solutions incubated in a "click chip" prior to any surface functionalization (A), after silane incubation (B), after attachment of the water soluble Cu(I) ligand (C), and after Cu(I) chelation (D).

Initial conjugation reactions, described in more detail in later sections, indicated some contaminants were present in reaction solutions. The contaminants were likely non-immobilized reagents from the surface functionalization process. To confirm this two "click chips" were functionalized, but the immobilization process was halted at various steps and a buffer solution was incubated in the "click chips" and the solutions were collected and analyzed by LC-MS. Solutions were collected after four different steps: (1) bonding PDMS device to glass prior to any surface treatment steps, (2) silane incubation, (3) water soluble Cu(I) ligand immobilization, and (4) Cu(I) incubation. Based on UV chromatograms the primary contaminant was silane

(**Figure 3.6**). This is supported by the observation that silane diffused into the PDMS during the functionalization process. The silane then likely leached back into reaction solutions.

To determine which factors significantly impacted silane contamination a fractional factorial design of experiments (DOE) was set-up to tune the parameters of the silane attachment steps. The following four factors were varied to reduce the amount of silane diffusing into the PDMS, (1) silane concentration, (2) silane incubation time, (3) oven incubation time, and (4) duration of methanol rinse following the oven incubation. A fractional factorial design with two levels for each factor was selected to quickly determine significant factors. The factors were coded as A, B, C, and D and two levels were set for each factor to test the extreme conditions (+ for the upper extreme, – for the lower extreme) (**Table 3.1**). The final fractional factorial DOE consisted of eight trials (**Table 3.2**).

Table 3.1. Lists all factors and levels used for the fractional factorial DOE to identify significant factors that contribute to silane contamination of product solutions.

Factor and Level	Condition
A-	10% silane
A+	97% silane
B-	5 min silane incubation
B+	1 h 55 min silane incubation
C-	1 h oven incubation
C+	24 h oven incubation
D-	5 min methanol rinse
D+	1 h 55 min methanol rinse

Table 3.2. Lists the eight different trials conducted to determine which factors significantly affected silane contamination. The plus and minus signs correspond to **Table 3.1** and indicate whether the lower or upper extreme was used for a factor.

	Factors			
Trial	**A**	**B**	**C**	**D**
1	-	-	-	-
2	+	-	-	+
3	-	+	-	+
4	+	+	-	-
5	-	-	+	+
6	+	-	+	-
7	-	+	+	-
8	+	+	+	+

The eight trials listed in **Table 3.2** were performed to determine which factors significantly affected silane contamination of product solutions. Each trial represents one microfluidic device where the same "click chip" functionalization process was utilized except the procedure stopped after rinsing the devices with methanol following silane and oven incubation steps (see materials and methods section for details). After the last step an aqueous solution with 8 v/v% DMSO was incubated in the chip for 2 hours and the solution was collected for analysis by LC-MS. The silane concentrations were calculated based on a standard curve of known silane concentrations and the results were entered into Minitab to determine which factors were significant. Based on a normal plot of the factors and three two-factor interactions (AB, AC, and AD) none of the effects were considered significant (**Figure 3.7**).

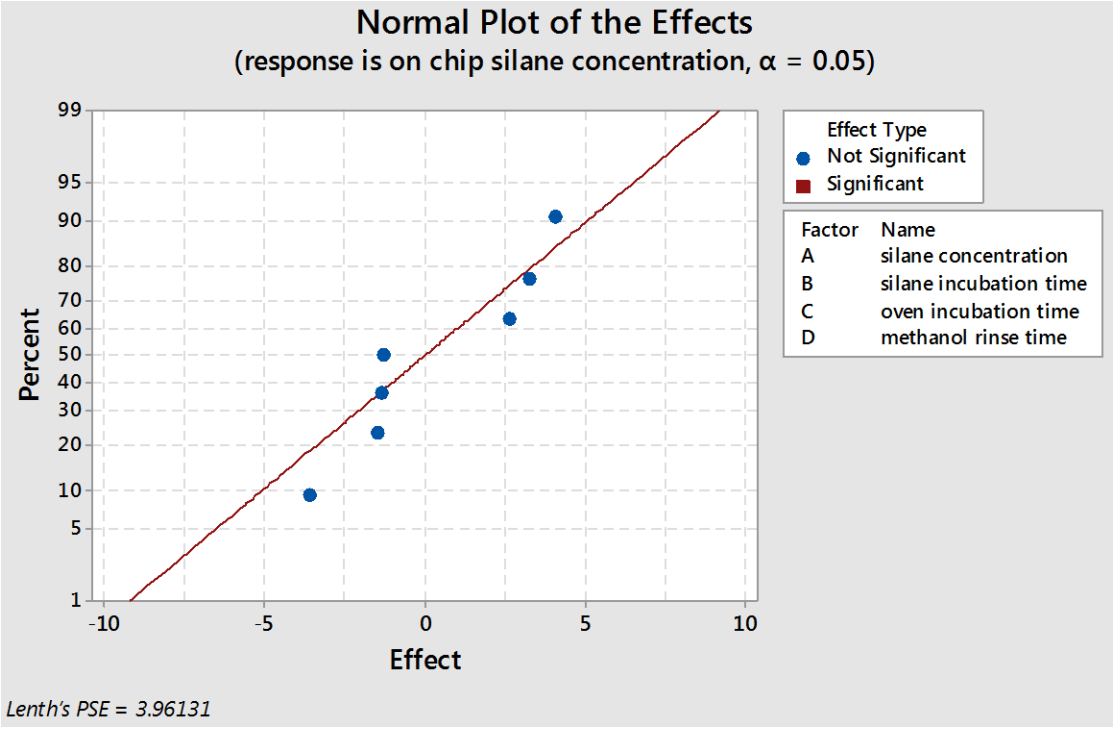

Figure 3.7. Normal plot of factors and three two-factor interactions (AB, AC, and AD) indicated no effects were significant. Plot was created using Minitab.

Despite not statistically finding any of the factors significant the LC-MS results indicated trials 4 and 5 had the highest and lowest silane concentrations (12.1 mM and -0.26 mM respectively) of the eight trials. The negative value occurred because the actual silane concentration was below the lowest standard (1 mM). The results of trials 4 and 5 made sense considering these treatment combinations are the extremes. For example, trial 4 utilized the highest silane concentration (97%) and longest silane incubation time (1 h 55 min), but the shortest oven incubation (1 h) and methanol rinse (1 h 55 min) times. Trial 5 was the exact opposite of trial 4, representing the factors that would likely lead to the lowest silane concentrations in incubation solutions, which was supported by values quantified using LC-MS (UV chromatograms). Trials 4 and 5 were repeated three more times and the silane concentrations of incubation solutions were determined from LC-MS UV chromatograms (**Figure 3.8**). The lack of any significant factors from the fractional factorial design is likely from a lack of replication which is one inherent negative of unreplicated fractional factorial DOEs. However, I was able to demonstrate that parameters can be tuned to reduce silane contamination of solutions incubated in "click chips". Future work can optimize this process further to optimally minimize silane contamination while maximizing bound Cu(I) catalyst.

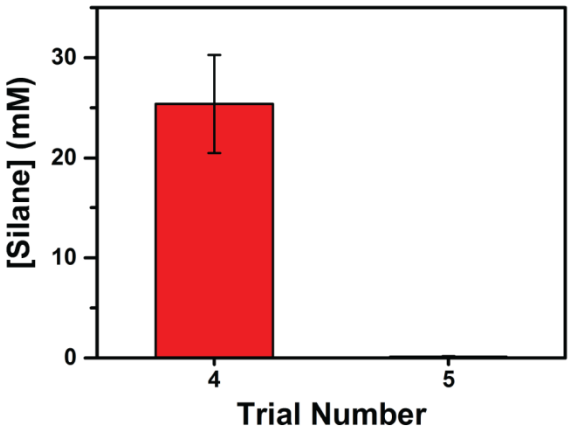

Figure 3.8. Silane concentration of aqueous solutions incubated in microfluidic devices functionalized using treatment combinations of trial 4 or 5 as outlined in **Table 3.2**. The values represent the average ± one standard deviation (n = 3).

BFC and BM conjugation reactions

General method for conjugation reaction. Prior to the reaction, a reagent mixture was created by mixing stock solutions of the appropriate BFC and BM together in a phosphate buffer. Then, the "click chip" with immobilized Cu(I) was rinsed and a portion of the BFC and BM solution was injected into the microreactor. The microreactor was placed in a pre-heated humidity chamber for the specified incubation time, and reaction samples were collected for LC-MS analysis. Following sample collection the chip was rinsed thoroughly with methanol and water. Then, more BFC and BM solution was injected into the microreactor and incubated in a humidity chamber again. The process of adding the reagent mixture, incubating, and collecting a sample was repeated until three samples were collected from each "click chip". The Cu(I) solution ($CuSO_4$ and sodium ascorbate) was only injected prior to the first reaction. All conjugation reactions were performed on two separate "click chips", so a total of six samples were collected for each set of conjugation reaction parameters.

LC-MS was utilized to determine the yields of the bioconjugation reactions. No further work-up of reaction samples was performed prior to LC-MS. All yields discussed here were determined from crude reaction samples. Samples were collected from the chip and directly injected into the LC-MS system along with multiple dilutions of the initial reagents to establish a standard curve. Yields were calculated by comparing peak areas of the initial reagents before and after the reaction.

Unexpected tert-butyl protecting group loss. The initial "click chip" conjugation reaction tested was between propargyl-DOTA-tris(*tert*-butyl) ester and cRGDfK-azide. The reagent mixture was incubated for 12 h at 47 °C. DOTA-cRGD product formed but two unexpected results occurred; (i) DOTA-alkyne lost *tert*-butyl (tBu) protecting groups and (ii) DOTA-alkyne

chelated copper by removing Cu(I) from the Cu(I)- ligand complex. These two observations were true for both unreacted DOTA-alkyne and DOTA in the DOTA-cRGD product. Divalent cations have been utilized before to bind near esters in non-BFC compounds to catalyze ester hydrolysis, and the rate of hydrolysis was likely related to binding affinities for the divalent cation.[30] Previous reports regarding macrocycle BFCs indicated tBu protected DOTA-alkyne species will chelate Cu, but reaction conditions varied widely (*e.g.*, temperature, catalyst concentrations) and no previous work used an immobilized Cu(I) catalyst. Previous work demonstrated that DOTA-alkyne without tBu protecting groups removes and chelates copper from a non-immobilized Cu(I)-ligand complex.[31] Here, I describe how even when the Cu(I)-ligand complex is immobilized and the BFC reagent (DOTA-alkyne) contains tBu protecting groups, tBu protected DOTA-alkyne still (i) loses tBu protecting groups and (ii) removes Cu(I) catalyst from the Cu(I)-ligand complex via chelation.

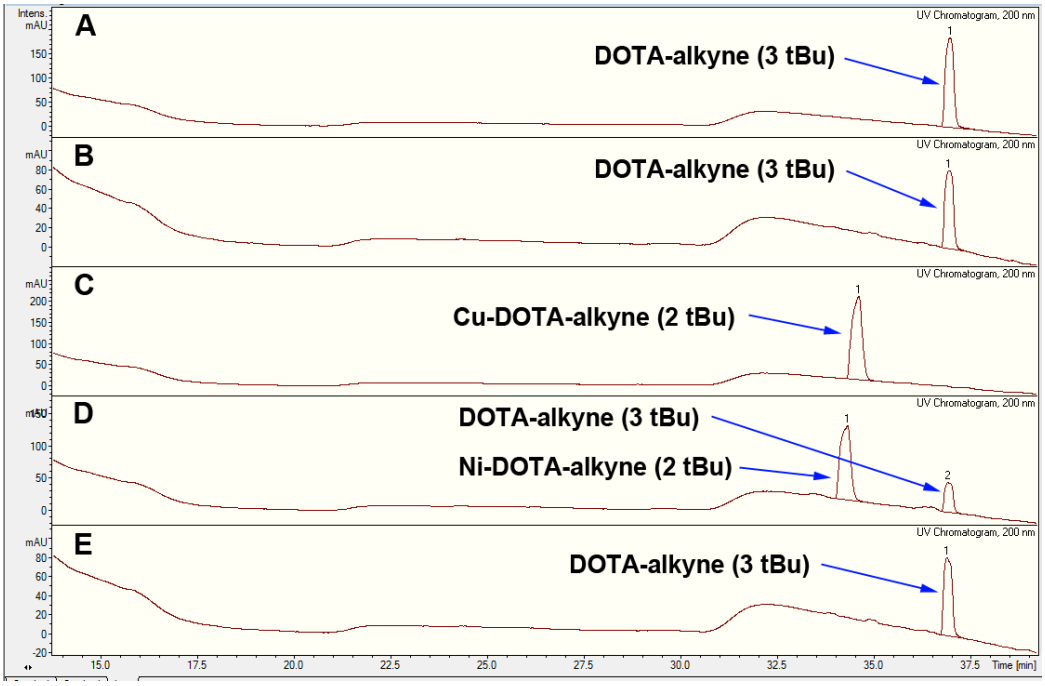

Figure 3.9. LC-MS UV chromatograms of tBu protected DOTA-alkyne stock solution (A), tBu DOTA-alkyne incubated without any metal added (B), tBu DOTA-alkyne incubated with Cu(II) (C), tBu DOTA-alkyne incubated with Ni(II) (D), and tBu DOTA-alkyne incubated with Fe(II) (E).

To further investigate tBu protecting group loss and metal chelation, tBu protected BFCs were incubated with metal ions. A recent review mentioned little systematic data is available on how other protected chelators, besides DOTA-alkyne derivatives, behave during CuAAC.[32] Therefore, three different protected chelators, including propargyl-DOTA-tris(tBu) ester, were incubated with $CuSO_4$ at 47 °C for 4 h to determine the effect of copper ions on different tBu protected chelators. Protected DOTA-alkyne displayed complete conversion to Cu-DOTA-alkyne with 2 t-butyl groups (**Figure 3.9**), similar to the initial "click" reaction tested. However, when an azido-DOTA-tris(tBu) ester compound was incubated under the same conditions, a mixture of Cu-DOTA-azide compounds with 2 and 3 tBu protecting groups formed (**Figure 3.10**). When incubating copper(II) with a different chelator, propargyl-NO2A-bis(tBu) ester, the incubation also yielded a mixture of Cu-NO2A compounds with either 0 or 1 tBu groups (**Figure 3.11**).

The Cu-DOTA-azide compounds are particularly interesting because of the three different BFCs incubated with Cu(II), Cu-DOTA-azide with 3 tBu protecting groups was the only example of a Cu-BFC complex that formed without loss of any tBu groups. This may be because azides are able to assist with formation of Cu complexes.[33] However, there is little previous structural data regarding Cu-DOTA-azide species and further experiments are required to conclusively demonstrate the azide group interacts with the chelated copper.

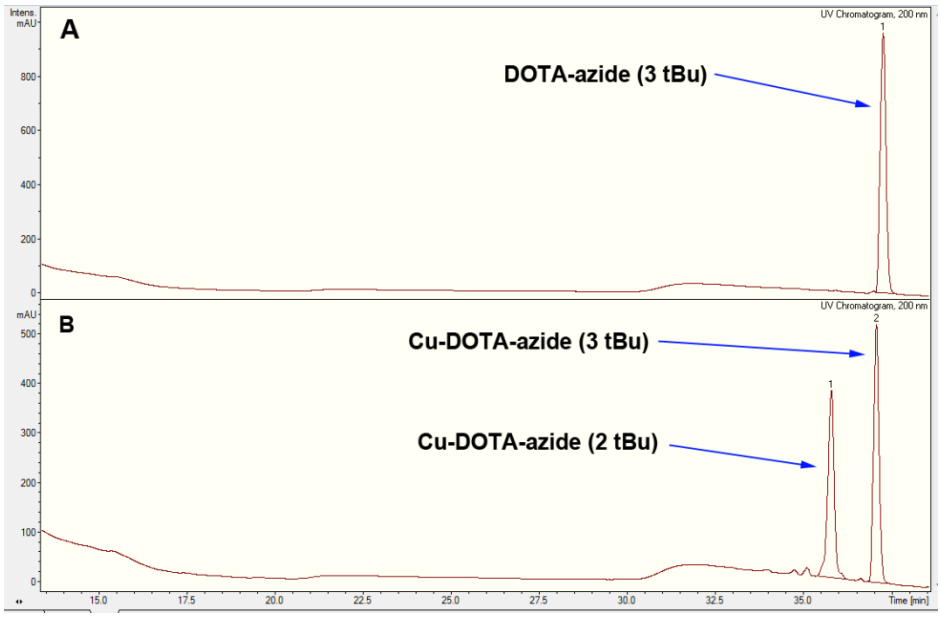

Figure 3.10. LC-MS UV chromatograms of tBu protected DOTA-azide stock solution (A) and Cu-DOTA-azide after incubating tBu DOTA-azide with Cu(II) for 4 h at 47 °C (B).

Additionally, Ni(II) and Fe(II) were incubated with protected DOTA-alkyne and NO2A-alkyne to determine the effects of other metals on tBu protected chelators. Ni(II) and Fe(II) were selected because both are potential contaminants of ^{64}Cu solutions. While Ni(II) caused partial or complete loss of t-butyl groups similar to Cu(II), incubating DOTA- or NO2A-alkyne with Fe(II) caused no substantial loss of t-butyl groups, as seen in **Figure 3.9** and **Figure 3.11**, respectively. Therefore, the results indicate that other *tert*-butyl protected bifunctional chelators, NO2A-alkyne and DOTA-azide, are also susceptible to (i) tBu protecting group loss and (ii) metal ion chelation. Furthermore, the results indicate the number of tBu groups lost depends on the chelator and the metal ion present.

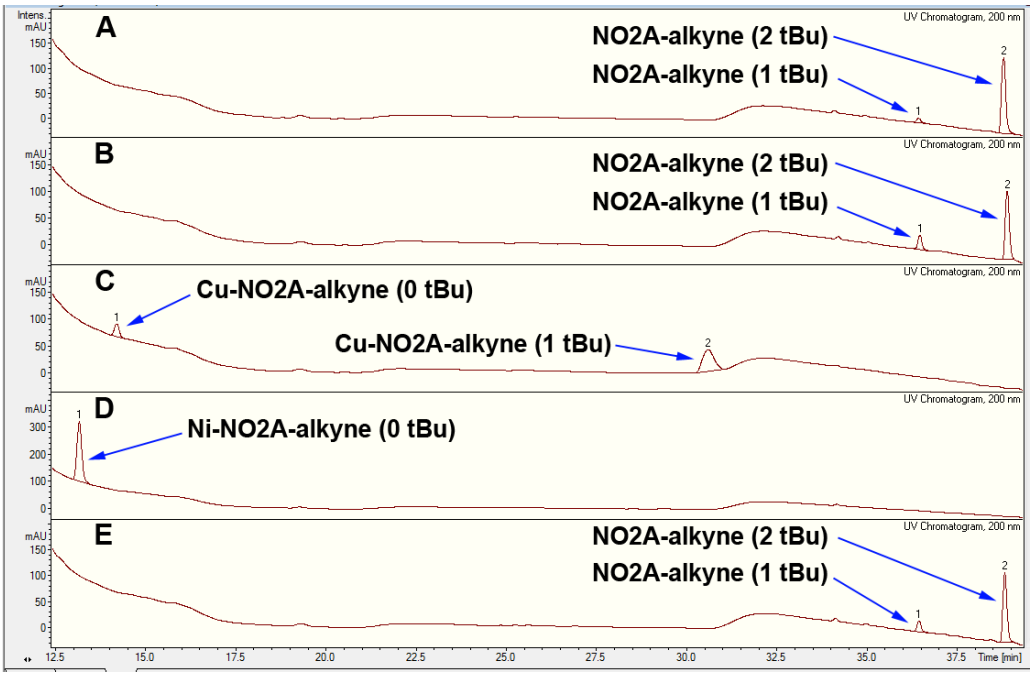

Figure 3.11. LC-MS UV chromatograms of tBu protected NO2A-alkyne stock solution (A), tBu NO2A-alkyne incubated without any metal added (B), tBu NO2A-alkyne incubated with Cu(II) (C), tBu NO2A-alkyne incubated with Ni(II) (D), and tBu NO2A-alkyne incubated with Fe(II) (E).

"Click chip" characterization and testing. In light of the tBu loss and chelation issues of tBu protected BFCs in the presence of metal ions, even when the metal ion was immobilized, the BM and BFC conjugation reaction process was slightly modified. Specifically, BFCs were reacted with Cu(II) ions prior to "click" reactions in an effort to reduce loss of Cu(I) catalyst from the immobilized Cu(I)-ligand complex. Therefore, all reagent mixtures consisted of the appropriate Cu-BFC and BM mixed in a phosphate buffer.

I systematically tested the conjugation reaction of Cu-DOTA-alkyne and cRGDfK-azide at different temperatures (**Figure 3.12A**) and incubation times (**Figure 3.12B**) to determine their effects on yields. **Figure 3.12** displays the yields for each individual reaction for "click chip" 1 (red columns) and "click chip" 2 (blue columns), and also the cumulative mean yield of all six reactions ± one standard deviation (yellow columns) for each condition. Some Cu-DOTA-cRGDfK yields slightly exceeded 100% due to difficulty in subtracting background levels of the

cRGDfK-azide reagent in LC-MS chromatograms. As expected, yields were higher when operating at 47 °C compared to 19 °C (**Figure 3.12A**), especially for the first incubation (left most red and blue columns).

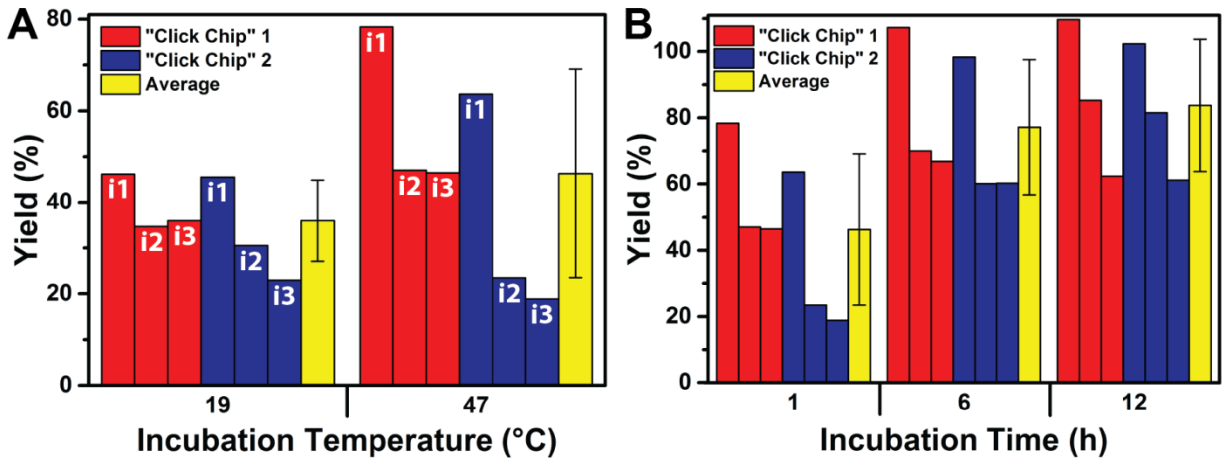

Figure 3.12. Yields for successive incubations (i1, i2, i3) of Cu-DOTA-alkyne and cRGDfK-azide performed with "click chips" 1 (red bars) and 2 (blue bars) incubated at different temperatures (A) or times (B). Reactions at different temperatures (A) were incubated for 1 h. Reactions at different times (B) were incubated at 47 °C. Yellow columns represent the cumulative mean yield of all six reactions ± one standard deviation for each condition.

Incubation time also affected yields with a general increase in yields with increasing incubation time. Yields for "click chip" 2 were considerably lower after 1 h incubations at 47 °C. As discussed in Chapter 2, the total amount of immobilized Cu(I) catalyst was 1136 ± 272 nmol.[27] Therefore, the difference in yields is likely due to less Cu(I) on "click chip" 2, which is further corroborated by Cu(I) loss experiments (**Figure 3.14A**) discussed in detail later. However, yields for both chips after 6 h and 12 h incubations were nearly identical; indicating the chip-to-chip variation in Cu(I) catalyst loading had negligible impact on yields for longer incubations.

Control reactions were performed by incubating a solution of Cu-DOTA-alkyne and cRGDfK-azide in a chip without immobilized silane or water soluble Cu(I) ligand. The Cu(I) solution ($CuSO_4$ and sodium ascorbate) was still injected into the microreactors identically to "click

chips" but no immobilized water soluble Cu(I) ligand was present. Only a small amount of product (8% ± 4%) formed (**Figure 3.13**), demonstrating the importance of the immobilized TBTA analog to first capture the Cu(I) catalyst and then support the Cu(I) oxidation state critical for CuAAC reactions.

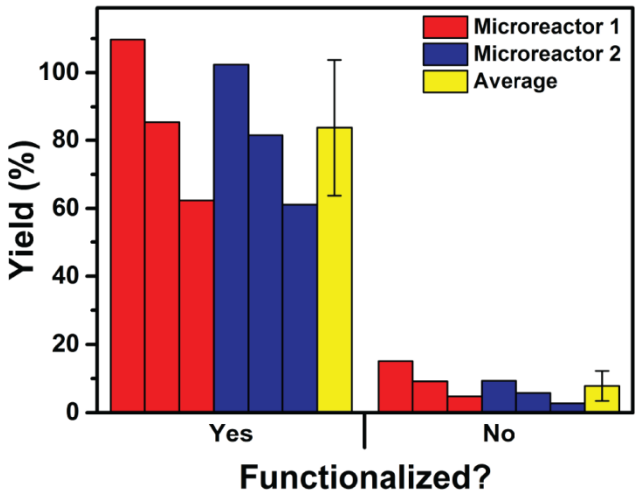

Figure 3.13. Yields for the conjugation of Cu-DOTA-alkyne and cRGDfK-azide using thin "click chips" with immobilized silane and Cu(I) ligand (functionalized) or microreactors without immobilized silane and Cu(I) ligand (not functionalized). Cu(I) catalyst was injected into both chips prior to the first reaction. Reactions were incubated for 12 h at 47 °C.

The "click chips" successfully facilitated the conjugation of BFC (Cu-DOTA-alkyne) and BM (cRGDfK-azide). Complete conversion of reagents was observed after 6 h incubations at 47 °C for the first incubations on both microreactors. These are promising results considering many traditional BM and BFC CuAAC conjugation reactions require either harsh reaction conditions, including high temperatures and microwave irradiation[28, 31, 34], or long reaction times (~18 h) at room temperature[7]. Additionally, the same two "click chips" were utilized for all reactions and similar yields from both microreactors after 6 h and 12 h incubations indicate "click chip" fabrication is reproducible.

Figure 3.12 clearly indicates decreasing yields for successive reactions. The likely cause of the decline in yield was active catalyst loss during incubations and rinse steps. To determine the

extent of Cu(I) catalyst loss, a solution without BFC or BM was incubated in the "click chips" identical to conjugation reactions. Incubation samples were collected similarly to conjugation reactions, but methanol and water used to rinse the microreactors after each reaction were also collected. The amount of copper (**Figure 3.14A**) in collected solutions were quantified by inductively coupled plasma optical emission spectrometry (ICP-OES). Because ICP-OES requires a few milliliters of sample, incubations and rinse solutions were combined in separate vials for each chip. Therefore, the results in **Figure 3.14A** are cumulative amounts of copper for each chip after three incubations.

Despite losing Cu(I) catalyst, most Cu(I) was lost during the rinsing step and both catalytic activity and yields were easily recovered by injecting more Cu(I) ions into the microreactor. Copper concentrations in samples was low (~20 ppm), which is much lower than typical CuAAC "click" conjugation reactions of BFCs and BMs which can easily have copper concentrations in the range of 100's to 1000's of ppm if not higher. The reduced copper concentration in samples mitigates or obviates purification requirements typically required for CuAAC reactions. Additionally, **Figure 3.14B** indicates yields are nearly identical after multiple uses, where one use is defined as injection of Cu(I) ions followed by three simultaneous incubations without the addition of fresh Cu(I) catalyst in between reactions. The same two "click chips" were used for conjugating BFCs and BMs under a variety of conditions but the yields after seven uses (21 reactions) were nearly the same as the first use (initial three reactions). **Figure 3.14B** demonstrates the robustness of the "click chips" after multiple uses and indicates the microreactors can be reused for at least 20 reactions.

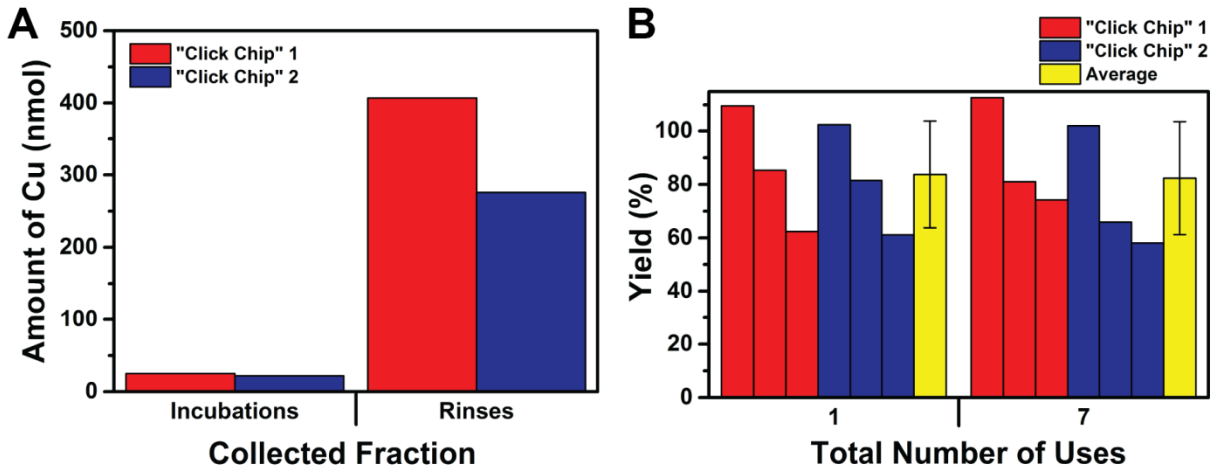

Figure 3.14. Amount of copper in incubation samples and rinse solutions used to wash the microreactors between incubations. The values are the total amount of copper from 3 sequential incubations in each "click chip" (A). Yields of the "click chip" facilitated conjugation of Cu-DOTA-alkyne and cRGDfK-azide after one use and seven uses where each "use" consists of injecting Cu(I) ions followed by three sequential reactions (B).

Versatility for other substrates. After establishing ideal "click chip" operation conditions with the conjugation reaction between Cu-DOTA-alkyne and cRGDfK-azide additional conjugation reactions were tested to demonstrate synthesis of different BM-BFC conjugates on chip. Peptides are attractive biomolecules for radiotracers because of their rapid clearance and facile synthesis[35], but DNA or RNA based imaging probes are receiving increased attention because of their low immunogenicity, high affinity, and stable structures among other traits.[36] Therefore, conjugation reactions between Cu-DOTA-azide and EdU, a commercially available nucleoside, were tested to demonstrate a conjugation reaction with a non-peptide BM. There are also a wide variety of BFCs besides DOTA utilized in radiotracers. The choice of chelator depends on the radiometal utilized[37], and different chelators can greatly affect biodistribution of radiotracers.[38] NO2A derivatives are another widely used BFC, and were utilized for the conjugation reaction of Cu-NO2A-alkyne and cRGDfK-azide to test conjugation of different BFCs to BMs using "click chips".

The “click chip” successfully synthesized both NO2A-cRGD and DOTA-EdU conjugates. When Cu-DOTA-azide and EdU were incubated at 47 °C for 12 h in “click chips”, the CuAAC conjugation reaction proceeded with similar yields to the Cu-DOTA-alkyne and cRGDfK-azide conjugation reaction with near complete conversion and ~80% average yield (**Figure 3.15**). When the Cu-NO2A-alkyne and cRGDfK-azide reaction was performed on chip using the same conditions the yields (~45% average yield) were lower than the other two conjugation reactions. This indicates longer incubations are likely required for some conjugation reactions (**Figure 3.15**). Ultimately, the two additional conjugation reactions demonstrate the versatility of the “click chips” to facilitate conjugation reactions between multiple BMs and BFCs. This versatility is crucial when synthesizing custom radiotracers to meet the needs of individual patients.

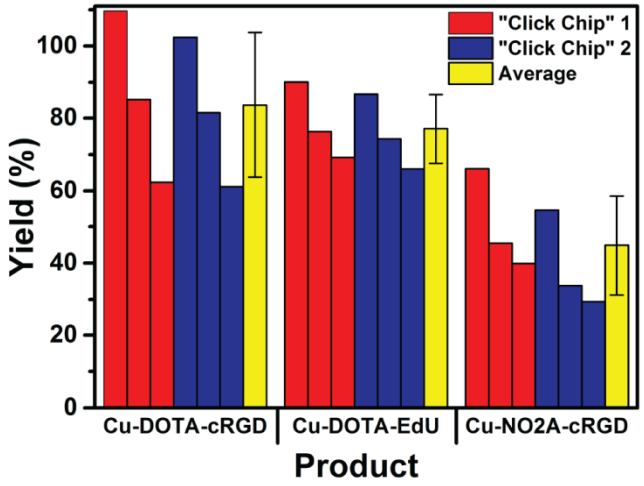

Figure 3.15. Yields for three different CuAAC reactions on chip to produce Cu-BFC-BM conjugates. Reactions were incubated at 47 °C for 12 h.

3.3 Materials and methods

All solvents and chemical reagents were purchased from Thermo Fisher Scientific, Sigma-Aldrich, or Avantor and were used as received unless otherwise specified. Water was purified in-house using a Barnstead E-Pure filtration system. Sylgard 184 PDMS from Dow Corning, a

G3P-8 Spin Coater from Specialty Coating Systems, silicon wafers from University Wafer, 4 mil (101.6 μm) thick COC from TOPAS Advanced Polymers, glass microscope slides from Thermo Fisher Scientific, and a PDC-001 Harrick Scientific Plasma Cleaner were utilized for chip fabrication. DOTA-alkyne was purchased from CheMatech, and NO2A-alkyne and DOTA-azide were from Macrocyclics. The peptide cRGDfK-azide was synthesized as described previously.[31] 30 gauge PTFE tubing from Cole-Parmer, glass syringes from Hamilton Company or plastic syringes from Henke-Sass Wolf and Becton, Dickinson and Company, and Micro-Liter and Milliliter syringe pump modules from Harvard Apparatus were used for injecting fluids into chips. Cu(I) catalyst loss was determined by a PerkinElmer Optima 2000 DV ICP-OES. LC-MS was performed on an Agilent LC-MS (HPLC: 1100, MS: Trap XCT Plus) using a Luna C18(2) column (5 μm, 100 Å, 150 x 4.60 mm) from Phenomenex. The same LC-MS method was used for all samples. The flow rate was 400 μL min^{-1} with the mobile phase of solvent A (0.1% formic acid in water) and solvent B (0.1% formic acid in acetonitrile). The linear gradient used was 0% B (0-2 min), 0%→10% B (2-10 min), 10% B (10-15 min), 10%→15% B (15-25 min), 15%→45% B (25-35 min), 45%→100% B (35-36 min), 100% B (36-51 min), 100%→0% B (51-51.5 min), 0% B (51.5-76.5 min). MS (ESI) used a nebulizer pressure of 35.00 psi, a dry gas flow rate of 8.00 L min^{-1}, a dry temperature of 350 °C, and a capillary voltage of 4.5 kV.

Thin "click chip" fabrication

PDMS used for the interconnects was combined in a 10:1 ratio (base : curing agent), mixed, and degassed for ~20 min. The PDMS was poured onto a silicon wafer inside a petri dish, and cured for 2 h in a 65 °C oven, then allowed to cool to room temperature and stored for later use.

The silicon masters used for PDMS molds were etched as described previously.[27] More 10:1 PDMS was prepared for the microreactor identically to the interconnect process. The etched

silicon wafer was centered on a spin-coater, and the degassed PDMS was carefully poured on top of the wafer. The PDMS was spun at 200 rpm for 60 s, cured in an oven for 1 h at 65 °C, and then allowed to cool to room temperature. A sheet of COC was cut to ~55 x 55 mm. The chip design was printed onto a transparency sheet and taped to the COC. Using the transparency sheet as a guide the COC above the inlets and outlets was cut out. The cured PDMS prepared earlier for interconnects was cut to size using a scalpel.

The protective coating from the COC was removed and the COC, PDMS interconnects, and PDMS chip on the silicon wafer were all placed in a plasma cleaner. All components were treated with an oxygen plasma for 1 min. Immediately after removal the PDMS interconnects were attached followed by the COC. Pressure was applied to the COC using a block of PDMS to remove any air pockets. The bonded components were placed in a 65 °C oven for 30 min then allowed to cool to room temperature. A scalpel was used to cut the PDMS along the edge of the COC and the PDMS layer was carefully removed from the silicon master. Tape was applied to the exposed PDMS surface and the chip was trimmed to size using scissors. The tape was peeled off near the interconnect ports and through-holes were punched at each inlet and outlet with a piece of 19 gauge hypodermic tubing with the punch side beveled to prevent cracking the PDMS.

A 50 x 45 x 1 mm glass slide was scrubbed clean with an Alconox solution, rinsed with water, and dried with N_2. The tape from the PDMS imprint was removed and both the PDMS and glass were treated with an oxygen plasma for 1 min. The PDMS and glass were bonded together and incubated overnight in a 65 °C oven.

Quantifying solvent loss in thin and thick chips

Thick PDMS/glass chips were fabricated as described previously.[27] Methanol was injected into thin (COC/PDMS/glass) and thick (PDMS/glass) chips to eliminate bubbles, and then water was

injected for 10 min to replace methanol as the solvent. Double-sided Scotch tape was applied onto small pieces of glass (~10 x 10 x 1 mm), which were then placed on top of the interface ports of each chip. Microfluidic chips were placed in preheated humidity chambers consisting of 150 mm diameter glass petri dishes with lids and two aluminum weigh boats filled with water. After placing the chips in the glass dishes the lid was sealed with Parafilm. Chips were incubated at the appropriate temperature (23 °C, 37 °C, or 47 °C) for 12 h. Water loss was determined by comparing chip mass before and after heating. Chips were allowed to cool for at least 10 min prior to determining the mass after incubation.

Ligand immobilization process

A 1 mL glass syringe and a bottle of 3-(trimethoxysilyl)propyl acrylate (TMSPA), were placed in a glove bag to reduce water contamination that may induce silane crosslinking. The glove bag was purged with house N_2 three times then filled with N_2 a fourth time. The syringe was loaded with TMSPA inside the N_2 filled glove bag. The "click chip" was rinsed with methanol at 30 μL min^{-1}, and pressure was applied with a block of PDMS to remove any air pockets. Water was injected into the microreactor at 30 μL min^{-1} to remove any methanol. During the water injection a fresh solution of acidified hydrogen peroxide (5:1:1 H_2O/H_2O_2/HCl by volume) was prepared. The "click chip" surfaces were activated by injecting the acidified hydrogen peroxide for 5 min at 30 μL min^{-1} then stopping the injection and letting the chip sit for 5 min. Water, then methanol, and water again were injected to remove the air pockets produced by the hydrogen peroxide solution and remove methanol for further acidic hydrogen peroxide injections. The activation process was repeated 3 more times. Three injections may not be required but this was done because the hydrogen peroxide solution rapidly develops small bubbles which are trapped on chip. Removing bubbles with methanol (other alcohols such as ethanol or isopropanol work

well too) in between acidic hydrogen peroxide solution injections may improve the amount of the surface activated.

After the final acidified hydrogen peroxide rinse the microreactor was quickly flushed with water then methanol. The syringe of neat TMSPA was removed from the glove bag and silane was injected into the microreactor at room temperature for 5 min at 20 μL min^{-1}, then the flow was reduced to 4 μL min^{-1} for 1 h. The chip was rinsed with methanol then air was injected into the chip to remove methanol and the chip was heated in a 65 °C oven for 2 h, and then cooled to room temperature. The chip was then rinsed with methanol then water.

A water-soluble derivative of the Cu(I) ligand tris-(benzyltriazolylmethyl)amine (TBTA) was synthesized as described in Chapter 2.[27] A 20 mM solution of the water-soluble TBTA derivative was created by adding 628 μL of water to 8.24 mg (12.6 μmol) of the water-soluble Cu(I) ligand. Borax (12.39 mg, 61.57 μmol) was added to the ligand solution to catalyze the aza-Michael reaction[39] that covalently links the ligand with the immobilized TMSPA. The solution was placed in a bath sonicator for 10 min. The silane-coated microreactor was rinsed with methanol then water followed by injection of the Cu(I) ligand and borax solution at 20 μL min^{-1} for 6 min. The tubing was removed and ports covered with Crystal Clear tape, then the microreactor was incubated at room temperature for 18 h. More Cu(I) ligand solution was injected followed by a 6 h incubation at room temperature. After this the chip was rinsed with methanol, water, and air, and stored until use for conjugation reactions.

Minimizing silane contamination

COC/PDMS/glass chips were functionalized similar to the process described in the ligand immobilization process section above, but the procedure was halted after rinsing chips with methanol. Four parameters of the silane attachment process were varied as outlined by **Table**

3.2. Aqueous solutions consisting of 8 v/v% DMSO in water were incubated in the devices for 2 h at 47 °C using the humidified petri dishes as described in the solvent loss section. The incubation solutions were collected and analyzed by LC-MS.

Incubating BFCs with metal ions

Propargyl-DOTA-tris(*tert*-butyl) ester or NO2A-butyne-bis(*tert*-butyl) ester in DMSO, was combined with water (2:3 DMSO/water) to create 3.00 mM solutions. Separate 50 mM metal stock solutions were prepared by dissolving $CuSO_4$, $NiSO_4$, or $FeSO_4$ in 10 mL of water. In separate amber glass vials the appropriate 3.00 mM tBu protected BFC solution (700 μL), 180 mM potassium phosphate buffer pH 7.20 (175 μL), appropriate 50 mM metal solution (63 μL), and water (112 μL) were combined and stirred on a 47 °C hot plate for 4 h along with a control vial of tBu protected BFC with additional water added (63 μL) instead of metal solution. A 3.00 mM solution of azido-mono-amide-DOTA-tris(*tert*-butyl) ester was prepared identically to DOTA-alkyne and NO2A-alkyne and incubated in a similar fashion with a $CuSO_4$ solution so the final Cu concentration was 3.00 mM. The solution was incubated for 4 h at 47 °C. Samples were analyzed by LC-MS. Multiple products with different quantities of tBu groups may be produced after incubating BFCs with metal ions. See **Table 3.3** for MS data of metal-BFC complexes.

Table 3.3. MS (ESI) adduct data for BFCs after incubation with a metal ion. Some incubations formed multiple metal-BFC complexes such as NO2A-alkyne and Cu which formed Cu-NO2A-alkyne products with either 0 or 1 tBu protecting groups.

Compound	$[M+H]^+$ Adduct	Calcd *m/z*	Found *m/z*
Cu-DOTA-alkyne (2 tBu)	$C_{27}H_{46}CuN_5O_7^+$	615.3	615.4
Ni-DOTA-alkyne (2 tBu)	$C_{27}H_{46}N_5NiO_7^+$	610.3	610.4
Cu-NO2A-alkyne (1 tBu)	$C_{20}H_{33}CuN_4O_5^+$	472.2	471.9
Cu-NO2A-alkyne (0 tBu)	$C_{16}H_{25}CuN_4O_5^+$	416.1	415.8
Ni-NO2A-alkyne (0 tBu)	$C_{16}H_{25}N_4NiO_5^+$	411.1	410.8
Cu-DOTA-azide (3 tBu)	$C_{31}H_{58}CuN_8O_7^+$	717.4	717.0
Cu-DOTA-azide (2 tBu)	$C_{27}H_{49}CuN_8O_7^+$	660.3	660.7

Reaction solution preparation

cRGDfK-azide was dissolved in DMSO then water was added to make a 3.00 mM solution (4:1 water/DMSO). EdU was dissolved in DMSO to create a 6.00 mM stock solution. 2.00 mM Cu-BFC solutions were prepared in phosphate buffer as described in the incubating BFCs with metal ions section. Reaction solutions were prepared by combining water, phosphate buffer at pH 7.20 (30 mM final concentration), the appropriate BM stock solution (600 μM final concentration), and Cu-BFC stock solution (400 μM final concentration).

BFC and BM conjugation reactions

A Cu(I) solution was created by combining 8.5 mL of water, 0.5 mL of 50 mM $CuSO_4$ solution, and 1.0 mL of 200 mM sodium ascorbate solution. Chips were rinsed with methanol to remove air bubbles then rinsed with water. Cu(I) solution was injected through the side with a single interface port for 25 min at 30 μL min^{-1} then allowed to sit for 3 min. Then, Cu(I) solution was injected through both ports on the opposite side at 15 μL min^{-1} for 25 min. Water was injected for 20 min at 30 μL min^{-1} to rinse the microreactor. The appropriate reagent solution was injected into the "click chip" for 5 min at 20 μL min^{-1}. Microreactors were incubated in a humidified petri dish identically to water loss experiments discussed above. Reaction samples were collected by injecting water into the microreactor at 30 μL min^{-1} for 50 s and collecting the effluent. Microreactors were rinsed with methanol then water and a second reaction was started identical to the first reaction. The process was repeated for a final, third reaction, and microreactors were rinsed with methanol, water, and then air was injected to dry the "click chips" prior to storage. Cu(I) solution was only injected into microreactors prior to the first reaction. Two microreactors were used for each set of reaction parameters for a total of six trials. Reaction samples were analyzed by LC-MS and yields were determined by differences in

reagent peak areas from LC-MS chromatograms of reaction samples and standards for Cu-DOTA-cRGDfK (**Figure 3.16**), Cu-DOTA-EdU (**Figure 3.17**), and Cu-NO2A-cRGDfK (**Figure 3.18**). See **Table 3.4** for MS (ESI) data of Cu-BFC-BM conjugates.

Table 3.4. MS (ESI) adduct data for Cu-BFC-BM conjugates from "click chip" reaction samples. Some reactions formed multiple Cu-BFC-BM products with different numbers of tBu groups such as Cu-DOTA-alkyne and cRGDfK-azide which formed products with 2, 1, or 0 tBu protecting groups.

Compound	$[M+H]^+$ Adduct	Calcd *m/z*	Found *m/z*
Cu-DOTA-cRGDfK (2 tBu)	$C_{54}H_{85}CuN_{16}O_{14}^+$	1244.6	1244.9
Cu-DOTA-cRGDfK (1 tBu)	$C_{50}H_{77}CuN_{16}O_{14}^+$	1188.5	1188.8
Cu-DOTA-cRGDfK (0 tBu)	$C_{46}H_{69}CuN_{16}O_{14}^+$	1132.4	1132.7
Cu-NO2A-cRGDfK (1 tBu)	$C_{47}H_{72}CuN_{15}O_{12}^+$	1101.5	1101.6
Cu-NO2A-cRGDfK (0 tBu)	$C_{43}H_{64}CuN_{15}O_{12}^+$	1045.4	1045.6
Cu-DOTA-EdU (2 tBu)	$C_{38}H_{61}CuN_{10}O_{12}^+$	912.4	913.1
Cu-DOTA-EdU (1 tBu)	$C_{34}H_{53}CuN_{10}O_{12}^+$	856.3	857.1

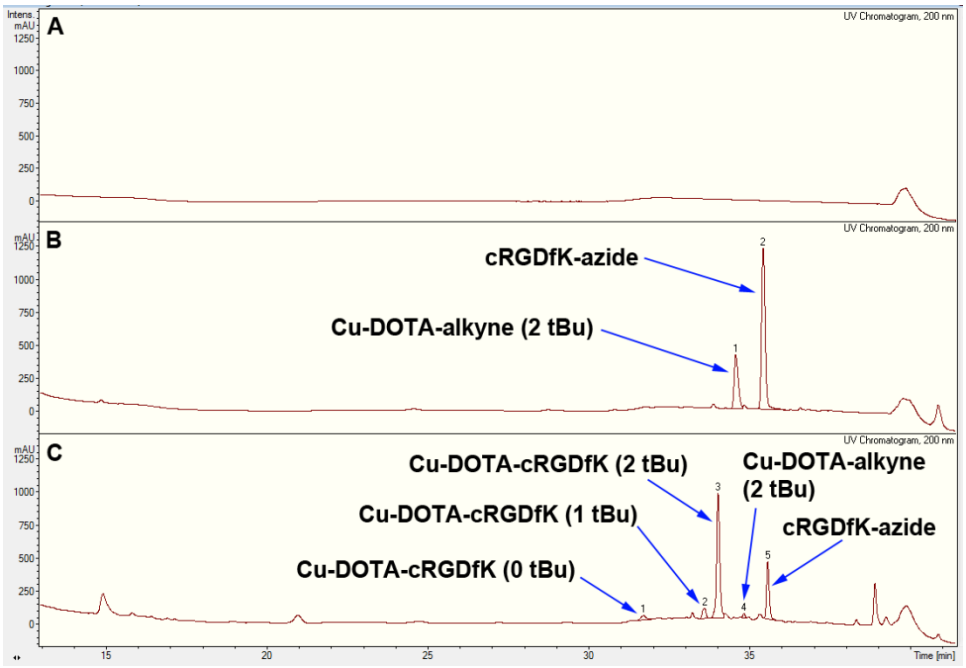

Figure 3.16. LC-MS UV chromatograms of a blank without any injection (A), initial Cu-DOTA-alkyne and cRGDfK-azide reagent solution prior to reaction (B), and the first sample collected from a reactor after incubating for 12 h at 47 °C (C). The peaks at ~15 min and ~21 min are due to silane contamination leaking from the PDMS which can be avoided by proper pretreatment of the PDMS chip.

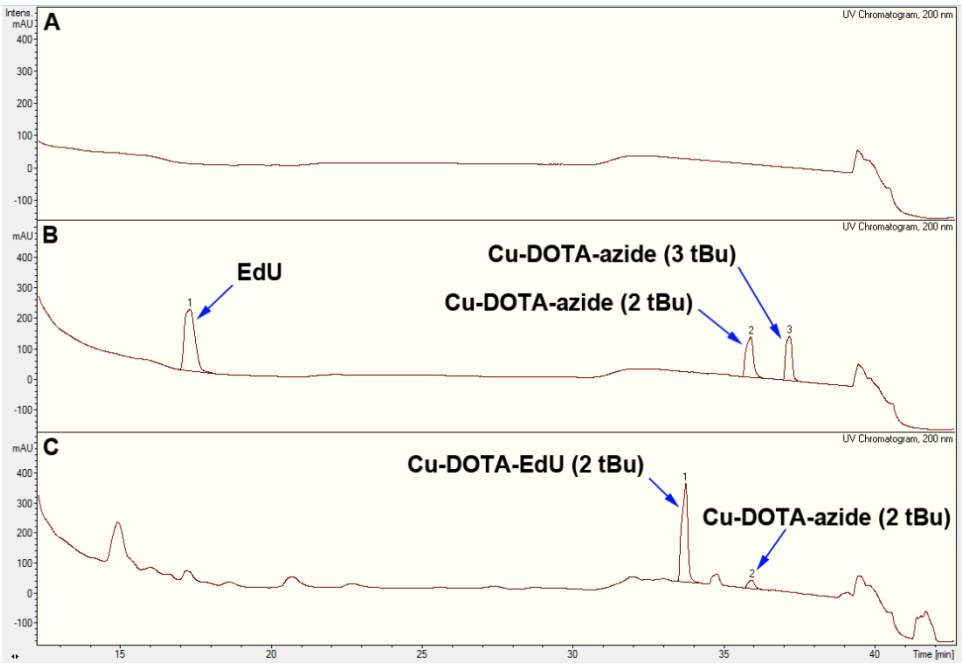

Figure 3.17. LC-MS UV chromatograms of a blank without any injection (A), initial Cu-DOTA-azide and EdU reagent solution prior to reaction (B), and the first sample collected from a reactor after incubating for 12 h at 47 °C (C).

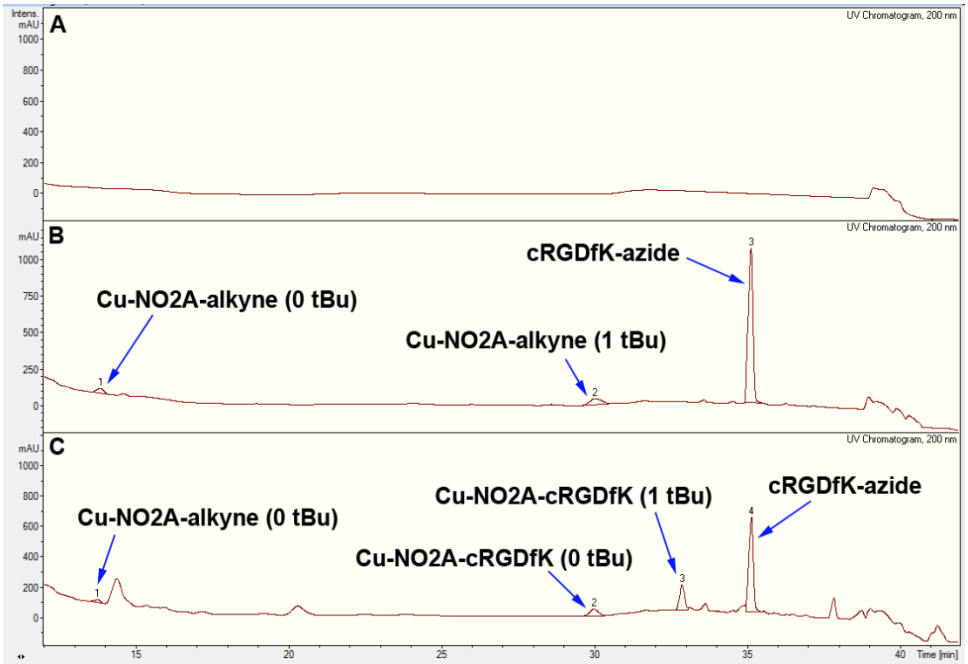

Figure 3.18. LC-MS UV chromatograms of a blank without any injection (A), initial Cu-NO2A-alkyne and cRGDfK-azide reagent solution prior to reaction (B), and the first sample collected from a reactor after incubating for 12 h at 47 °C (C).

Quantifying Cu(I) catalyst loss

A 9.3 v/v% DMSO solution in water was created to mimic the reagent solution used for "click chip" BFC and BM conjugation reactions. Three "reactions" were performed on two microreactors identically to the method used for BFC and BM conjugation reactions except methanol and water used to rinse the chips following each incubation were collected in addition to incubation samples. Samples and rinses were combined in two separate vials for each microreactor because ICP-OES requires ~3-5 mL of sample and dilution of individual samples may reduce Cu concentration below detection limits. Solvent for each sample was evaporated under vacuum then placed in a vacuum oven overnight to ensure removal of all methanol. Nitric acid solution (3 mL, 100 mM) was added to each sample. Samples were transferred between different vials during processing so a portion of the nitric acid solution was aliquoted to previously used vials, vortex mixed, then transferred back to the sample container to reduce Cu loss from adsorption to container walls. Samples were diluted with an additional 2 mL of water and Cu concentration was quantified for each sample by ICP-OES. The 100 mM nitric acid solution was also analyzed and confirmed minimal amounts of Cu (~0.005 ppm) present in this solution compared to incubation and rinse samples with Cu concentrations between roughly 0.5-5 ppm.

3.4 Conclusions

Here a thin "click chip" with an immobilized Cu(I) catalyst suitable for CuAAC conjugation of biomolecules and bifunctional chelators was developed. The microreactor design was improved from the previous "click chip" described in Chapter 2, to reduce solvent loss for longer reactions by reducing PDMS thickness and bonding a more gas impermeable COC layer on top of the PDMS. Using the new "click chip" design, BM-BFC conjugates using either a peptide,

which are easily synthesized and have ideal *in vivo* clearance characteristics, or a nucleoside, representative of the recent interest in DNA or RNA based imaging agents because of their low immunogenicity and stable structure were synthesized. Additionally, a wide variety of BFCs are utilized in radiotracer synthesis largely depending on the desired radiometal. Three different BFC derivatives of DOTA or NO2A, two widely used bifunctional chelators, were used in "click" reactions on chip. The ability to synthesize three different BM-BFC conjugates, without potentially harmful microwave irradiation or high temperatures, demonstrates the flexibility of the "click chips" to facilitate conjugation reactions under mild conditions. Cu(I) catalyst loss was observed but the concentration of copper in reaction samples was minute (~20 ppm), reducing or obviating the need to remove copper from reaction solutions, and enabling direct injection of crude reaction samples into LC-MS systems. Thus enabling rapid purification of BFC-BM conjugates.

Additionally, tBu loss from protected BFCs was further explored. Some previous work has mentioned hydrolysis of tBu esters from protected BFCs, but the few papers that do discuss tBu loss are mostly DOTA-alkyne species. No systematic data exists on how other protected chelators respond to CuAAC reaction conditions. The work described here in Chapter 3 demonstrated that *tert*-butyl ester hydrolysis occurs for BFCs besides tBu protected DOTA-alkyne in the presence of metal ions, and that the quantity of tBu protecting groups lost depends on the BFC and metal ion. Further work determining the effects of other parameters (e.g., temperature) were not studied, but are worthy of further research.

Due to tBu ester hydrolysis by copper, even when Cu(I) catalyst was immobilized, the BFCs chelated Cu(I) catalyst. Therefore, BFC complexes were pre-chelated with Cu(II) ions to reduce loss of immobilized Cu(I) catalyst. Copper ions from the Cu-BFC-BM product were not

removed. Two general radiometal-based radiotracer production methods using "click" chemistry can be used; either chelate then "click" or vice versa. The "click chip" described here will likely be useful for chelate then "click" schemes where radiometal chelation occurs prior to conjugation to the appropriate BM. This nullifies the need to remove copper ions from the Cu-BFC-BM product because ^{64}Cu or the desired radiometal is already chelated.

3.5 References

(1) James, M. L., and Gambhir, S. S. (2012) A Molecular Imaging Primer: Modalities, Imaging Agents, and Applications. *Physiol. Rev. 92*, 897-965.

(2) Kong, F. L., Kim, E. E., and Yang, D. J. (2012) Targeted Nuclear Imaging of Breast Cancer: Status of Radiotracer Development and Clinical Applications. *Cancer Biother. Radiopharm. 27*, 105-112.

(3) Uz Zaman, M., Fatima, N., Sajjad, Z., Zaman, U., Tahseen, R., and Zaman, A. (2014) 18FDG Synthesis and Supply: a Journey from Existing Centralized to Future Decentralized Models. *Asian Pac. J. Cancer Prev. 15*, 10057-10059.

(4) Wadas, T. J., Wong, E. H., Weisman, G. R., and Anderson, C. J. (2010) Coordinating Radiometals of Copper, Gallium, Indium, Yttrium, and Zirconium for PET and SPECT Imaging of Disease. *Chem. Rev. 110*, 2858-2902.

(5) Zeglis, B. M., Houghton, J. L., Evans, M. J., Viola-Villegas, N., and Lewis, J. S. (2014) Underscoring the Influence of Inorganic Chemistry on Nuclear Imaging with Radiometals. *Inorg. Chem. 53*, 1880-1899.

(6) Zeglis, B. M., and Lewis, J. S. (2011) A practical guide to the construction of radiometallated bioconjugates for positron emission tomography. *Dalton Trans. 40*, 6168-6195.

(7) Knör, S., Modlinger, A., Poethko, T., Schottelius, M., Wester, H.-J., and Kessler, H. (2007) Synthesis of Novel 1,4,7,10-Tetraazacyclodecane-1,4,7,10-Tetraacetic Acid (DOTA) Derivatives for Chemoselective Attachment to Unprotected Polyfunctionalized Compounds. *Chem. – Eur. J. 13*, 6082-6090.

(8) Kolb, H. C., Finn, M. G., and Sharpless, K. B. (2001) Click chemistry: Diverse chemical function from a few good reactions. *Angew. Chem., Int. Ed. 40*, 2004-2021.

(9) Wangler, C., Schirrmacher, R., Bartenstein, P., and Wangler, B. (2010) Click-chemistry reactions in radiopharmaceutical chemistry: fast & easy introduction of radiolabels into biomolecules for in vivo imaging. *Curr. Med. Chem. 17*, 1092-116.

(10) Cai, Z. X., Li, B. T. Y., Wong, E. H., Weisman, G. R., and Anderson, C. J. (2015) Cu(I)-assisted click chemistry strategy for conjugation of non-protected cross-bridged macrocyclic chelators to tumour-targeting peptides. *Dalton Trans. 44*, 3945-3948.

(11) Schultz, M. K., Parameswarappa, S. G., and Pigge, F. C. (2010) Synthesis of a DOTA-Biotin Conjugate for Radionuclide Chelation via Cu-Free Click Chemistry. *Org. Lett. 12*, 2398-2401.

(12) Wangler, C., Schirrmacher, R., Bartenstein, P., and Wangler, B. (2009) Simple and convenient radiolabeling of proteins using a prelabeling-approach with thiol-DOTA. *Bioorg. Med. Chem. Lett. 19*, 1926-1929.
(13) Mindt, T. L., Schweinsberg, C., Brans, L., Hagenbach, A., Abram, U., Tourwe, D., Garcia-Garayoa, E., and Schibli, R. (2009) A click approach to structurally diverse conjugates containing a central di-1,2,3-triazole metal chelate. *ChemMedChem 4*, 529-539.
(14) Lebedev, A. Y., Holland, J. P., and Lewis, J. S. (2010) Clickable bifunctional radiometal chelates for peptide labeling. *Chem. Commun. 46*, 1706-1708.
(15) Hong, V., Presolski, S. I., Ma, C., and Finn, M. G. (2009) Analysis and optimization of copper-catalyzed azide-alkyne cycloaddition for bioconjugation. *Angew. Chem., Int. Ed. Engl. 48*, 9879-9883.
(16) Hong, V., Steinmetz, N. F., Manchester, M., and Finn, M. G. (2010) Labeling Live Cells by Copper-Catalyzed Alkyne-Azide Click Chemistry. *Bioconjug. Chem. 21*, 1912-1916.
(17) Li, S., Cai, H., He, J., Chen, H., Lam, S., Cai, T., Zhu, Z., Bark, S. J., and Cai, C. (2016) Extent of the Oxidative Side Reactions to Peptides and Proteins During the CuAAC Reaction. *Bioconjug. Chem. 27*, 2315-2322.
(18) Liu, K., Wang, M. W., Lin, W. Y., Phung, D. L., Girgis, M. D., Wu, A. M., Tomlinson, J. S., and Shen, C. K. F. (2011) Molecular Imaging Probe Development Using Microfluidics. *Curr. Org. Synth. 8*, 473-487.
(19) Elizarov, A. M. (2009) Microreactors for radiopharmaceutical synthesis. *Lab Chip 9*, 1326-1333.
(20) Taggart, M. P., Tarn, M. D., Esfahani, M. M., Schofield, D. M., Brown, N. J., Archibald, S. J., Deakin, T., Pamme, N., and Thompson, L. F. (2016) Development of radiodetection systems towards miniaturised quality control of PET and SPECT radiopharmaceuticals. *Lab Chip 16*, 1605-1616.
(21) Pascali, G., Watts, P., and Salvadori, P. A. (2013) Microfluidics in radiopharmaceutical chemistry. *Nucl. Med. Biol. 40*, 776-787.
(22) Lebedev, A., Miraghaie, R., Kotta, K., Ball, C. E., Zhang, J. Z., Buchsbaum, M. S., Kolb, H. C., and Elizarov, A. (2013) Batch-reactor microfluidic device: first human use of a microfluidically produced PET radiotracer. *Lab Chip 13*, 136-145.
(23) Wheeler, T. D., Zeng, D., Desai, A. V., Onal, B., Reichert, D. E., and Kenis, P. J. A. (2010) Microfluidic labeling of biomolecules with radiometals for use in nuclear medicine. *Lab Chip 10*, 3387-3396.
(24) Zeng, D. X., Desai, A. V., Ranganathan, D., Wheeler, T. D., Kenis, P. J. A., and Reichert, D. E. (2013) Microfluidic radiolabeling of biomolecules with PET radiometals. *Nucl. Med. Biol. 40*, 42-51.
(25) Mate, G., Szikra, D., Simecek, J., Szilagyi, S., Trencsenyi, G., Wester, H.-J., Kertesz, I., and Galuska, L. (2016) Multiparametric labeling optimization and synthesis of 68Ga-labeled compounds applying a continuous-flow microfluidic methodology. *J. Flow Chem. 6*, 86-93.
(26) Wright, B. D., Whittenberg, J. J., Desai, A., DiFelice, C., Kenis, P., Lapi, S., and Reichert, D. E. (2016) Microfluidic Preparation of an 89Zr-Labeled Trastuzumab Single Patient Dose. *J. Nucl. Med. 57*, 747-752.

(27) Li, H., Whittenberg, J. J., Zhou, H., Ranganathan, D., Desai, A. V., Koziol, J., Zeng, D., Kenis, P. J. A., and Reichert, D. E. (2015) Development of a microfluidic "click chip" incorporating an immobilized Cu(I) catalyst. *RSC Adv. 5*, 6142-6150.
(28) Dijkgraaf, I., Rijnders, A. Y., Soede, A., Dechesne, A. C., van Esse, G. W., Brouwer, A. J., Corstens, F. H. M., Boerman, O. C., Rijkers, D. T. S., and Liskamp, R. M. J. (2007) Synthesis of DOTA-conjugated multivalent cyclic-RGD peptide dendrimers via 1,3-dipolar cycloaddition and their biological evaluation: implications for tumor targeting and tumor imaging purposes. *Org. Biomol. Chem. 5*, 935-944.
(29) Mindt, T. L., Muller, C., Stuker, F., Salazar, J.-F. d. r., Hohn, A., Mueggler, T., Rudin, M., and Schibli, R. (2009) A "Click Chemistry" Approach to the Efficient Synthesis of Multiple Imaging Probes Derived from a Single Precursor. *Bioconjug. Chem. 20*, 1940-1949.
(30) Mortellaro, M. A., Bleisch, T. J., Duerr, B. F., Kang, M. S., Huang, H., and Czarnik, A. W. (1995) Metal Ion-Catalyzed Hydrolysis of Acrylate Esters and Amides by Way of Their Conjugate Addition Adducts. *J. Org. Chem. 60*, 7238-7246.
(31) Li, H., Zhou, H., Krieger, S., Parry, J. J., Whittenberg, J. J., Desai, A. V., Rogers, B. E., Kenis, P. J. A., and Reichert, D. E. (2014) Triazine-Based Tool Box for Developing Peptidic PET Imaging Probes: Syntheses, Microfluidic Radiolabeling, and Structure–Activity Evaluation. *Bioconjug. Chem. 25*, 761-772.
(32) Notni, J., and Wester, H. J. (2016) A Practical Guide on the Synthesis of Metal Chelates for Molecular Imaging and Therapy by Means of Click Chemistry. *Chem. – Eur. J. 22*, 11500-11508.
(33) Bevilacqua, V., King, M., Chaumontet, M., Nothisen, M., Gabillet, S., Buisson, D., Puente, C., Wagner, A., and Taran, F. (2014) Copper-Chelating Azides for Efficient Click Conjugation Reactions in Complex Media. *Angew. Chem., Int. Ed. 53*, 5872-5876.
(34) Kriemen, E., Ruf, E., Behrens, U., and Maison, W. (2014) Synthesis of 1,4,7,10-Tetra-azacyclododecan-1,4,7,10-tetra-azidoethylacetic Acid (DOTAZA) and Related "Clickable" DOTA Derivatives. *Chem. – Asian J. 9*, 2197-2204.
(35) Reubi, J. C. (2003) Peptide receptors as molecular targets for cancer diagnosis and therapy. *Endocr. Rev. 24*, 389-427.
(36) Chen, Z. Y., Wang, Y. X., Lin, Y., Zhang, J. S., Yang, F., Zhou, Q. L., and Liao, Y. Y. (2014) Advance of Molecular Imaging Technology and Targeted Imaging Agent in Imaging and Therapy. *Biomed. Res. Int. 2014*, 1.
(37) Liu, S. (2015) Radiolabeled Cyclic RGD Peptide Bioconjugates as Radiotracers Targeting Multiple Integrins. *Bioconjug. Chem. 26*, 1413-1438.
(38) Strand, J., Honarvar, H., Perols, A., Orlova, A., Selvaraju, R. K., Karlstrom, A. E., and Tolmachev, V. (2013) Influence of Macrocyclic Chelators on the Targeting Properties of Ga-68-Labeled Synthetic Affibody Molecules: Comparison with In-111-Labeled Counterparts. *PLoS One 8*, e70028.
(39) Hussain, S., Bharadwaj, S. K., Chaudhuri, M. K., and Kalita, H. (2007) Borax as an efficient metal-free catalyst for hetero-Michael reactions in an aqueous medium. *Eur. J. Org. Chem.*, 374-378.

Chapter 4

Design and characterization of a millifluidic herringbone mixer*

4.1 Introduction

Micro- and millifluidic platforms have been utilized for multiple synthetic applications, including tumor imaging agent production[1], generating pharmaceuticals[2, 3], and general organic and inorganic synthesis[4-6]. In particular, small-scale continuous flow platforms are advantageous relative to conventional batch systems due to (i) greater control of reaction parameters (e.g., temperature), (ii) simpler scale-up, and (iii) potential for automation.[7] These small-scale continuous flow platforms consist of multiple unit operations such as mixing, chemical transformations, and separations.[8] Off-the-shelf microreactors utilized in continuous flow platforms are commercially available and can improve the transition from academic research to industrial production while simultaneously reducing the need for expertise and equipment for microfabrication.[9] The continued development of small-scale continuous flow systems and individual unit operations will further the adoption of micro- and millifluidic platforms in both academia and industry.

One crucial unit operation used in many small-scale continuous flow systems is mixing, via an active or passive approach. Active mixers require an external energy supply (e.g., acoustic waves, magnetic fields) to reduce mixing time while passive mixers require only pressure head and rely on structures in the mixer to manipulate fluid flow.[10] The lack of moving parts and/or external energy sources makes passive mixers inherently easier to fabricate and operate; especially for microfluidic platforms that have a characteristic dimension typically on the scale

*This chapter has been adapted from the following manuscript: Whittenberg, J. J., Kumar, V., Lane, K. R., Verma, S., Patel, H. S., Kenis, P. J. A. Design and Characterization of a Millifluidic Herringbone Mixer. This manuscript was under review for publication at the time of submission of this dissertation.

of 10's to 100's of micrometers. Microfluidic passive mixers have been studied extensively over the past decades.[10, 11] However, few efforts have focused on millifluidic mixers.[12] Millifluidic platforms, with characteristic dimensions near 1 mm to a few millimeters, have similar advantages to microfluidic platforms such as rapid mass and heat transfer.[5] Yet, millifluidic platforms enable higher throughput, are simpler to fabricate and operate, and easier to interface with laboratory equipment.[2, 5, 13]

A wide variety of passive mixer designs have been utilized in microfluidic systems, including zigzag channels, 3-D serpentine structures, and slanted wells.[10] One particular design, the staggered herringbone mixer (SHM) developed by Stroock et al.[14], is frequently utilized in microfluidics because of its simple design and proven capability as an efficient mixer for continuous flow systems.[15, 16] The SHM consists of asymmetric grooves that add a transverse component to fluid flow that splits, stretches, and folds fluid to reduce diffusion distances and subsequently reduce mixing time.[11, 14] The SHM pattern not only enables rapid mixing, but also creates a highly uniform residence time distribution (RTD) similar to a plug flow distribution.[17]

Determining what has been accomplished at the millifluidic scale is challenging. The term "millifluidic" is not as well characterized and utilized as "microfluidic". For example other terms including "milliscale" and "mesofluidic" may be used instead to describe systems near the millimeter length scale, and occasionally the term "microfluidic" is still used. A previous scaled-up SHM was fabricated, but with the herringbone structures sandwiched in between two channels instead of on the top or bottom of the channel.[18] The RTD of the layered herringbone device was determined, but mixing efficiency was not quantified and the residence time required for the reaction under consideration required 10's to 100's of seconds for optimal conversion.[18]

In this chapter I discuss the development of a millifluidic herringbone mixer capable of rapid mixing that is critical for fast reactions to reduce mass transfer limitations.

Nanoparticle (NP) synthesis is one example reaction that typically requires fast mixing and a narrow RTD due to the rapid kinetics of nanoparticle formation and growth. Inhomogeneity in mixing during NP synthesis contributes to high polydispersity and poor batch-to-batch reproducibility.[19] Microfluidic platforms have been utilized previously to synthesize NPs including a SHM platform.[20, 21] However, millifluidic platforms are particularly advantageous for NP production because of higher throughput and, more critical for metal NP synthesis, reduced chance of channel clogging.[13] Previous work has leveraged the advantages of millifluidic continuous flow set-ups for NP synthesis. A turbulent jet mixer was developed for high-throughput nanoparticle production, but requires a specific flow regime to produce a stable jet.[22] Additionally, other previously reported platforms have been based primarily on mixing by diffusion with limited mixing in the transversal (perpendicular to fluid flow) direction. Advances in mixer design could provide improved control on NP properties such as particle size distribution.[13] A millifluidic SHM capable of faster mixing in the transversal direction relative to previous diffusion-based designs that are currently utilized can improve NP synthesis.

In Chapter 4 I discuss the development and characterization of a simple millifluidic SHM. To develop the millifluidic SHM computational fluid dynamics (CFD) simulations were first used to optimize the SHM dimensions. The resulting mixer design was readily fabricated using a conventional CNC milling machine. The scaled-up SHM was (1) characterized by using aqueous dye solutions to confirm mixing capability and (2) validated by synthesizing gold nanoparticles (AuNPs) in the mixer to demonstrate one potential application of the millifluidic mixer.

4.2 Results and discussion

The envisioned fabricated millifluidic SHM design would have a similar structure to previously constructed microfluidic herringbone mixers for scaled-up mixing and reaction applications. The general SHM design consists of individual grooves with one long arm and one short arm embedded in the channel at an angle with respect to the channel sidewall. The asymmetry of the individual grooves creates two separate helical flows of different sizes. Only asymmetric grooves were used for the millifluidic SHM design described in Chapter 4 and the terms groove and herringbone are used interchangeably. A set number of individual grooves with the same orientation of long and short arms, called a half-cycle, are placed in a row downstream of each other. The orientation is then reflected so the short and long arms are on opposites sides of the channel to create a second half-cycle (**Figure 4.1A**). The two half-cycles with opposite orientation make one full-cycle, and a typical SHM design contains multiple full-cycles to completely mix solutions. The change in orientation between half-cycles alters the center of rotation and creates a chaotic flow which exponentially decreases diffusion distance enabling rapid mixing.[14, 23]

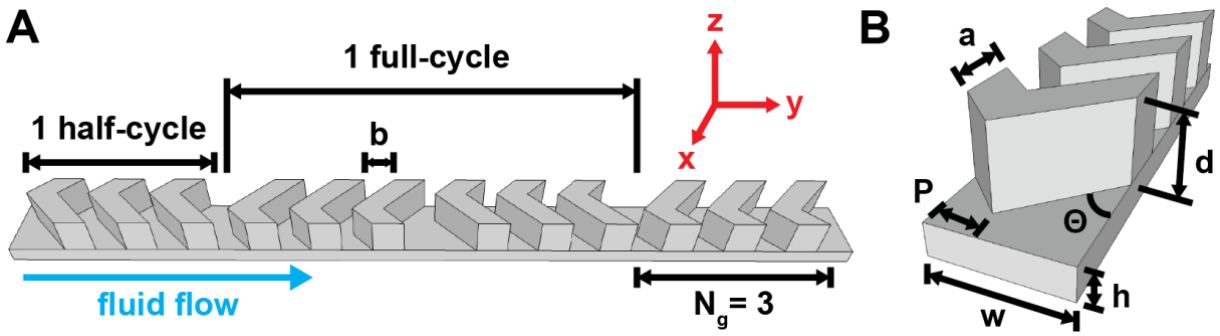

Figure 4.1. Schematics of a channel with herringbones with the number of grooves per half-cycle and spacing between individual herringbones (A) and labels displaying the variables and constants utilized to define channel and individual herringbone dimensions (B).

The mixer design, fabrication, and testing process consisted of CFD simulations, fabricating the millifluidic SHMs, characterizing mixing, and validating the mixer design by synthesizing nanoparticles. The main goal of CFD simulations was to guide the millifluidic SHM design for experimental verification and validation. Three factors, (1) groove width, (2) groove depth, and (3) distance between grooves, were varied in CFD simulations to optimize one criterion, extent of mixing. Extent of mixing in fabricated millifluidic SHMs was characterized by analyzing the mixing of aqueous dye solutions at various flow rates. One potential application of the millifluidic SHM was validated by demonstrating synthesis of gold nanoparticles.

CFD simulations

A multitude of CFD simulations have been performed to improve groove mixer design, including SHMs. Previous simulations analyzed how adjusting variables, especially channel and individual herringbone (HB) dimensions (**Figure 4.1B**), affect mixing. Previously studied parameters include channel width (w)[24], channel height (h)[24, 25], groove depth (d)[17, 23, 26], groove width (a)[17], groove angle relative to the y-axis (θ)[27], the asymmetry factor (P)[24], the distance between successive grooves (b)[23], and the number of grooves per half-cycle (N_g)[17] affect mixing performance (**Figure 4.1**). Other factors not related to channel dimensions (e.g., flow rate) have also been tested.[23] Some previous work has even considered multi-objective optimization with two or three criterion (e.g., mixing performance and pressure drop).[24, 26] However, most prior work focused on optimizing microfluidic SHMs with small deviations from the original SHM developed by Stroock et al.[23]

CFD simulations were utilized to optimize HB dimensions for fabrication and experimental validation of a millifluidic SHM. For all simulations channel width (800 μm) and channel height (200 μm) were held constant to maintain a wetted perimeter (~2 mm) similar to 1/8" stainless

steel tubing and 20 gauge PTFE tubing typically used by the Kenis lab. Additionally, the groove angle (45°) and asymmetry factor (1/3) were held constant for all simulations because these values have been optimized previously and are typically conserved in microfluidic SHM simulations.[14, 28] For this work three factors, groove width (a), groove depth (d), and distance between grooves (b), were optimized using CFD simulations. Groove width and groove depth in particular are key factors when optimizing mixer performance.[26, 27, 29]

For this project, three factors were tuned to optimize one criterion, extent of mixing. Previous efforts optimized SHM mixers from CFD simulations by analyzing flow-based descriptors (e.g., non-axial velocities)[30], particle tracking techniques[31], and mixing index[24] or a similar term, coefficient of variation (CoV)[23]. CoV was used to determine the completeness of mixing in both CFD simulations and experiments discussed in detail later because this is a commonly utilized method for both SHMs and static mixers in general,.[23, 32] CoV is defined as the ratio of the standard deviation of a distribution (e.g., concentration, intensity) by the mean of the distribution. CoV values nearer to zero indicate higher uniformity and hence more completely mixed solutions. For CFD simulations the CoV of the xz-plane at channel position y (CoV_y) is calculated by:

$$CoV_y = \frac{\sqrt{\frac{\iint (c - \bar{c})^2 dA}{A}}}{\bar{c}} \quad \textbf{(4.1)}$$

Where c is the concentration of the solute, $\bar{c}$ is the average concentration, and A is the area of the xz-plane analyzed, in this case the channel outlet for all simulations.

Similar to prior work[23] the SHM design was optimized in multiple steps: (1) optimize the dimensions of a single HB (**Figure 4.2A**) by adjusting groove width and depth and (2) determine ideal distance between two herringbones (**Figure 4.3A**). For the first step, groove width and

groove depth were varied between 200 μm and 800 μm with a step size of 100 μm, and simulations of all 49 combinations of groove width and groove depth were performed. Groove depth and width were optimized in the single HB simulations here because of their strong impact on mixing efficiency.[23, 27] Wide and deep grooves have previously been demonstrated to promote rapid mixing.[26]

Based on CoV calculations (**Equation 4.1**) at the channel outlet of single HB simulations the optimum groove width was 600 μm (**Figure 4.2B**). CoV began to increase slightly when groove width was increased to 700 μm or 800 μm. Deeper grooves did reduce CoV, but improvements in mixing completeness were marginal above groove depths of approximately 400-500 μm depending on the groove width (**Figure 4.2B**). For example, the CoV for a herringbone with a groove width of 600 μm and depth of 800 μm was only 0.002 lower than a groove with the same width but a depth of 500 μm. Previous work indicated average transversal velocity (used to determine mixing effectiveness) did not improve beyond a certain groove depth and width[23], and the CFD simulation results discussed in this chapter showed the same result with a local CoV minima achieved by a groove width of 600 μm and groove depth of 800 μm.

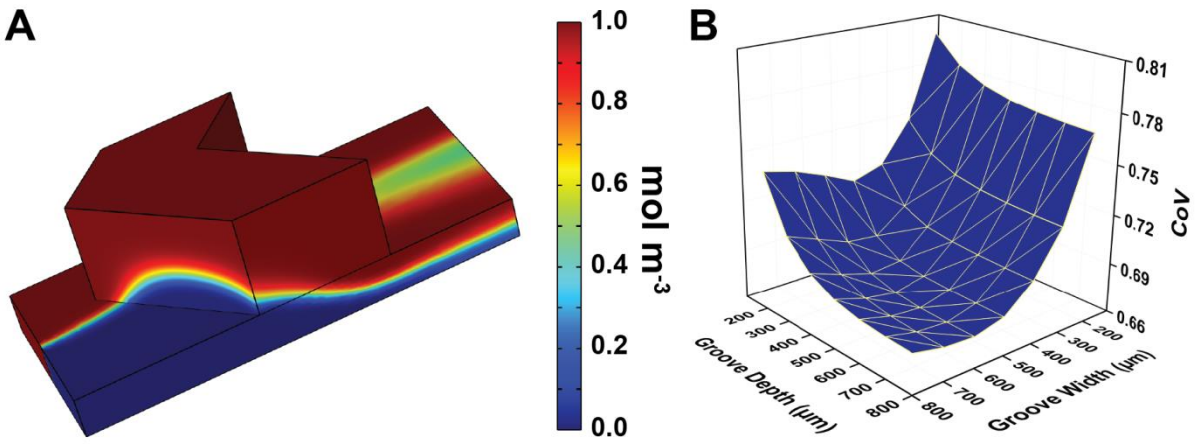

Figure 4.2. Image of a COMSOL simulation of a single HB displaying solute concentration that was used to determine optimum groove width and groove depth (A) and a surface plot of CoV results, calculated at the channel outlet, from all 49 simulations of single HBs with different groove widths and depths (B).

After optimizing individual groove dimensions, simulations containing two herringbones were conducted to optimize the distance between grooves (**Figure 4.3A**). Herringbone width (600 μm) and depth (500 μm) were held constant while the distance between herringbones was altered between 200 μm and 1000 μm with a 100 μm step size. A groove depth of 500 μm was chosen to reduce computation time and because groove depths greater than 500 μm resulted in marginal improvements in single HB mixing effectiveness based on single HB simulations. The CoV at the channel outlet of each simulation was calculated using **Equation 4.1**, and results indicated CoV continued to decrease as the distance between herringbones increased (**Figure 4.3B**). The trend of improved mixing for increased distance between grooves is similar to previous work that also indicated the best SHM geometry (lowest CoV) had the greatest distance between herringbones.[23]

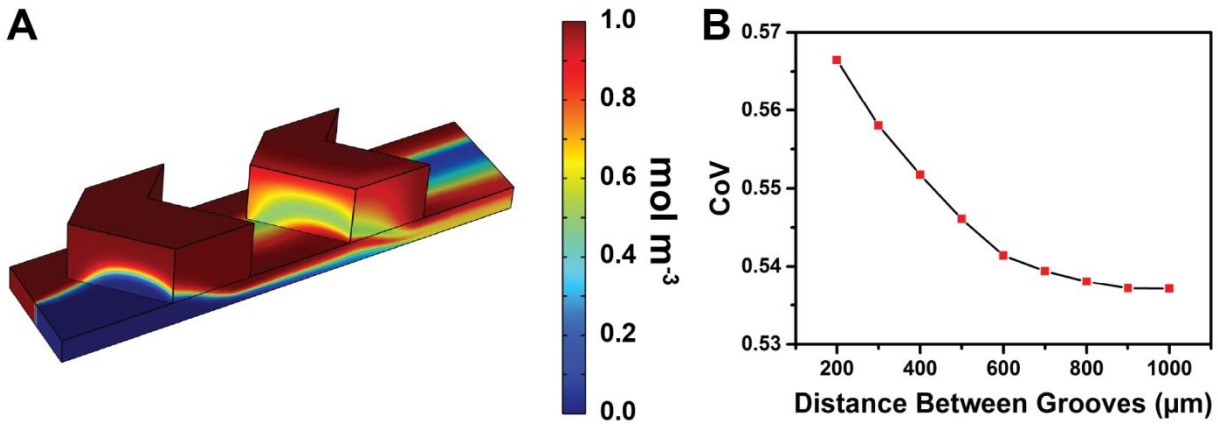

Figure 4.3. Image of a COMSOL simulation with two HBs displaying solute concentration that was used to determine ideal distance between grooves (A) and a graph of CoV results, calculated at the channel outlet, from all inter-groove distance simulations (B).

However, determining an optimum distance between grooves is more challenging than varying distance between two HBs; primarily because another HB can be added for any distance between grooves greater than groove width. To demonstrate the effects of adding an additional herringbone another simulation was performed with three HBs and 200 μm spacing between

grooves (data not shown), holding all other parameters the same as two HB simulations. Therefore, the three HB simulation was identical to the two HB simulation with 1000 μm spacing between the grooves, except one additional HB was placed in between the two herringbones. The CoV of the three HB simulation (0.45) was lower than any of the two HB simulations. CoV data from two and three HB simulations indicate that while increased distance between grooves reduces CoV, inter-groove distance should not drastically exceed the groove width because another HB could be added to the mixer.CFD simulations were used to analyze three parameters of a millifluidic SHM: groove width, groove depth, and distance between grooves. The results represent a local optimum and additional computational analysis may further optimize designs. However, identifying a true optimum is computationally intensive and is difficult due to the non-linear nature of the mixing problem[24], and also because of the number of factors involved and potential criterion to optimize. For example, finding a true optimum of distance between grooves requires designing a DOE that also varies the total number of HBs, number of HBs per half-cycle, groove width, and potentially other factors. Here though, I describe an improved millifluidic SHM design based on CFD simulations that was useful for guiding the fabrication of millifluidic SHMs discussed in the next section.

Fabrication of millifluidic mixers

Based on the outcomes of the CFD simulations the initial millifluidic SHM design contained two inlets, one outlet, and 42 herringbones. Previous work suggested there is not a critical number of HBs per half-cycle, but a critical length of each half-cycle.[29] This was later validated by CFD simulations by Sabotin et al., that indicated just two HBs in one half-cycle was enough to efficiently stretch and fold mixing fluids.[23] Therefore, half-cycles consisted of 3 HBs for all

millifluidic SHM designs. The initial mixer design contained 42 herringbones to provide ample number of cycles to characterize the extent of mixing at different flow rates.

Millifluidic SHMs were fabricated in poly(methyl methacrylate) (PMMA) by conventional milling machines. PMMA was selected because the material is readily machined, has excellent optical properties (e.g., low autofluorescence), and is amenable for high-volume device production.[33] A standard CNC milling machine was utilized to fabricate channel and HB features in a 3 mm thick blank PMMA sheet. Due to the fabrication method, the mixer dimensions differed from optimum CFD simulation dimensions. Groove width was changed to 350 μm instead of 600 μm because a 0.014" diameter end mill was utilized for milling the HBs and could easily mill each HB in one pass. Additionally, groove depth was reduced to 500 μm because this is the maximum depth achievable with this end mill. The milling process also produced HBs with rounded corners instead of the sharp corners typically seen in microfluidic SHMs, but previous work indicated rounded corners had no negative effects on mixing performance.[23] Based on CFD simulations (**Figure 4.3B**) inter-groove distance was approximately the same as groove width. Distance between grooves was ~340 μm for HBs in the same half-cycle and ~400 μm for HBs in between half-cycles.

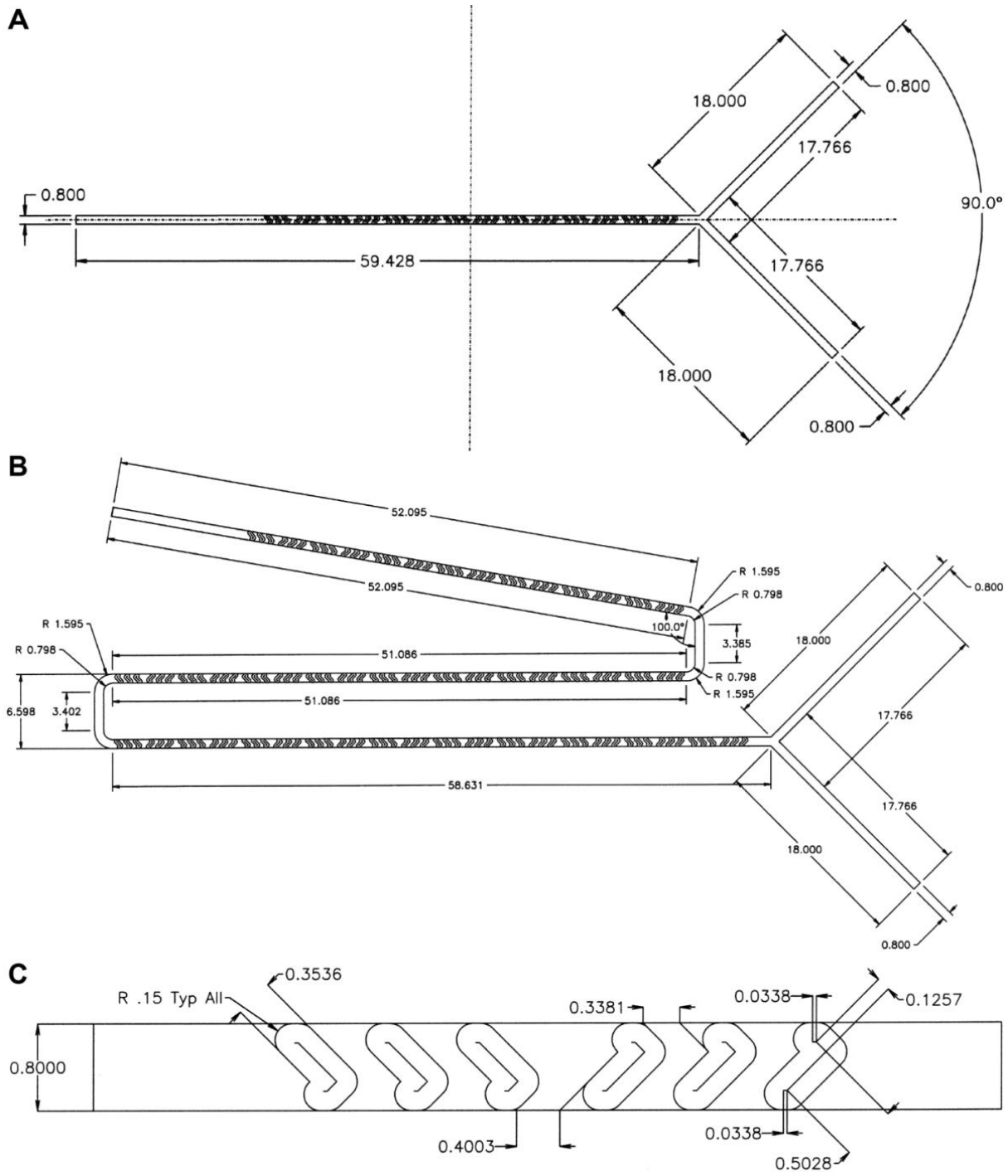

Figure 4.4. Dimensions for the short mixer (A), long mixer (B) and herringbones (C). All dimensions are in millimeters.

Two different millifluidic SHM designs were fabricated (**Figure 4.4**, **Figure 4.5**), and then validated by determining the extent of mixing and ability to synthesize AuNPs. The initial

millifluidic SHM design with 42 HBs (7 full-cycles), referred to as a "short mixer" (**Figure 4.4A**, **Figure 4.5A**), was bonded to another 3 mm thick sheet of PMMA for quantifying the extent of mixing and synthesizing AuNPs. The exact same design was bonded to a thin (175 μm thick) sheet of PMMA, to qualitatively analyze mixing completeness in the z-direction with confocal microscopy. However, an extended millifluidic SHM was required to enable longer residence times for AuNP synthesis, discussed in more detail later. Therefore a new mixer with the same channel width, channel height, and individual HB dimensions, but longer channel length was fabricated with 156 HBs (26 full-cycles). This SHM, referred to as a "long mixer" (**Figure 4.4B**, **Figure 4.5B**), was similarly bonded to 3 mm thick sheets of PMMA and utilized for both quantifying extent of mixing and synthesizing AuNPs.

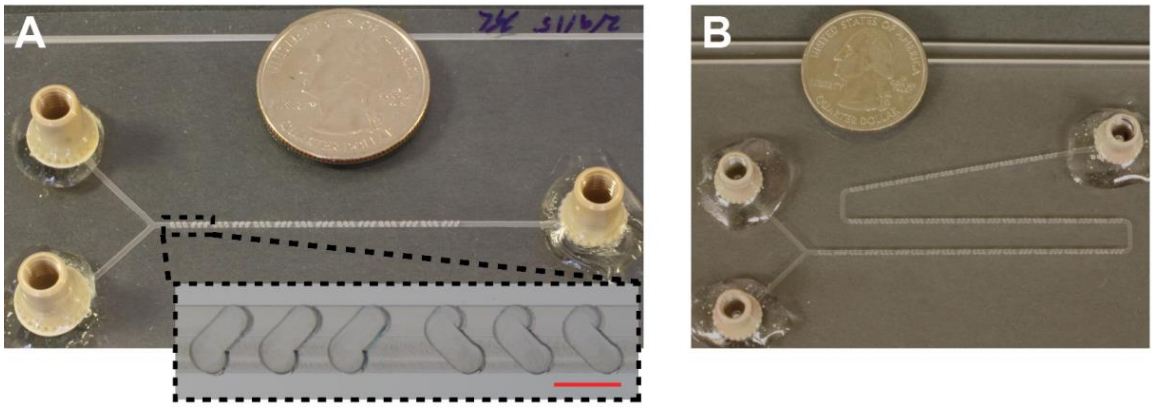

Figure 4.5. Photographs of the two different millifluidic SHM designs fabricated in PMMA, the "short mixer" with 42 HBs (7 full-cycles) and an inset image of one full-cycle of HBs (A) and the "long mixer" with 156 HBs (26 full-cycles) (B). The inset image scale bar is 800 μm.

Characterization of millifluidic mixer performance

Multiple methods have been utilized to characterize the extent of mixing on microfluidic platforms including dilution of colored dyes or fluorescent compounds, reactions generating colored species, and monitoring species concentration.[34] In this work two dyes (Fast Green FCF and Amaranth) dissolved in phosphate buffered saline (PBS) solution were mixed in the

millifluidic SHM devices. Dissolving both dyes in PBS ensures no mismatch in either ionic strength or pH. This dye system was adopted from Werts et al. who optimized conditions to use Fast Green, Amaranth, and other dyes for quantitative analysis on microfluidic devices with non-monochromatic light and digital cameras.[35] A similar technique was used for the work described in this chapter to quantify mixing for fabricated millifluidic SHM designs.

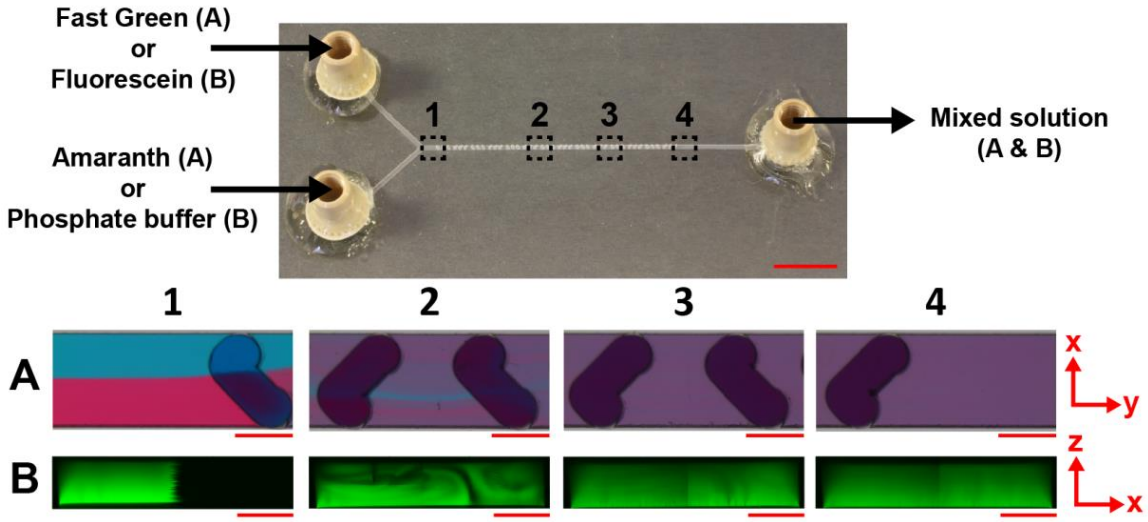

Figure 4.6. Photograph of a short mixer and optical microscope images (A) and confocal microscope images (B) at 4 separate locations along the channel. Optical microscope images depict mixing of aqueous solutions of Fast Green and Amaranth in the xy-plane. Confocal microscope images display mixing of fluorescein and buffer in the xz-plane. Brightness of all confocal images was increased by the same amount in Photoshop (v12.1, Adobe Systems Inc.) to improve visualization and no quantitative data was extracted from confocal images. The scale bars are 1 cm for the short mixer photograph, 500 μm for optical microscope images, and 200 μm for confocal microscope images.

Mixing experiments were performed on the short and long mixers by injecting aqueous solutions of Fast Green and Amaranth in separate inlets at equal flow rates (**Figure 4.6A**). Eleven separate images were captured at each imaging location to improve the signal-to-noise ratio and minimize the effect of pulses from syringe pumps. ImageJ was utilized to determine greyscale intensities across the channel, orthogonal to fluid flow. Analysis of pixel intensity is a common method to quantify mixing on chip.[36-38] Similar to CFD simulations, CoV was again utilized as a function of channel position to determine the completeness of mixing:

$$CoV_y = \frac{\sqrt{\frac{\sum_{i=1}^{n}(I_i - \bar{I})^2}{N}}}{\bar{I}} \quad (\mathbf{4.2})$$

where I_i is the intensity of pixel i, $\bar{I}$ is the average intensity, and N is the total number of pixels analyzed. For this application a CoV of 0.05 or lower defines a well-mixed solution, which is generally accepted in most industrial applications of static mixers.[39]

Flow rate is an important factor that impacts mixing for SHM designs. Therefore, CoV data was gathered after different numbers of full-cycles for multiple flow rates between 0.2 and 4.0 mL min^{-1} on the short mixer (**Figure 4.5A**) and 1.0 and 13.0 mL min^{-1} on the long mixer (**Figure 4.5B**). See the materials and methods section for details on the experimental set-up and data analysis. The initial exponential decay of CoV displayed in **Figure 4.7A** and **B** is indicative of chaotic mixing and has been shown previously for microfluidic SHMs.[15] A CoV of less than 0.05 was achieved in ~100s of milliseconds for short and long millifluidic SHMs, which is comparable to previous microfluidic passive mixers.[10] CoV calculations after the last herringbone for short mixers (**Figure 4.7C**) and long mixers (**Figure 4.7D**) indicate CoV plateaus at roughly 0.03. A similar baseline near a CoV of 0.08 was noticed in previous work that quantified mixing in microfluidic SHMs using fluorescent molecules and confocal microscopy.[15] The plateau may be due to edge effects[15] caused by the different refractive indices of PMMA and water or other factors that lead to non-uniform intensity. Edge effects were minimized by ignoring ~20 μm of data on either side of the channel, but attempts to reduce potential sources of non-uniform intensity to analyze CoVs below 0.03 is unnecessary for most mixing applications considering a CoV of 0.05 is generally accepted as a well-mixed solution.[39]

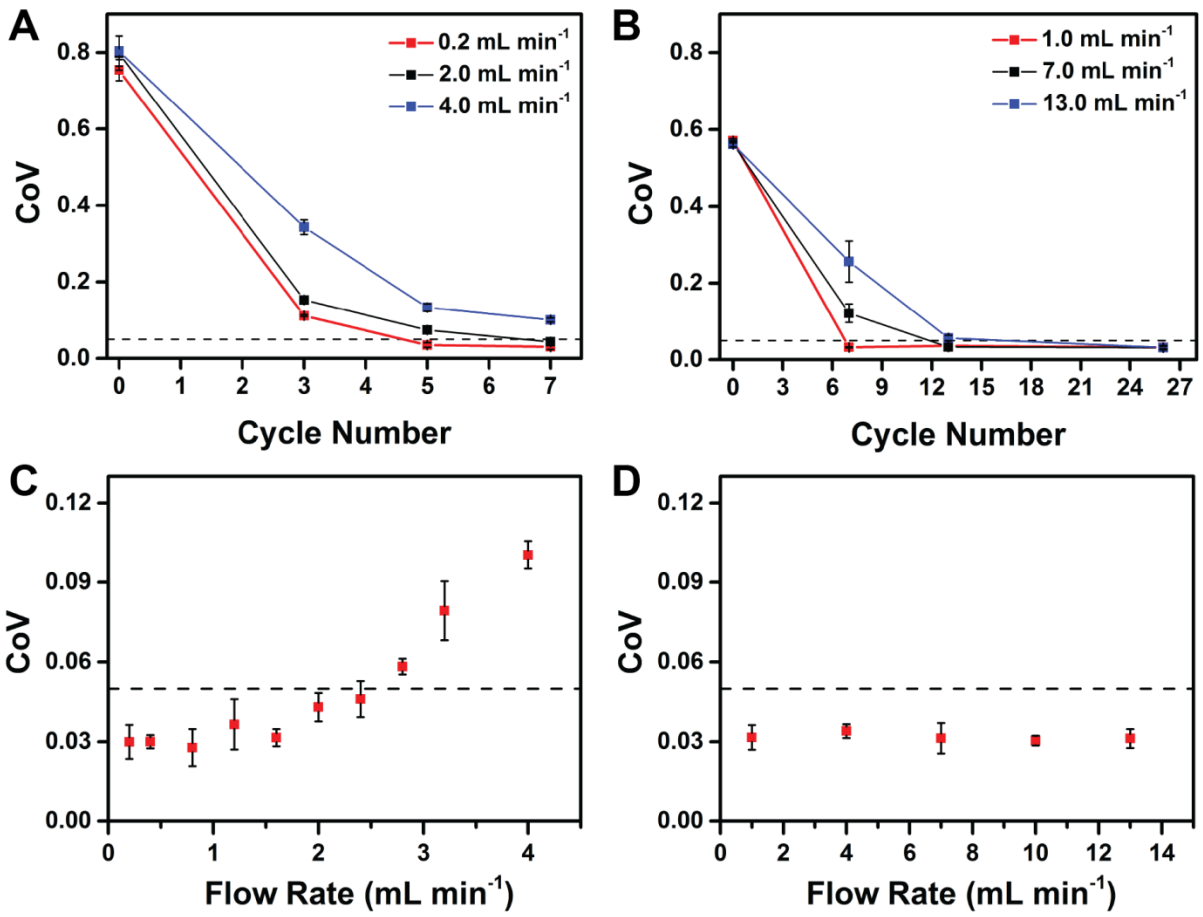

Figure 4.7. Graphs of CoV measured after a set number of full-cycles (6 HBs per full-cycle) at different total volumetric flow rates in the short mixer (A) or long mixer (B), and graphs of CoV calculated at different total volumetric flow rates after the last herringbone in the short mixer (C) or long mixer (D). The dashed line represents a CoV of 0.05, the criteria used to define a well-mixed solution. Note flow rates represent the total flow rate of both reagents.

Mixing in the z-direction is also important to characterize because the CoV data acquired from optical microscope images (**Figure 4.6A**) are cumulative values over the depth of the channel. Confocal microscopy has been utilized previously to analyze mixing in microfluidic SHMs and enables visualization of mixing in the z-direction.[14, 15] In this work a confocal microscope was also used to analyze mixing by injecting fluorescein dissolved in phosphate buffer in one inlet and phosphate buffer without fluorescein in the second inlet. Cross-sections of confocal images (**Figure 4.6B**) were utilized to qualitatively confirm mixing in the z-direction (see materials and methods section for specifics). Quantitative data was not determined primarily because the larger

channel size of the millifluidic SHMs relative to microfluidic dimensions required 1s to 10s of minutes to capture a single image. Not only is confocal microscopy prohibitively time-consuming and expensive to analyze multiple flow rates for millifluidic SHMs, but long scan times led to non-uniformities in the flow patterns likely due to pulses from syringe pumps. However, images of the cross-sections did qualitatively confirm solutions were well-mixed in the z-direction.

Application of millifluidic mixers for nanoparticle synthesis

Mixing is a key parameter for nanoparticle synthesis. Poor mixing during NP synthesis contributes to high polydispersity and poor batch-to-batch reproducibility.[19] Additionally, RTD can affect NP size and negatively impact size distribution.[40] Therefore, millifluidic SHMs are potentially useful for NP synthesis by (1) rapidly mixing reactants and (2) maintaining a narrow RTD. Previous work determined the reduction of gold and nucleation for AuNP synthesis can occur in less than 100 ms, and specifically noted these results would not have been possible without rapid mixing from a micromixer.[41] Prior work that utilized millifluidic mixers for NP synthesis consisted of platforms that mixed primarily by diffusion with slow mixing in the transversal direction[13, 42], utilized a turbulent jet mixer that required a specific flow regime[22], or made a mixer similar to a slanted groove mixer by pressing a Teflon tube with metallic jaws but still required turbulent flow to mix solutions properly[43]. Lohse et al. in particular noted the potential usefulness for simulation-guided mixer design for scaled-up nanoparticle synthesis schemes.[13]

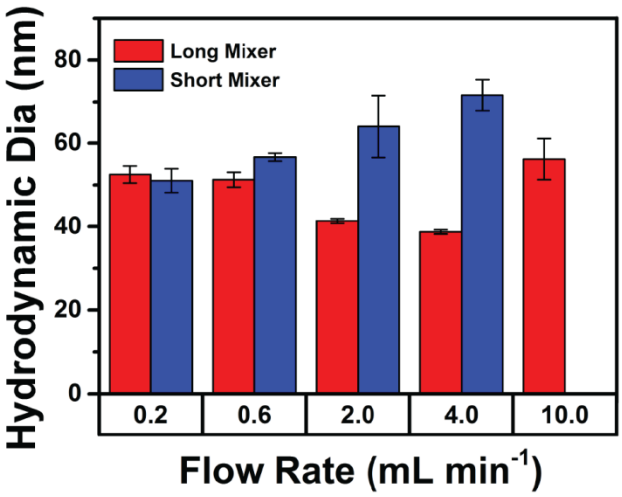

Figure 4.8. Hydrodynamic diameter of AuNPs from samples collected from short (blue bars) and long (red bars) mixers at different flow rates. Flow rates represent the total flow rate of both reagents. Results are displayed as the mean hydrodynamic diameter ± one standard deviation with n = 4.

The millifluidic SHMs were validated by synthesizing AuNPs. Ascorbic acid and chloroauric acid were injected in separate inlets of short mixers at the same flow rate and four samples were collected at each flow rate. Dynamic light scattering (DLS) results indicated AuNP size increased with increasing flow rate (**Figure 4.8**, blue bars), suggesting incomplete mixing and/or too short a residence time depending on the flow rate. For short mixers, a flow rate of 4.0 mL min^{-1} resulted in a CoV of ~0.10 measured after the last HB. However, the long mixer displayed complete mixing (CoV < 0.05) for flow rates up to 13.0 mL min^{-1} and also enables longer residence times in the mixer to reduce AuNP formation in the uncontrolled environment of the collection vials.

Therefore, the same AuNP synthesis experiment was performed utilizing long mixers, and AuNP size decreased with increasing flow rate up to 4.0 mL min^{-1} (**Figure 4.8**, red bars) demonstrating the importance of mixing and residence time on AuNP size. Additionally, batch-to-batch reproducibility improved, indicated by the small deviation in average AuNP size from multiple collections at the same flow rate. At a total flow rate of 10.0 mL min^{-1} AuNP size

increased similar to the short mixers, indicating device residence time was too short and AuNP formation likely continued in the collection vial. Therefore, a longer mixer may be required for higher flow rates simply to provide more residence time and not because mixing is incomplete. Additionally, the AuNP samples collected at flow rates of 0.2, 0.6, 2.0, or 4.0 mL min^{-1} from the long mixer had a polydispersity index (PDI) ranging from 0.18 to 0.26 (**Table 4.1**) which is comparable to similar sized gold nanoparticles from Sigma-Aldrich which have a specified PDI of less than or equal to 0.2.

All millifluidic SHMs utilized in this work displayed gold deposition on channel and HB walls. Gold deposition during AuNP synthesis was noted in multiple previous set-ups.[13, 42, 44] NP deposition on channel walls may be advantageous in some cases if the deposited NPs are useful as catalysts for continuous flow synthesis.[45] If NP deposition is undesirable, one of the advantages of using polymer-based millifluidic SHMs for NP synthesis is their low cost, and millifluidic SHMs can be discarded after generating the desired amount of NPs.[42] Another potential option to reduce deposition is to keep solution pH above 10, but pH also affects AuNP size so there is a tradeoff between desired AuNP size and amount of deposition.[43] Ultimately, despite gold deposition on the internal mixer features, the PMMA millifluidic SHMs were still capable of producing AuNPs with high batch-to-batch reproducibility and AuNP size could be controlled using different flow rates.

Table 4.1. Contains all the nanoparticle data used for **Figure 4.8**, and shows the PDI for each sample as well. A new short or long mixer was used for each flow rate and four gold nanoparticle samples were collected from each mixer.

Device	Flow Rate (mL min^{-1})	Sample Number	Hydrodynamic Diameter (nm)	PDI
Short Mixer	0.2	1	55.3	0.24
Short Mixer	0.2	2	50.3	0.23
Short Mixer	0.2	3	49.2	0.22
Short Mixer	0.2	4	49.4	0.22
Short Mixer	0.6	1	57.3	0.24
Short Mixer	0.6	2	56.0	0.25
Short Mixer	0.6	3	55.8	0.24
Short Mixer	0.6	4	57.7	0.23
Short Mixer	2	1	60.1	0.21
Short Mixer	2	2	61.8	0.21
Short Mixer	2	3	75.1	0.29
Short Mixer	2	4	59.2	0.20
Short Mixer	4	1	71.4	0.28
Short Mixer	4	2	73.0	0.28
Short Mixer	4	3	66.6	0.26
Short Mixer	4	4	75.4	0.29
Long Mixer	0.2	1	54.5	0.26
Long Mixer	0.2	2	51.2	0.23
Long Mixer	0.2	3	54.1	0.24
Long Mixer	0.2	4	50.4	0.22
Long Mixer	0.6	1	53.4	0.24
Long Mixer	0.6	2	52.1	0.23
Long Mixer	0.6	3	49.5	0.24
Long Mixer	0.6	4	50.2	0.22
Long Mixer	2	1	41.7	0.21
Long Mixer	2	2	40.8	0.21
Long Mixer	2	3	40.9	0.23
Long Mixer	2	4	42.0	0.21
Long Mixer	4	1	39.1	0.21
Long Mixer	4	2	38.8	0.19
Long Mixer	4	3	38.9	0.20
Long Mixer	4	4	38.0	0.18
Long Mixer	10	1	57.7	0.26
Long Mixer	10	2	59.6	0.26
Long Mixer	10	3	58.6	0.23
Long Mixer	10	4	48.9	0.23

4.3 Materials and methods

All solvents and chemical reagents were purchased from Thermo Fisher Scientific, Sigma-Aldrich, or Avantor and were used as received unless otherwise specified. Water was purified in-house using a Barnstead E-Pure filtration system.

CFD Simulations

All CFD simulations were completed on a Dell Precision T3500 workstation (Dell Inc.) with 24 GB of RAM using COMSOL Multiphysics 5.1 (COMSOL Inc.). Two different types of simulations were performed. The first set of CFD simulations optimized groove width and groove depth using one herringbone while a second set of simulations optimized distance between grooves using two, or in one simulation three, HBs.

CFD simulations used the laminar flow and transport of diluted species interfaces to solve Navier-Stokes (NS) equations for incompressible flow and convection-diffusion (CD) equation at steady-state. NS and CD equations were coupled for simulations. The density and viscosity of the fluid were set to those of water at 20 °C. The material poly(methyl methacrylate) was selected for all boundaries, except the inlets and outlet, because PMMA was used for all fabricated millifluidic SHMs.

The channel in all simulations was set to 800 μm wide by 200 μm tall with a 300 μm entry length with respect to the apex of the first HB. Channel length was 2000 μm for one HB simulations and 3600 μm for two and three HB simulations. For single HB simulations both groove width and groove depth were varied from 200 μm to 800 μm with a 100 μm step size, and all 49 combinations were simulated. For two HB simulations groove width was 600 μm and groove depth was 500 μm while the distance between grooves was varied from 200 μm to 1000 μm with a 100 μm step size. The single three HB simulation used the same parameters as the two

HB simulations except one additional HB was added and the distance between all grooves was 200 μm.

The boundary conditions and diffusion coefficient ($D = 10^{-9}$ m^2 s^{-1}) were similar to previous work.[23] The channel entry was split into equal halves for two inlets. Both inlet flows were set to 0.01 m s^{-1}, similar to the velocity of the lower flow rates tested on the fabricated millifluidic SHMs. The outlet boundary condition was set to 0 Pa. The solute concentration of one inlet was 1 mol m^{-3} and the other inlet was 0 mol m^{-3}. No slip and no flux boundary conditions were set at all other boundaries besides the inlets and outlet.

Three-dimensional CFD simulations are computationally demanding, especially considering the increased size of the channel and herringbones relative to microfluidic SHMs. Therefore the meshing was slightly coarser than meshes previously used for microfluidic SHMs[15, 23, 28] to reduce computational power and time. A free tetrahedral mesh was used for both the channel and herringbones. Meshing size parameters were 30 μm for the maximum element size, 5 μm for the minimum element size, 1.3 for the maximum element growth rate, 0.2 for curvature factor, and 0.7 for the resolution of narrow regions for the channel and the settings for the herringbones were 10 μm, 5 μm, 1.3, 0.2, and 0.85, respectively for a finer mesh relative to the channel. Total mesh elements ranged from 7×10^5 to 9×10^6 for single HB simulations, 8×10^6 for two HB simulations, and 1×10^7 for the three HB simulation.

Additionally, to decrease computation time laminar flow was discretized using the default COMSOL setting (P1 + P1), and similarly the transport of diluted species utilized the default linear discretization. Due to the discretization scheme and to avoid potential convergence issues, consistent stabilization (streamline and crosswind diffusion) was utilized, but not inconsistent stabilization. Higher order discretization schemes may improve accuracy of simulations, but

come at the cost of computation time and power. In this chapter only low Peclet number flows were simulated and the mesh used was as fine as possible while still able to complete simulations in a timely manner. Streamline and particle tracing are other potential simulation methods to determine extent of mixing, but ignore the problem of diffusion.[15] CFD simulations were used to guide SHM design, but extent of mixing was also experimentally determined. All calculations and images from CFD simulations were obtained using tools available in COMSOL.

Millifluidic SHM fabrication

Two different millifluidic designs were fabricated, a mixer with 42 HBs (**Figure 4.4A**) and a mixer with 156 HBs (**Figure 4.4B**) referred to as a "short mixer" and "long mixer" respectively. All SHM designs were fabricated in 3 mm thick PMMA sheets (Astari Niagra International) using a conventional CNC milling machine. A 0.010" diameter end mill was used for milling all channels and a 0.014" diameter end mill was utilized for fabricating all herringbones. Fabricated HB dimensions were the same for all SHMs (**Figure 4.4C**). Through holes for inlets and outlets were drilled with a 1.20 mm drill bit. The edges around the drilled holes were sanded to remove burrs that may impact PMMA bonding, and the PMMA was rinsed with water.

All millifluidic mixers, except mixers used for confocal microscopy, used a blank 3 mm thick piece of PMMA with no milled features as the bottom substrate. The blank was cut slightly larger than the PMMA sheet with the milled SHM design. Both blank and milled PMMA sheets were scrubbed with an aqueous Alconox solution, rinsed with water, rinsed with isopropanol, and finally dried with a stream of nitrogen. Both PMMA sheets were placed in a plasma cleaner (Harrick Scientific, model PDC-001) for 2 min at 500 mTorr to reduce bonding temperature and improve bonding strength.[46] The sheets were then quickly combined into the following assembly in order from bottom to top: (1) an aluminum block, (2) a sheet of polydimethylsiloxane

(PDMS), (3) the blank PMMA sheet, (4) the PMMA piece with milled features, (5) a second PDMS sheet, and (6) an aluminum block. The entire assembly was placed in a hot press (Carver, Model 3851) preheated to 95 °C. A pressure of 2900 kPa was applied for 40 min at 95 °C. The hot press was shut off and allowed to cool for 3 h before removing the PMMA device.

Placement of PDMS sheets, a deformable polymer, on either side of the PMMA pieces improved bonding by evenly applying force to the PMMA sheets. Without PDMS present sections of PMMA did not bond. The PDMS sheets (~15 x 15 cm) were fabricated by pouring a degassed 10:1 mixture (base/curing agent) of Sylgard 184 PDMS (Dow Corning) on top of 2 clean glass plates with walls made from tape to contain the PDMS. The PDMS was cured overnight in a 65 °C oven and removed from the glass plates.

After bonding, the PMMA surface near the inlets and outlet was cleaned with isopropanol. Then NanoPorts (IDEX, 10-32 coned assemblies for 1/16" OD tubing) with gaskets underneath were lined up with each inlet or outlet. The NanoPorts were held in place using a binder clip and a 2-part Loctite epoxy was applied around the edges of the NanoPorts. The epoxy cured overnight and then the binder clips were removed.

The device used for confocal microscopy was a short mixer, and was fabricated in an almost identical fashion except a 0.175 mm thick piece of PMMA (Goodfellow) was used for the bottom substrate. Additionally, a thin sheet (~0.5 mm) of titanium was inserted between the bottom sheet of PDMS and the thin sheet of PMMA to prevent the PDMS from pushing the thin PMMA sheet upwards, causing channel collapse.

General method for injecting solutions into millifluidic SHMs

All millifluidic SHM devices had NanoPorts glued to both inlets and the outlet for attachment of 20 gauge PTFE tubing (Cole-Parmer or AlphaWire) to enable fluid injection and collection.

All solutions were loaded into plastic (Becton, Dickinson and Company) or glass (Hamilton Company) syringes and connected to the 20 gauge tubing via 20 gauge syringe needles (Becton, Dickinson and Company or Hamilton Company). Syringes were placed in milliliter syringe pump modules or a PHD 2000 syringe pump (Harvard Apparatus) to control the flow rate of injected fluids. Prior to injecting the desired solutions for mixing analysis or nanoparticle synthesis, isopropanol then water were injected into the millifluidic mixers to remove any air pockets. Air pockets may also be removed with high flow rates of water (~20 mL min^{-1}), obviating the need for changing the input from isopropanol to water.

Quantifying the extent of mixing – optical microscope

A solution of 0.5 mM Fast Green FCF and 2.0 mM Amaranth were prepared in 1x phosphate buffered saline from Corning. Fast Green and Amaranth were chosen based on previous work that determined these two dyes were useful for characterizing and quantifying microfluidic systems with red-green-blue (RGB) cameras.[35] PBS was used to dissolve the dyes to ensure there wasn't a mismatch in pH or ionic strength between the two different dye solutions.[35] Prepared dye solutions were stored in the fridge (4 °C) in amber glass jars up to 3 months and removed approximately 6 to 24 hours before experiments to allow solutions to warm to room temperature. Solutions of 0.5 mM Fast Green and 2.0 mM Amaranth were injected at equal flow rates into millifluidic SHMs placed on top of a microscope (Leica M205 C) stage and 11 images were captured using a RGB camera (Leica DFC295) at five different positions along the length of the mixer. During image capture ambient light was reduced by turning off lights and surrounding the microscope area with a thick curtain. After capturing all required images, the flow rate was changed and the image acquisition process was repeated. Devices were cleaned by injecting

isopropanol, then water, and finally air. The entire process of fluid injection and image capture was repeated on three separate days for n=3 trials on all graphs in **Figure 4.7**.

Each combination of light source, microscope, color camera, and dye solution produces a different spectral response and requires checking the concentration range where the response is linear.[35] Therefore, prior to collecting data on the optical microscope to quantify the extent of mixing, microscope settings (e.g., zoom, exposure time, gain, saturation, gamma) were optimized and linearity of the Fast Green FCF and Amaranth dye solutions checked. 8-bit greyscale images were used for image analysis so microscope settings were optimized to ensure good separation in greyscale intensity between the two dyes without either dye reaching a maxima or minima (i.e., 0 or 255 for 8-bit greyscale images). Linearity of the dyes at all concentrations was confirmed by mixing stock solutions of 0.5 mM Fast Green and 2.0 mM Amaranth in different concentrations from 100 v/v% Fast Green to 100 v/v% Amaranth and injecting the premixed solutions into a millifluidic SHM (**Figure 4.9**).

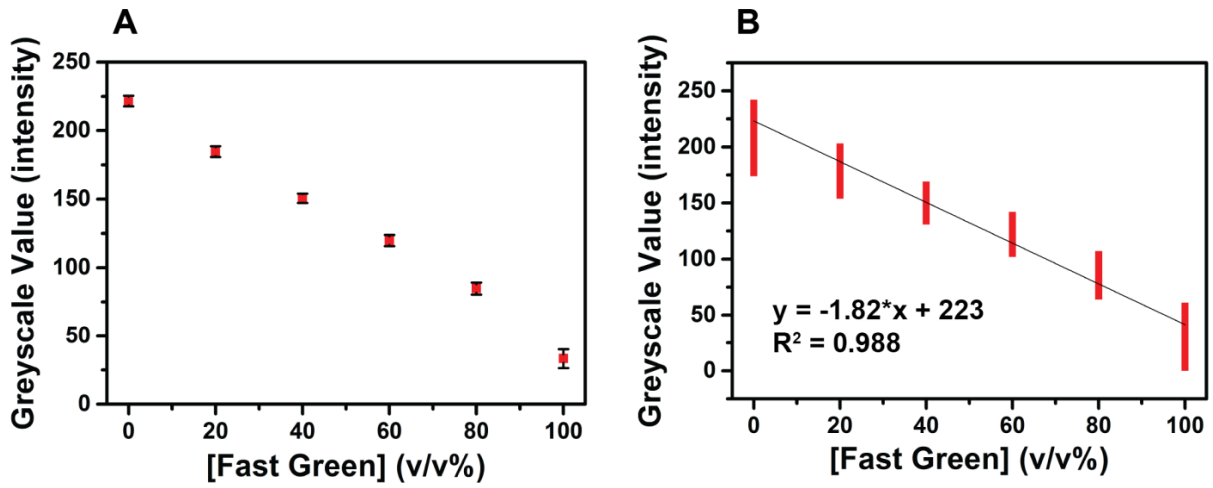

Figure 4.9. Graphs without (A) and with (B) linear regression model displaying the linear relationship between the greyscale intensity and dye concentration. Data is expressed as the mean ± standard deviation (A) or all data points are displayed (B). Both graphs are displayed to show the small standard deviation in greyscale intensity (A) and to accurately calculate a simple linear regression model (OriginPro 2016 v93E) with all data points used (B).

Captured images were analyzed by ImageJ (v1.48v, National Institutes of Health) to quantitatively determine the extent of mixing. Images were split into 8-bit red, green, and blue channels, and the red channel was saved for processing. A line was drawn across the channel, orthogonal to the fluid flow, and a single column of intensity values was gathered from the line for each red channel image, ignoring ~20 μm of data on either side of the channel to avoid edge affects. Lines were drawn in between half-cycles to ensure no collected data came from a herringbone feature (**Figure 4.10**). The coefficient of variation (CoV) was calculated (**Equation 4.2**) at each position imaged (11 images per position) using Microsoft Excel (Microsoft Corporation). The same number of data points was used for each CoV calculation. Home-written scripts (ImageJ) and macros (Excel) were used to accelerate image processing and analysis.

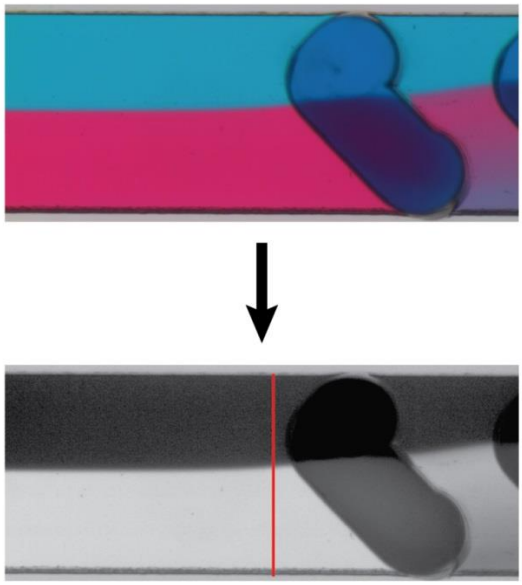

Figure 4.10. Schematic to demonstrate how greyscale intensity data was collected from optical microscope images. The raw optical microscope images were split into 8-bit red, green, and blue channels, and the red channel was preserved for analysis. A line was drawn across the channel (red line in image), perpendicular to fluid flow, to determine the greyscale intensity values in ImageJ. Further data processing was performed in Excel to remove data from ~20 μm on either side of the channel to avoid edge effects and calculate the CoV.

Characterizing the extent of mixing – confocal microscope

A 50 mM potassium phosphate buffer solution was prepared and the pH was adjusted to 8.00. A stock solution of 50 mM fluorescein was prepared in dimethyl sulfoxide. A 500 μM solution of fluorescein was created by diluting 50 mM fluorescein stock solution in 50 mM phosphate buffer, pH 8.00. 500 μM fluorescein and 50 mM phosphate buffer were injected into different inlets of a millifluidic SHM at a flow rate of 100 μL min^{-1} for each fluid (200 μL min^{-1} total flow rate). Z-stack images were captured using a LSM 700 confocal microscope (Carl Zeiss Inc.) with a 20x/0.8 Plan-Apochromat objective and a 488 nm laser. A tile scan with 2 tiles was necessary to capture the full width of the channel so the final dimensions of the z-stack images were approximately 1132 μm (x) x 566 μm (y) x 210 μm (z). Slices from the confocal images representing the xz-plane were obtained using Imaris x64 software (v8.1.2, Bitplane).

Gold nanoparticle synthesis and characterization

A 6 mM ascorbic acid solution and a 0.375 mM chloroauric acid solution were prepared in water immediately prior to nanoparticle synthesis experiments. Ascorbic acid and chloroauric acid were injected into separate inlets at equal flow rates. A new millifluidic SHM was used for each flow rate. Four separate 4 mL samples were collected at each flow rate, waiting 30 s before collecting the first sample and waiting 1 min between each subsequent collection. A Malvern Zetasizer Nano-ZS (Malvern Instruments) was used to determine the hydrodynamic diameter of gold nanoparticles using DLS. The mean hydrodynamic diameter and standard deviation were determined using the 4 separate samples collected at each flow rate.

4.4 Conclusions

Millifluidic platforms have similar advantages to their microfluidic counterparts, including rapid heat and mass transfer, but use of millifluidics enables higher throughput and millifluidic

platforms are simpler to fabricate and operate than their microfluidic equivalents. One crucial step in many applications is mixing, which has been well characterized for the microfluidic scale but not for the millifluidic scale. CFD simulations were used to identify the dimensions (groove width, groove depth, and distance between grooves) that optimize the mixing performance of a millifluidic staggered herringbone mixer. Based on insights from the CFD simulations, a short millifluidic mixer was fabricated and quantitatively characterized, and results indicated the mixer was able to rapidly and effectively mix (CoV < 0.05) fluids up to a total flow rate of ~2.0 mL min^{-1}. A similar long mixer with more HBs was able to successfully mix solutions at flow rates of 13.0 mL min^{-1}.

One potential use of the millifluidic SHM design was validated by synthesizing AuNPs. The short mixer displayed larger AuNP size with increasing flow rate and poorer batch-to-batch reproducibility likely from a combination of incomplete mixing and short residence time. However, the long mixer design demonstrated (1) improved batch-to-batch reproducibility compared to the short mixer, (2) size control by adjusting total flow rate, and (3) PDIs similar to commercially available AuNPs. In summary, the millifluidic SHM design discussed in Chapter 4 is an inexpensive, easily manufactured platform that can be used to rapidly mix solutions for NP synthesis and potentially other applications including pharmaceutical production, enzymatic reactions, and improving chemical selectivity of reactions.

4.5 References

(1) Pascali, G., Watts, P., and Salvadori, P. A. (2013) Microfluidics in radiopharmaceutical chemistry. *Nucl. Med. Biol. 40*, 776-787.

(2) Tran, T.-T., Nguyen, M.-H., Tan, Y. Z., Chew, J. W., Khan, S. A., and Hadinoto, K. (2017) Millifluidic synthesis of amorphous drug-polysaccharide nanoparticle complex with tunable size intended for supersaturating drug delivery applications. *Eur. J. Pharm. Biopharm. 112*, 196-203.

(3) Kang, L., Chung, B. G., Langer, R., and Khademhosseini, A. (2008) Microfluidics for drug discovery and development: From target selection to product lifecycle management. *Drug Discov. Today 13*, 1-13.
(4) Yao, X., Zhang, Y., Du, L., Liu, J., and Yao, J. (2015) Review of the applications of microreactors. *Renew. Sust. Energ. Rev. 47*, 519-539.
(5) Shahbazali, E., Hessel, Volker, Noël, Timothy, Wang, Qi. (2016) Metallic nanoparticles made in flow and their catalytic applications in micro-flow reactors for organic synthesis. *Physical Sciences Reviews 1*.
(6) Mason, B. P., Price, K. E., Steinbacher, J. L., Bogdan, A. R., and McQuade, D. T. (2007) Greener Approaches to Organic Synthesis Using Microreactor Technology. *Chem. Rev. 107*, 2300-2318.
(7) Agostino, F. J., and Krylov, S. N. (2015) Advances in steady-state continuous-flow purification by small-scale free-flow electrophoresis. *TrAC, Trends Anal. Chem. 72*, 68-79.
(8) Hartman, R. L., and Jensen, K. F. (2009) Microchemical systems for continuous-flow synthesis. *Lab Chip 9*, 2495-2507.
(9) Elvira, K. S., i Solvas, X. C., Wootton, R. C. R., and deMello, A. J. (2013) The past, present and potential for microfluidic reactor technology in chemical synthesis. *Nat. Chem. 5*, 905-915.
(10) Lee, C.-Y., Chang, C.-L., Wang, Y.-N., and Fu, L.-M. (2011) Microfluidic Mixing: A Review. *Int. J. Mol. Sci. 12*, 3263-3287.
(11) Lee, C.-Y., Wang, W.-T., Liu, C.-C., and Fu, L.-M. (2016) Passive mixers in microfluidic systems: A review. *Chem. Eng. J. 288*, 146-160.
(12) Woldemariam, M., Filimonov, R., Purtonen, T., Sorvari, J., Koiranen, T., and Eskelinen, H. (2016) Mixing performance evaluation of additive manufactured milli-scale reactors. *Chem. Eng. Sci. 152*, 26-34.
(13) Lohse, S. E., Eller, J. R., Sivapalan, S. T., Plews, M. R., and Murphy, C. J. (2013) A Simple Millifluidic Benchtop Reactor System for the High-Throughput Synthesis and Functionalization of Gold Nanoparticles with Different Sizes and Shapes. *ACS Nano 7*, 4135-4150.
(14) Stroock, A. D., Dertinger, S. K. W., Ajdari, A., Mezic, I., Stone, H. A., and Whitesides, G. M. (2002) Chaotic Mixer for Microchannels. *Science 295*, 647-651.
(15) Williams, M. S., Longmuir, K. J., and Yager, P. (2008) A practical guide to the staggered herringbone mixer. *Lab Chip 8*, 1121-1129.
(16) Land, K. J., Mbanjwa, M., and Korvink, J. G. (2014) Microfluidic channel structures speed up mixing of multiple emulsions by a factor of ten. *Biomicrofluidics 8*, 054101.
(17) Aubin, J., Fletcher, D. F., and Xuereb, C. (2005) Design of micromixers using CFD modelling. *Chem. Eng. Sci. 60*, 2503-2516.
(18) Cantu-Perez, A., Barrass, S., and Gavriilidis, A. (2011) Hydrodynamics and reaction studies in a layered herringbone channel. *Chem. Eng. J. 167*, 657-665.
(19) Rahman, M., and Rebrov, E. (2014) Microreactors for Gold Nanoparticles Synthesis: From Faraday to Flow. *Processes 2*, 466.
(20) Xu, Z., Lu, C., Riordon, J., Sinton, D., and Moffitt, M. G. (2016) Microfluidic Manufacturing of Polymeric Nanoparticles: Comparing Flow Control of Multiscale Structure in Single-Phase Staggered Herringbone and Two-Phase Reactors. *Langmuir 32*, 12781-12789.

(21) Zhao, C.-X., He, L., Qiao, S. Z., and Middelberg, A. P. J. (2011) Nanoparticle synthesis in microreactors. *Chem. Eng. Sci. 66*, 1463-1479.
(22) Lim, J.-M., Swami, A., Gilson, L. M., Chopra, S., Choi, S., Wu, J., Langer, R., Karnik, R., and Farokhzad, O. C. (2014) Ultra-High Throughput Synthesis of Nanoparticles with Homogeneous Size Distribution Using a Coaxial Turbulent Jet Mixer. *ACS Nano 8*, 6056-6065.
(23) Sabotin, I., Tristo, G., Junkar, M., and Valentincic, J. (2013) Two-step design protocol for patterned groove micromixers. *Chem. Eng. Res. Des. 91*, 778-788.
(24) Cortes-Quiroz, C. A., Azarbadegan, A., Zangeneh, M., and Goto, A. (2010) Analysis and multi-criteria design optimization of geometric characteristics of grooved micromixer. *Chem. Eng. J. 160*, 852-864.
(25) Ansari, M. A., and Kim, K.-Y. (2007) Application of the radial basis neural network to optimization of a micromixer. *Chem. Eng. Technol. 30*, 962-966.
(26) Afzal, A., and Kim, K.-Y. (2014) Three-objective optimization of a staggered herringbone micromixer. *Sensor Actuat. B-Chem. 192*, 350-360.
(27) Ansari, M. A., and Kim, K. Y. (2007) Application of the radial basis neural network to optimization of a micromixer. *Chem. Eng. Technol. 30*, 962-966.
(28) Du, Y., Zhang, Z., Yim, C., Lin, M., and Cao, X. (2010) A simplified design of the staggered herringbone micromixer for practical applications. *Biomicrofluidics 4*.
(29) Lynn, N. S., and Dandy, D. S. (2007) Geometrical optimization of helical flow in grooved micromixers. *Lab Chip 7*, 580-7.
(30) Hassell, D. G., and Zimmerman, W. B. (2006) Investigation of the convective motion through a staggered herringbone micromixer at low Reynolds number flow. *Chem. Eng. Sci. 61*, 2977-2985.
(31) Kang, T. G., and Kwon, T. H. (2004) Colored particle tracking method for mixing anlysis of chaotic micromixers. *J. Micromech. Microeng. 14*, 891-899.
(32) Kukuková, A., Noël, B., Kresta, S. M., and Aubin, J. (2008) Impact of sampling method and scale on the measurement of mixing and the coefficient of variance. *AlChE J. 54*, 3068-3083.
(33) Subramanian, B., Kim, N., Lee, W., Spivak, D. A., Nikitopoulos, D. E., McCarley, R. L., and Soper, S. A. (2011) Surface Modification of Droplet Polymeric Microfluidic Devices for the Stable and Continuous Generation of Aqueous Droplets. *Langmuir 27*, 7949-7957.
(34) Aubin, J., Ferrando, M., and Jiricny, V. (2010) Current methods for characterising mixing and flow in microchannels. *Chem. Eng. Sci. 65*, 2065-2093.
(35) Werts, M. H. V., Raimbault, V., Texier-Picard, R., Poizat, R., Francais, O., Griscom, L., and Navarro, J. R. G. (2012) Quantitative full-colour transmitted light microscopy and dyes for concentration mapping and measurement of diffusion coefficients in microfluidic architectures. *Lab Chip 12*, 808-820.
(36) Mao, X. L., Juluri, B. K., Lapsley, M. I., Stratton, Z. S., and Huang, T. J. (2010) Milliseconds microfluidic chaotic bubble mixer. *Microfluid. Nanofluid. 8*, 139-144.
(37) Venancio-Marques, A., Barbaud, F., and Baigl, D. (2013) Microfluidic Mixing Triggered by an External LED Illumination. *J. Am. Chem. Soc. 135*, 3218-3223.
(38) Lee, J. H., Lee, K. H., Won, J. M., Rhee, K., and Chung, S. K. (2012) Mobile oscillating bubble actuated by AC-electrowetting-on-dielectric (EWOD) for microfluidic mixing enhancement. *Sensor Actuat. A-Phys. 182*, 153-162.

(39) III, A. W. E., and Meyer, C. F. (2004) Mixing in Pipelines, in *Handbook of Industrial Mixing: Science and Practice* (Paul, E. L., Atiemo-Obeng, V. A., and Kresta, S. M., Eds.) pp 391-477, John Wiley & Sons, Inc.
(40) Li, Y. H., Sanampudi, A., Reddy, V. R., Biswas, S., Nandakumar, K., Yemane, D., Goettert, J., and Kumar, C. S. S. R. (2012) Size Evolution of Gold Nanoparticles in a Millifluidic Reactor. *ChemPhysChem 13*, 177-182.
(41) Thanh, N. T. K., Maclean, N., and Mahiddine, S. (2014) Mechanisms of Nucleation and Growth of Nanoparticles in Solution. *Chem. Rev. 114*, 7610-7630.
(42) Li, Y., Sanampudi, A., Raji Reddy, V., Biswas, S., Nandakumar, K., Yemane, D., Goettert, J., and Kumar, C. S. S. R. (2012) Size Evolution of Gold Nanoparticles in a Millifluidic Reactor. *ChemPhysChem 13*, 177-182.
(43) Jun, H., Fabienne, T., Florent, M., Coulon, P. E., Nicolas, M., and Olivier, S. (2012) Understanding of the size control of biocompatible gold nanoparticles in millifluidic channels. *Langmuir 28*, 15966-74.
(44) Jun, H., Fabienne, T., Florent, M., Coulon, P.-E., Nicolas, M., and Olivier, S. (2012) Understanding of the Size Control of Biocompatible Gold Nanoparticles in Millifluidic Channels. *Langmuir 28*, 15966-15974.
(45) Navin, C. V., Krishna, K. S., Bovenkamp-Langlois, G. L., Miller, J. T., Chattopadhyay, S., Shibata, T., Losovyj, Y., Singh, V., Theegala, C., and Kumar, C. S. S. R. (2015) Investigation of the synthesis and characterization of platinum-DMSA nanoparticles using millifluidic chip reactor. *Chem. Eng. J. 281*, 81-86.
(46) Tsao, C. W., and DeVoe, D. L. (2009) Bonding of thermoplastic polymer microfluidics. *Microfluid. Nanofluid. 6*, 1-16.

Chapter 5

Concluding remarks

5.1 Summary

Molecular imaging has the potential to improve the understanding of biochemical processes and assist with clinical diagnoses and disease treatment. The molecular imaging technique positron emission tomography (PET) in particular has grown substantially in the field of clinical oncology since the 1990s.[1] The most widely used PET radiotracer is [^{18}F]fluorodeoxyglucose ([^{18}F]FDG)[2], but despite the widespread use of [^{18}F]FDG the probe has multiple shortcomings including a lack of sensitivity for specific tumors, and the radioisotope ^{18}F has a short half-life. There is a strong desire to further the development and production of other PET radiotracers, specifically radiotracers that utilize radiometals because radiometal-based radiotracers offer flexibility, modularity, and simplicity.[3]

In my dissertation I first described how microfluidic platforms and "click chemistry" can be used to improve synthesis of radiometal-based PET radiotracers. Typically, PET radiotracers are produced in large batches (approximately a few milliliters) and then shipped to the imaging location. While this centralized production approach may be cost effective, the method is not conducive to personalized medicine. Recently, there has been a rise in the interest of producing the most suitable PET radiotracer (personalized medicine), on-site (decentralized production), when needed (dose-on-demand), to enable more individualized treatment of patients.[4] The continued development of microfluidic platforms for radiotracer synthesis is essential to the development of the decentralized, dose-on-demand production approach. Reducing reactor size

not only decreases the use of expensive reagents, but also minimizes radiation shielding size and cost.[5, 6]

The goal of personalized medicine is to further divide one general population of patients into smaller strata to improve diagnosis and treatment while minimizing side effects. Molecular imaging agents, especially PET radiotracers, can non-invasively image tumors without disrupting the body's biochemistry or physiology and assist with determining which patients will respond to specific treatments. However, cancer is heterogeneous in nature and a multitude of molecular targets exist for molecular probe development including integrins, vascular endothelial growth factor (VEGF), and cyclooxygenase (COX)-2.[7] The wide range of targets requires an equally large number of specific biomolecules for incorporation into PET radiotracers. Improving the synthesis of tumor-specific radiotracers and molecular imaging agents in general is necessary for the continued growth of personalized medicine. For example, more than 1,400 ^{18}F-based tracers have been developed for research applications, but few are commercially available due to high capital and operating costs and short radiotracer half-life.[6]

The "click chip" was designed to address the challenge of producing multiple radiotracers with different biomolecules using one chemistry to simplify the synthesis process. "Click chemistry", specifically Cu(I)-catalyzed azide-alkyne cycloaddition (CuAAC), enables site-specific attachment of bifunctional chelators (BFCs) to the tumor-targeting biomolecules (BMs) under mild reaction conditions unlikely to denature biomolecules (e.g., proteins[8]). The fabricated "click chip" leverages the advantages of microfluidics and CuAAC to improve the BFC and BM conjugation process while also reducing purification requirements by immobilizing the cytotoxic Cu(I) catalyst, minimizing or obviating the need to remove Cu(I). I demonstrated the ability to synthesize three different BM-BFC conjugates with minimal Cu(I) leaching (~1 μg) into the

product solution. Furthermore, many CuAAC biomolecule and bifunctional chelator conjugation reaction conditions require long incubation times[9] or high temperatures (~80-100 °C) and microwave irradiation[10]. Here, I demonstrated the ability to synthesize a peptide and BFC conjugate at 47 °C in high yields (~80% – 100%) after 1-6 hours.

Nanoparticles are also useful as molecular imaging agents with the potential to easily incorporate multiple modalities (e.g., theranostics[11]). Many nanoparticles (NPs) have been created for medical imaging purposes including gold NPs[12, 13], quantum dots[14], and Fe_3O_4 NPs[15]. However, NPs are currently synthesized using batch synthetic strategies that are not easily scaled up.[16-18] Lohse et al. addressed this issue by creating a simple millifluidic reactor to produce gold nanoparticles (AuNPs) in a high throughput fashion, but specifically mentioned the current design was a "version 1.0" model and one potential improvement would be to incorporate new mixer designs.[16] Rapid mixing is critical for NP synthesis because poor mixing contributes to high polydispersity and poor batch-to-batch reproducibility.[19]

In addition to the development of a "click chip", in this dissertation I describe the development of a millifluidic staggered herringbone mixer (SHM) to improve the throughput of nanoparticle synthesis. While microfluidic platforms have been utilized previously to synthesize nanoparticles with high monodispersity[19], production of nanoparticles using millifluidics is still relatively new. Therefore, computational fluid dynamics (CFD) simulations were utilized to optimize the mixer design which was then fabricated by milling the features in sheets of poly(methyl methacrylate) (PMMA). Optical and confocal microscopy both confirmed the fabricated mixer was able to effectively mix aqueous solutions, and the millifluidic platform was validated by synthesizing AuNPs.

Overall my dissertation focused on the development of micro- and millifluidic platforms to improve the synthesis of imaging agents. In Chapter 2 I described how a new water-soluble Cu(I) ligand was covalently attached to the walls of a microfluidic platform to enable immobilization and stabilization of Cu(I) to reduce purification requirements of "click" reactions. The fabricated "click chip" was validated by conjugating a dye with a small molecule and peptide. Chapter 3 discussed how the "click chip" was improved by reducing the polydimethylsiloxane (PDMS) thickness and bonding a thin sheet of cyclic olefin copolymer (COC) to reduce solvent loss and enable longer reactions on chip. Three different BM-BFC conjugates were synthesized on the thin "click chip" to demonstrate the potential of the thin "click chip" for producing radiometal-based PET radiotracers. In Chapter 4, I described the development of a millifluidic SHM for reactions that require rapid mixing, such as NP synthesis. The millifluidic SHM was validated by synthesizing AuNPs.

5.2 Future directions

The developed "click chip" was successfully utilized to produce three separate BM-BFC conjugates with miniscule amounts of Cu(I) catalyst in the product solution. While two different BMs (a peptide and a nucleoside) were utilized for these conjugation reactions further work can demonstrate the utility of the "click chip" to synthesize other BM and BFC conjugates including antibody conjugates[8] using one chemistry to simplify radiotracer production. Additionally, by using a microfluidic platform the consumption of expensive of reagents and radiation shielding costs may be reduced; improving the availability of a "click chip" system for the decentralized production of radiotracers with dose-on-demand capabilities.

One "click chip" conjugation reaction created a product in relatively low yields (~65%) after 12 h indicating some reaction conditions may need to be further optimized. The same ratio of

reagents (1:1.5 BFC / BM) was used for all reactions to validate the "click chip", but reagent ratios could be adjusted to improve yields with reduced reaction time. Additionally, only one Cu(I) ligand was utilized for "click chips". Cu(I) ligands can impact reaction rates[8], and testing the "click chip" concept with different Cu(I) ligands may improve reaction rates as well.

Additionally, further work can focus on the loss of *tert*-butyl (tBu) protecting groups from BFCs. As mentioned in Chapter 3, tBu groups were removed from BFCs during "click reactions" and also when incubated with metal ions. The extent of tBu loss depended on the metal ion and the BFC. Further work examining the tBu loss phenomena could provide insights on improving the harsh reaction conditions (e.g., strong acids) typically required for de-*tert*-butylation. Evans et al. also recently noticed how a simple copper salt could be used to remove tBu groups from amides under mild conditions.[20] Furthermore, the loss of tBu groups indicates that a chelate then "click" strategy as opposed to a "click" then chelate strategy may be most effective when using the "click chip" for PET radiotracer synthesis, and further work can validate this premise.

With regards to the millifluidic SHM for NP production, only AuNPs have been produced using the mixer. These nanoparticles were only analyzed using dynamic light scattering (DLS) and further characterization (e.g., transmission electron microscopy) can confirm the size distribution of the synthesized nanoparticles. Future work could determine the utility of the mixer for synthesizing other nanoparticles including micelles and polymersomes. A commercially available microfluidic SHM has been utilized previously to synthesize polymeric nanoparticles but the throughput was low (10s – 100s μL/min).[21] A millifluidic turbulent jet mixer has also been utilized to synthesize lipid and polymer NPs[22], but requires achieving a specific flow regime to achieve rapid mixing which may be difficult when changing solvents and/or solutes. Further work studying the synthesis of polymer and lipid vesicle formation using

the millifluidic SHM described in my dissertation could demonstrate the potential to create imaging agent and therapeutic NPs at a greater throughput (1s – 10s mL/min) relative to microfluidic platforms.

Another potential future research avenue is to further analyze the millifluidic mixer design. Microfluidic mixers have been well-studied the last decades, but little work has focused on the mixing performance of millifluidic mixers.[23] Here we only identified a local optimum by tuning three different parameters, herringbone width and depth and the distance between herringbones. Identifying a true optimum is computationally intensive and difficult due to the non-linear nature of the mixing problem[24], and also because of the number of factors involved and potential criterion to optimize. Further computational and experimental work expanding the design space to include other factors such as the channel height and width and the number of grooves per half-cycle could further improve the millifluidic SHM mixing effectiveness. Additionally, other mixer designs analyzed at the microfluidic scale (e.g., slanted groove mixer[25]) can be further studied at the millifluidic scale to determine the effect of design on mixing effectiveness.

Additionally, sometimes capping agents are added to nanoparticles to control NP size and shape[26, 27], promote catalytic performance of NPs[28], or bind specific biological analytes[29]. The addition of different capping agents to the NP synthesis process could be tested on the millifluidic SHM by mixing the capping agent directly with the reagents or adding another port(s) downstream to attach capping agents to already synthesized NPs.

5.3 References

(1) Wagner, H. N. (2007) PET is alive and well. *J. Nucl. Med. 48*, 495.

(2) Uz Zaman, M., Fatima, N., Sajjad, Z., Zaman, U., Tahseen, R., and Zaman, A. (2014) 18FDG Synthesis and Supply: a Journey from Existing Centralized to Future Decentralized Models. *Asian Pac. J. Cancer Prev. 15*, 10057-10059.

(3) Zeglis, B. M., Houghton, J. L., Evans, M. J., Viola-Villegas, N., and Lewis, J. S. (2014) Underscoring the Influence of Inorganic Chemistry on Nuclear Imaging with Radiometals. *Inorg. Chem. 53*, 1880-1899.
(4) Taggart, M. P., Tarn, M. D., Esfahani, M. M., Schofield, D. M., Brown, N. J., Archibald, S. J., Deakin, T., Pamme, N., and Thompson, L. F. (2016) Development of radiodetection systems towards miniaturised quality control of PET and SPECT radiopharmaceuticals. *Lab Chip 16*, 1605-1616.
(5) Rensch, C., Lindner, S., Salvamoser, R., Leidner, S., Bold, C., Samper, V., Taylor, D., Baller, M., Riese, S., Wangler, C., and Wangler, B. (2014) Solvent resistant lab-on-chip platform for radiochemistry applications. *Lab Chip 14*, 2556-2564.
(6) Chen, S., Javed, M. R., Kim, H. K., Lei, J., Lazari, M., Shah, G. J., van Dam, R. M., Keng, P. Y., and Kim, C. J. (2014) Radiolabelling diverse positron emission tomography (PET) tracers using a single digital microfluidic reactor chip. *Lab Chip 14*, 902-910.
(7) Eckelman, W. C., Reba, R. C., and Kelloff, G. J. (2008) Targeted imaging: an important biomarker for understanding disease progression in the era of personalized medicine. *Drug Discov. Today 13*, 748-759.
(8) Sun, L. Y., Gai, Y. K., Anderson, C. J., and Zeng, D. X. (2015) Highly-efficient and versatile fluorous-tagged Cu(I)-catalyzed azide-alkyne cycloaddition ligand for preparing bioconjugates. *Chem. Commun. 51*, 17072-17075.
(9) Knör, S., Modlinger, A., Poethko, T., Schottelius, M., Wester, H.-J., and Kessler, H. (2007) Synthesis of Novel 1,4,7,10-Tetraazacyclodecane-1,4,7,10-Tetraacetic Acid (DOTA) Derivatives for Chemoselective Attachment to Unprotected Polyfunctionalized Compounds. *Chem. – Eur. J. 13*, 6082-6090.
(10) Li, H., Zhou, H., Krieger, S., Parry, J. J., Whittenberg, J. J., Desai, A. V., Rogers, B. E., Kenis, P. J. A., and Reichert, D. E. (2014) Triazine-Based Tool Box for Developing Peptidic PET Imaging Probes: Syntheses, Microfluidic Radiolabeling, and Structure–Activity Evaluation. *Bioconjug. Chem. 25*, 761-772.
(11) Liu, Y. L., Gunda, V., Zhu, X., Xu, X. D., Wu, J., Askhatova, D., Farokhzad, O. C., Parangi, S., and Shi, J. J. (2016) Theranostic near-infrared fluorescent nanoplatform for imaging and systemic siRNA delivery to metastatic anaplastic thyroid cancer. *Proc. Natl. Acad. Sci. U.S.A. 113*, 7750-7755.
(12) Zhao, Y., Sultan, D., Detering, L., Cho, S., Sun, G., Pierce, R., Wooley, K. L., and Liu, Y. (2014) Copper-64-Alloyed Gold Nanoparticles for Cancer Imaging: Improved Radiolabel Stability and Diagnostic Accuracy. *Angew. Chem., Int. Ed. 53*, 156-159.
(13) Coughlin, A. J., Ananta, J. S., Deng, N., Larina, I. V., Decuzzi, P., and West, J. L. (2014) Gadolinium-Conjugated Gold Nanoshells for Multimodal Diagnostic Imaging and Photothermal Cancer Therapy. *Small 10*, 556-565.
(14) Gao, X. H., Cui, Y. Y., Levenson, R. M., Chung, L. W. K., and Nie, S. M. (2004) In vivo cancer targeting and imaging with semiconductor quantum dots. *Nat. Biotechnol. 22*, 969-976.
(15) Yoo, H., Moon, S. K., Hwang, T., Kim, Y. S., Kim, J. H., Choi, S. W., and Kim, J. H. (2013) Multifunctional Magnetic Nanoparticles Modified with Polyethylenimine and Folic Acid for Biomedical Theranostics. *Langmuir 29*, 5962-5967.
(16) Lohse, S. E., Eller, J. R., Sivapalan, S. T., Plews, M. R., and Murphy, C. J. (2013) A Simple Millifluidic Benchtop Reactor System for the High-Throughput Synthesis and

Functionalization of Gold Nanoparticles with Different Sizes and Shapes. *ACS Nano 7*, 4135-4150.
(17) Shahbazali, E., Hessel, Volker, Noël, Timothy, Wang, Qi. (2016) Metallic nanoparticles made in flow and their catalytic applications in micro-flow reactors for organic synthesis. *Physical Sciences Reviews 1*.
(18) Cheung, T. L., Hong, L. Y., Rao, N. X., Yang, C. B., Wang, L. B., Lai, W. J., Chong, P. H. J., Law, W. C., and Yong, K. T. (2016) The non-aqueous synthesis of shape controllable Cu2-xS plasmonic nanostructures in a continuous-flow millifluidic chip for the generation of photo-induced heating. *Nanoscale 8*, 6609-6622.
(19) Rahman, M., and Rebrov, E. (2014) Microreactors for Gold Nanoparticles Synthesis: From Faraday to Flow. *Processes 2*, 466.
(20) Evans, V., Mahon, M. F., and Webster, R. L. (2014) A mild, copper-catalysed amide deprotection strategy: use of tert-butyl as a protecting group. *Tetrahedron 70*, 7593-7597.
(21) Xu, Z., Lu, C., Riordon, J., Sinton, D., and Moffitt, M. G. (2016) Microfluidic Manufacturing of Polymeric Nanoparticles: Comparing Flow Control of Multiscale Structure in Single-Phase Staggered Herringbone and Two-Phase Reactors. *Langmuir 32*, 12781-12789.
(22) Lim, J.-M., Swami, A., Gilson, L. M., Chopra, S., Choi, S., Wu, J., Langer, R., Karnik, R., and Farokhzad, O. C. (2014) Ultra-High Throughput Synthesis of Nanoparticles with Homogeneous Size Distribution Using a Coaxial Turbulent Jet Mixer. *ACS Nano 8*, 6056-6065.
(23) Woldemariam, M., Filimonov, R., Purtonen, T., Sorvari, J., Koiranen, T., and Eskelinen, H. (2016) Mixing performance evaluation of additive manufactured milli-scale reactors. *Chem. Eng. Sci. 152*, 26-34.
(24) Cortes-Quiroz, C. A., Azarbadegan, A., Zangeneh, M., and Goto, A. (2010) Analysis and multi-criteria design optimization of geometric characteristics of grooved micromixer. *Chem. Eng. J. 160*, 852-864.
(25) Kang, T. G., and Kwon, T. H. (2004) Colored particle tracking method for mixing anlysis of chaotic micromixers. *J. Micromech. Microeng. 14*, 891-899.
(26) Ajitha, B., Reddy, Y. A. K., Reddy, P. S., Jeon, H. J., and Ahn, C. W. (2016) Role of capping agents in controlling silver nanoparticles size, antibacterial activity and potential application as optical hydrogen peroxide sensor. *RSC Adv. 6*, 36171-36179.
(27) You, H. J., Yang, S. C., Ding, B. J., and Yang, H. (2013) Synthesis of colloidal metal and metal alloy nanoparticles for electrochemical energy applications. *Chem. Soc. Rev. 42*, 2880-2904.
(28) Niu, Z., and Li, Y. (2014) Removal and Utilization of Capping Agents in Nanocatalysis. *Chem. Mater. 26*, 72-83.
(29) Baptista, P., Pereira, E., Eaton, P., Doria, G., Miranda, A., Gomes, I., Quaresma, P., and Franco, R. (2008) Gold nanoparticles for the development of clinical diagnosis methods. *Anal. Bioanal. Chem. 391*, 943-950.